1987

Nonradiative excitation decay of dyes on insulators and semiconductors

Robert L. Crackel
Iowa State University

INFORMATION TO USERS

While the most advanced technology has been used to photograph and reproduce this manuscript, the quality of the reproduction is heavily dependent upon the quality of the material submitted. For example:

- Manuscript pages may have indistinct print. In such cases, the best available copy has been filmed.

- Manuscripts may not always be complete. In such cases, a note will indicate that it is not possible to obtain missing pages.

- Copyrighted material may have been removed from the manuscript. In such cases, a note will indicate the deletion.

Oversize materials (e.g., maps, drawings, and charts) are photographed by sectioning the original, beginning at the upper left-hand corner and continuing from left to right in equal sections with small overlaps. Each oversize page is also filmed as one exposure and is available, for an additional charge, as a standard 35mm slide or as a 17"x 23" black and white photographic print.

Most photographs reproduce acceptably on positive microfilm or microfiche but lack the clarity on xerographic copies made from the microfilm. For an additional charge, 35mm slides of 6"x 9" black and white photographic prints are available for any photographs or illustrations that cannot be reproduced satisfactorily by xerography.

Crackel, Robert L.

NONRADIATIVE EXCITATION DECAY OF DYES ON INSULATORS AND SEMICONDUCTORS

Iowa State University PH.D. 1987

PLEASE NOTE:

In all cases this material has been filmed in the best possible way from the available copy. Problems encountered with this document have been identified here with a check mark __√__.

1. Glossy photographs or pages _____
2. Colored illustrations, paper or print _____
3. Photographs with dark background _____
4. Illustrations are poor copy _____
5. Pages with black marks, not original copy _____
6. Print shows through as there is text on both sides of page _____
7. Indistinct, broken or small print on several pages __√__
8. Print exceeds margin requirements _____
9. Tightly bound copy with print lost in spine _____
10. Computer printout pages with indistinct print _____
11. Page(s) _____ lacking when material received, and not available from school or author.
12. Page(s) _____ seem to be missing in numbering only as text follows.
13. Two pages numbered _____. Text follows.
14. Curling and wrinkled pages _____
15. Dissertation contains pages with print at a slant, filmed as received _____
16. Other _____

_____

_____

Nonradiative excitation decay of dyes on insulators and semiconductors

by

Robert L. Crackel

A Dissertation Submitted to the
Graduate Faculty in Partial Fulfillment of the
Requirements for the Degree of

DOCTOR OF PHILOSOPHY

Department: Chemistry
Major: Physical Chemistry

Approved:

Members of the Committee:

Signature was redacted for privacy.
In Charge of Major Work

Signature was redacted for privacy.
For the Major Department

Signature was redacted for privacy.

Signature was redacted for privacy.
For the Graduate College

Iowa State University
Ames, Iowa

1987

TABLE OF CONTENTS

CHAPTER I. THEORY OF EXCITATION TRANSPORT AND TRAPPING

Introduction

The technique of dye sensitization, i.e., the use of organic dye molecules to enhance the absorption capabilities of a material in the lower energy areas of the spectrum, has been known for almost a century [1]. Until the 1970s, the technique was mainly investigated as to possible applications in the field of photography [1-5]. The primary interest in this area was to extend the absorption of the blue-sensitive silver-halide emulsion into the visible and near-infrared regions of the electromagnetic spectrum [3]. When solar energy research became more prominent, one area that received considerable attention was the use of photoelectrochemistry for solar energy conversion and storage [6]. One such application is the photovoltaic cell [7], in which a semiconductor electrode, connected to a counter electrode and immersed in an electrolytic solution, produces an electric current and voltage upon illumination from an external source. In order for the voltage and current to be produced, the energy of the incident radiation must be greater than the energy separation between the valence and conduction bands [6], i.e., the bandgap energy. This limits the semiconductors that can be used to narrow bandgap semiconductors which absorb in the visible or infra-red. By using dye sensitization, the effective absorption spectra of

wide bandgap semiconductors and insulators, which usually absorb in the ultra-violet, can be extended further into the red in order to make these materials more effective solar cells (see Figure 1.1).

Gerischer and Willig [8] have written an excellent review of the electrochemical work done involving dye sensitization through the middle 1970s. It is possible to describe dye sensitization in the following manner. Organic dye molecules are affixed to the surface of a substrate either by direct absorption [9-11] or by covalent attachment [12-14]. The dye molecules absorb the incident radiation, which is usually visible light, and end up in an electronically excited state. Once the electron is in the excited state it can be transferred into the conduction band of the substrate, provided that the energy of the excited state is greater than the energy of the conduction band. Once this electron is inserted in the conduction band by means of this "electron injection" mechanism, it is mobile and can be driven through a load to produce a voltage [8]. After the electron is injected into the semiconductor, the dye molecule will be oxidized and unable to absorb the incident radiation again until the electron is replaced via back transfer from the semiconductor or electron transfer from another source [8]. This process is illustrated in Figure 1.2. In this diagram D is the dye molecule in the ground state, D^* is the dye molecule in the excited electronic state, D^+ is the oxidized dye molecule, E_v is the energy of the valence band, E_c is the energy of the conduction band, and E_f is the Fermi energy of the semiconductor.

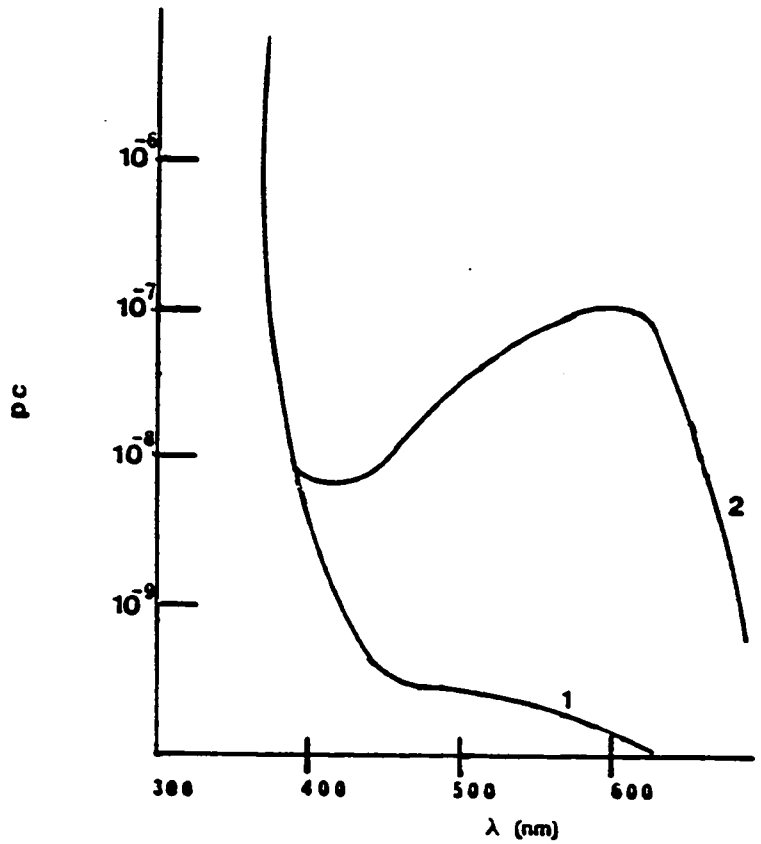

Experimental evidence for dye sensitization.

Figure 1.1. A qualitative plot of the light-generated photocurrent (vertical axis) vs. the wavelength of incident light (horizontal axis) for an unsensitized ZnO electrode (curve1) and for a ZnO electrode sensitized with the dye Rhodamine B (curve 2)

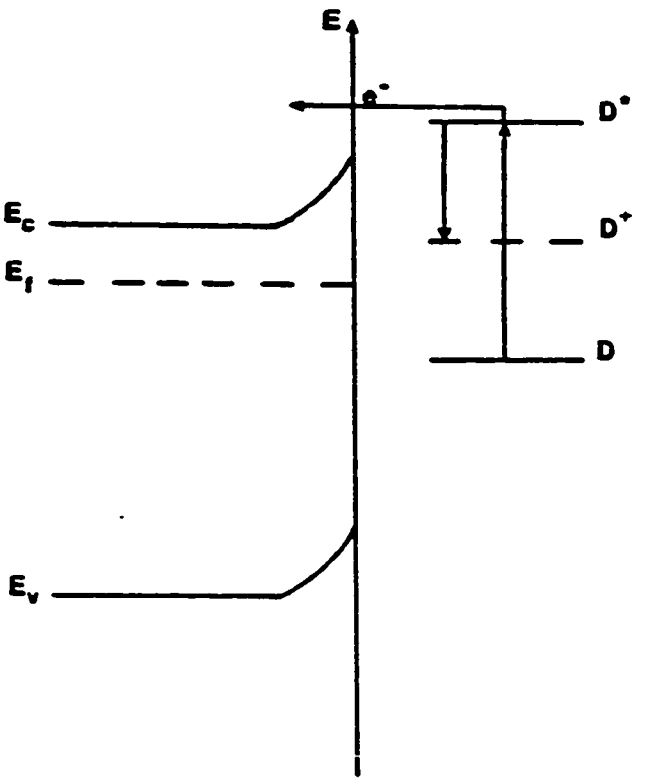

Figure 1.2. Mechanism for dye sensitization of a semiconductor electrode. E_V, E_C, and E_f are the energy levels of the valence band, conduction band, and Fermi energy, respectively of the semiconductor. D, D^*, and D^+ represent the dye molecule in ground, excited, and oxidized states, respectively

One quantity that is of interest in dye-sensitized semiconductors is the quantum efficiency for electron injection, Φ_p, which is determined by measuring the photocurrent produced by the semiconductor compared to the amount of light absorbed by the dye molecules [15]. The equation describing this quantum efficiency is

$$\Phi_p = \frac{k_{EI}}{k_{EI} + k_{fl} + k_q} \frac{k_{inj}}{k_{inj} + k_{rev}} \tag{1.1}$$

The variables in the above equation are: k_{EI}, the rate constant for electron injection, k_{fl}, the rate constant of fluorescence, k_q, the rate constant for all fluorescence quenching processes, k_{inj}, the rate at which electrons are removed to the bulk from the surface, and k_{rev}, the rate of back transfer from the substrate to the dye molecule [15]. The second factor in the equation becomes unimportant when $k_{inj} >> k_{rev}$, in other words when there is very little back transfer from substrate to the oxidized dye molecules. The equation can then be rewritten as

$$\Phi_p = \frac{k_{EI}}{k_{EI} + \tau} \tag{1.2}$$

where

$$\tau = \frac{1}{k_{fl} + k_q} \tag{1.3}$$

is the fluorescence lifetime in the absence of electron injection [15].

A significant amount of research has been done attempting to understand the process of dye sensitization. Initially most of the experiments were centered around trying to measure photocurrents and quantum efficiencies with electrochemical methods [9-11, 16-23], but more recently some investigators have examined the process by using the optical properties of the dye molecules to characterize the systems which are studied through such techniques as total internal reflection spectroscopy [24-28] and time-resolved fluorescence-emission spectroscopy [29-34]. An important conclusion from these experiments is that even though the electron injection quantum efficiency, Φ_p, is very small for single crystal surfaces, on the order of 10^{-2} [10, 28] for dyes adsorbed in monomeric form, the dye molecules still exhibit significant fluorescence quenching and fluorescence lifetime shortening [29-34] relative to what is seen for the same dyes in dilute solutions. This implies that some type of nonradiative energy transfer must be occurring which causes the fluorescence quenching and lifetime shortening. Since most of the dye molecules under consideration are laser dyes, they have very high fluorescence quantum yields meaning that the intramolecular nonradiative decay processes are not important mechanisms [35]. Therefore, the decay process is probably some type of intermolecular nonradiative energy transfer. To better understand what this process might be, it is necessary to examine the theory behind excitation transport and trapping.

Excitation transport and trapping

Nonradiative energy transfer between molecules is a phenomenon which has been of interest for many years. Beginning in the late 1940s, Förster examined this phenomenon in a series of papers [36-41] in which he determined that intermolecular interaction can be described in terms of a multipole expansion with usually only the dipole-dipole portion being of importance in singlet excitation transport at long distances. In his treatment, Förster defines three different cases for describing excitation transfer between molecules [40, 41]. The strength of the molecular interaction is the determining factor as to which case a system belongs. The difference in interactions is evident from the magnitude of change seen in absorption spectra [41].

The first case is called the strong coupling case and is characterized by major changes in the absorption spectra of the molecules being studies. The shapes of the vibronic envelopes in these spectra are completely different than the vibronic envelopes of the individual component molecules [41], even if the absorption occurs in approximately the same region. Systems for which the strong coupling is applicable are those in which the excitation is entirely delocalized such as between the molecules in a dimer or a higher aggregate.

The next case is the weak coupling case in which the interaction energy is not as strong and the changes in the absorption spectra are not as pronounced as in the strong coupling case. The overall shape

of the vibronic envelope is not changed but individual vibronic levels evidence a splitting which is termed the Davydov splitting [41]. For the weak coupling case, the delocalization of the excitation is weaker than in the strong coupling case because of the type of interaction which is in effect.

The last case, the most common one, is called the very weak coupling case in which the absorption spectra of the individual components remain virtually unchanged [41]. In this case, the excitation is localized on a specific molecule and through the interaction is transferred from one molecule to another. An alternative way [40] to view these cases is as follows. In the strong coupling case, the vibronic envelopes of the components are completely in resonance, which results in almost complete delocalization of the excitation. The weak coupling case has individual vibronic levels on the molecules which are in resonance, so that the excitation is thought of as being neither completely delocalized throughout the system or localized on a specific molecule. For the very weak coupling case, only certain regions of individual vibronic levels on the component molecules are in resonance which means that the excitation is essentially localized because the individual vibronic band width is no longer less than the vibronic splitting due to the molecular interaction [40].

Figure 1.3 illustrates the very weak coupling interaction. In the first step, the donor molecule, D, absorbs the incident energy thereby promoting an electron from the ground electronic state to an

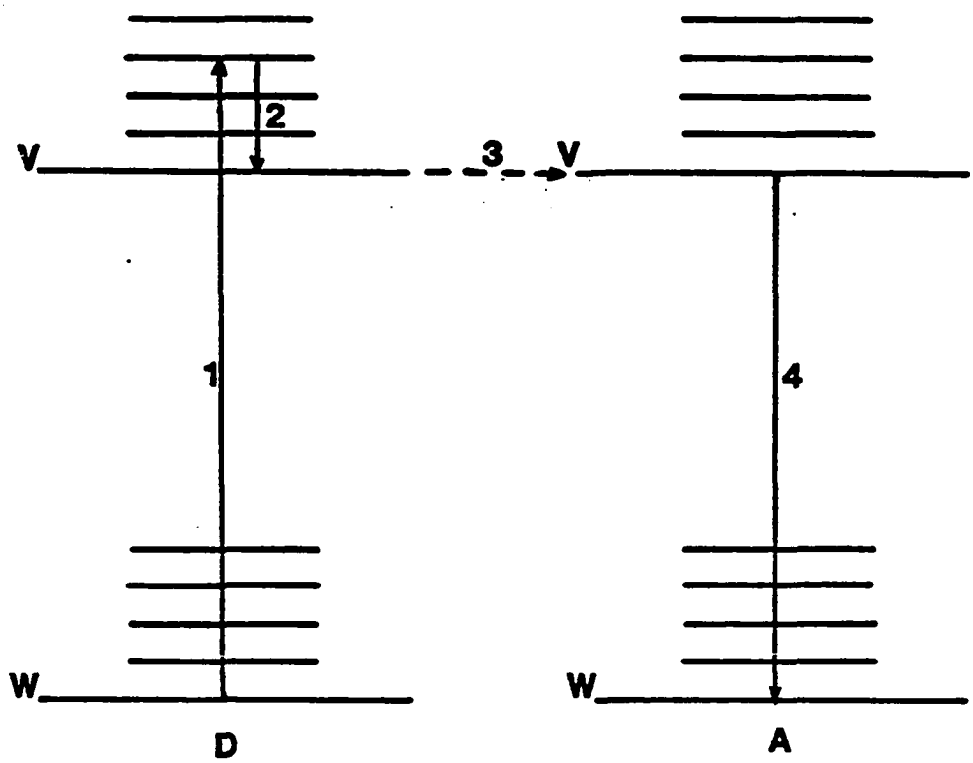

Figure 1.3. Diagram illustrating excitation transfer between a donor(D) and an acceptor(A) for the very weak coupling case. V and W are the vibrational states for the excited and ground electronic states, respectively

excited electronic state. The second step is vibrational relaxation of the excitation to the group vibrational level of the excited electronic state. The transfer of the excitation from the donor to the acceptor, A, is depicted by the third step. The fourth and final step is the relaxation of the excitation to the ground electronic state of the acceptor by either radiative or nonradiative mechanisms. The figure as drawn shows nonradiative energy transfer between like molecules. As will be seen later, this transfer can occur whenever the fluorescence spectrum of the donor and the absorption spectrum of the acceptor overlap. In fact, the greater the overlap of the spectra the more probable it is that the excitation can be transferred.

If the excited donor molecule is in vibrational level v and the unexcited acceptor is in vibrational level w then the vibronic interaction energy will be $U_{vw} = US^2_{vw}$ (1.4) where the quantities U, the electronic interaction energy, and S_{vw}, the vibrational overlap integral, are defined as

$$U_{DA} = \langle \phi_D^* \phi_A | V_{DA} | \phi_D \phi_A^* \rangle \tag{1.5}$$

and

$$S_{VW} = \langle x_v^* | x_w \rangle \tag{1.6}$$

The ϕ's and ϕ'^*s are ground state and excited state wavefunctions for the molecules, V_{DA} is the intermolecular interaction potential between the donor and acceptor, and χ and χ^* are the vibronic functions for

the molecules in the ground and excited states, respectively [41]. The expression for the interaction energy comes from Fermi's Golden Rule [42] which is used to evaluate nonradiative decay rates and gives the interaction energy as the product of the vibrational overlap and the electronic interaction between the involved states.

The electronic interaction energy, U, can be expanded in terms of a multipole expansion [36]. The first term is a dipole-dipole term that arises from the transition dipole moments, $\underline{m}_D$ and $\underline{m}_A$, of the donor and acceptor molecules. These transition dipole moments are proportional to the oscillator strengths of the transitions between the ground and excited states. The interaction energy can then be written as

$$U \sim \frac{1}{n^2 R_{DA}^{\ 3}} \left[(\underline{m}_D \underline{m}_A) - \frac{3}{R^2} (\underline{m}_D \underline{R}_{DA})(\underline{m}_A \underline{R}_{DA}) \right] \tag{1.7}$$

where n is the refractive index of the material surrounding the dipoles, and R_{DA} is distance between the donor and acceptor [41].

It can be shown (41) that the probability that the excitation is on the acceptor will be given by

$$\rho^*_{DA}(t) = 4 \iint \frac{u^2 (E_D E_A^*) \sin^2 (\Delta E t / 2h) dE_D dE_A^*}{(\Delta E)^2} \tag{1.8}$$

where (E_D^*, E_A) and (E_D, E_A^*) are the initial and final state total vibronic energies, respectively, and ΔE is the energy difference between the initial and final states

$$\Delta E = E_D^* - E_D - E_A^* + E_A \tag{1.9}$$

For the very weak coupling case the integral is evaluated in the limit of large τ to give

$$\rho_{DA}^*(t) = 4 \lim_{t\to\infty} \iint \frac{u^2(E_D, E_A^*) \sin^2[(\Delta E_t)/2\hbar] dE_D\, dE_A^*}{(\Delta E)^2}$$

$$= \frac{\pi t}{h^2} \iint u^2(E_D, E_A^*) \lim_{t\to\infty} \frac{\sin^2[(\Delta E t)/2h]}{\pi(\Delta E/2h)^2 t}\, dE_D\, dE_A^* \tag{1.10}$$

Using the relationship

$$\delta(x) = \lim_{t\to\infty} \frac{\sin^2 tx}{\pi t x^2} \tag{1.11}$$

gives

$$e_{DA}^*(t) = \frac{\pi t}{h^2} \iint u^2(E_D, E_A^*)\, \delta\left(\frac{\Delta E}{2h}\right) dE_D\, dE_A^*$$

$$= \frac{2\pi t}{h} \iint u^2(E_D, E_A^*)\, \delta(\Delta E)\, dE_D\, dE_A^* \tag{1.12}$$

Transformation of variables to

$$E = \frac{1}{2}[E_D^* - E_D + E_A^* - E_A] \tag{1.13}$$

results in the equation

$$\rho_{DA}^{*}(t) = \frac{2\pi t}{\hbar} \int u^2 (E, 0)\, dE \tag{1.14}$$

The transfer rate, $k_{D \rightarrow A}^{VW}$, is the probability, $\rho_{DA}^{*}(t)$, divided by time which means that

$$k_{D \rightarrow A}^{VW} = \frac{2\pi}{\hbar} \int u^2(E,0)\, dE \tag{1.15}$$

To evaluate the integral in equation (1.15) knowledge of the function u(E,0) is required. This function can be rewritten as [41]

$$u(E,0) = u(E_D^{*}, E_A; E_D, E_A^{*})$$

$$= u(E_D^{*}, E_A; E_D^{*} - E, E_A + E) \tag{1.16}$$

Use of the Born-Oppenheimer vibronic functions,

$$\Psi_{D^*A}(E_D^{*}, E_A) = \phi_D^{*}\, \phi_A\, \chi_D^{*}(E_D^{*})\chi_A^{*}(E_A)$$

$$\bar{\Psi}_{DA^*}(E_D, E_A^{*}) = \phi_D\, \phi_A^{*}\, \chi_D(E_D^{*} - E)\chi_A^{*}(E_A + E) \tag{1.17}$$

allows the quantity of interest to be expressed as

$$u^2(E, 0) = \langle \phi_D^* \phi_A | V | \phi_D \phi_A^* \rangle^2 S_D^2 (E_D^*, E_D^* - E) S_A^2 (E_A, E_A + E)$$

$$= U^2 S_D^2 (E_D^*, E_D^* - E) S_A^2 (E_A, E_A + E) \qquad (1.18)$$

where $S(E_1, E_2) = \langle \chi^*(E_1) | \chi(E_2) \rangle$ [41]. For dipole-dipole interaction, from equation (1.7)

$$U^2 = \frac{\kappa^2 |\underline{m}_D^2| \, |\underline{m}_A^2|}{n^4 R_{DA}^6} \qquad (1.19)$$

where κ is an orientational factor containing the directional dependence of the interaction energy and is given by [39]

$$\kappa = \cos \theta_{DA} - 3\cos \theta_D \cdot \cos\theta_A \qquad (1.20)$$

with θ_{DA} the angle between $\underline{m}_D$ and $\underline{m}_A$, θ_D the angle between $\underline{m}_D$ and the vector between D and A, and θ_A the angle between $\underline{m}_A$ and the vector between D and A. Using equations (1.18) and (1.19) in equation (1.15) gives

$$k_{D \to A} (E_A^*, E_D) = \frac{\kappa^2}{n^4 R_{DA}^6} \int \underline{m}_D^2 S_D^2 (E_D^*, E_D^* - h\nu) \, \underline{m}_A^2 S_A^2 (E_A, E_A + h\nu) d\nu \qquad (1.21)$$

where $E = h\nu$. Equation (1.21) is the transfer rate for those molecules with the initial energies E_D^* and E_A. The total transfer

rate is obtained by taking into account thermal equilibrium, through the use of the Boltzmann factors $g^*(E)$ and $g(E)$, and then integrating over the energies E_D^* and E_A to obtain [41]

$$k_{D\to A} = \frac{\kappa^2}{n^4 \tau^2 R_{ab}^6} \int [\underline{m}_D \int g^*(E_D^*)\, S_D^2\, (E_D^{\ddagger}, E_D^* - h\nu)\, dE_D^*]$$

$$\cdot\, [\underline{m}_A^2 \int g(E_A)\, S_A^2\, (E_A, E_A + h\nu)\, dE_A]\, d\nu \qquad (1.22)$$

The first term in the integral is related to the spectral density of the donor molecule in an excited state at thermal equilibrium, i.e., the fluorescence spectrum while the second term is similarly related to the acceptor molecule's absorption spectrum. This means that the transfer rate is proportional to the overlap of the donor fluorescence spectrum and the acceptor absorption spectrum.

The transfer rate can be written as

$$k_{D\to A} = \frac{9\kappa^2 (\ln 10) C^4}{128\, \pi^5\, n^4\, N \tau_D\, R_{DA}^6} \int f_D(\nu)\, \varepsilon_A(\nu)\, \frac{d\nu}{\nu^4} \qquad (1.23)$$

where $\varepsilon_A(\nu)$, the molar decadic extinction coefficient, and $f_D(\nu)$, the fluorescence quantum spectrum are given by

$$\varepsilon_A(\nu) = \frac{4\pi^2 N \underline{m}_A^2 \nu}{3(\ln 10) n \hbar c} \int g_A(E)\, S^2(E_A, E_A + h\nu)\, dE_A \qquad (1.24)$$

and

$$f_D(\nu) = \frac{2^5\pi^3 n\tau_D m_D^2 \nu^3}{3hc^3} \int g^*_D(E_D^*)\, S^2(E_D^*,\, E_D^* - h\nu)\, dE_D^* \qquad (1.25)$$

N is the concentration in molecules per millimole, τ_D is the natural fluorescence lifetime of the donor, c is the speed of light, and for a randomly oriented collection of molecules $\kappa^2 = 2/3$ [39].

Equation (1.23) is more commonly written in the form

$$k_{D\to A} = \frac{1}{\tau_D}\left(\frac{R_o}{R}\right)^6 \qquad (1.26)$$

where R_o is the distance at which the excitation transfer rate and the radiative rate of the donor have equal probability and is given by [39]

$$R_o^6 = \frac{9\,\kappa^2(\ln 10)c^4}{128\pi^5 n^4 N} \int f_D(\nu)\, \varepsilon_A(\nu)\, \frac{d\nu}{\nu^4} \qquad (1.27)$$

Knox (43) defines $\bar{R}_o$ as being the acceptor distance at which excitation transfer and the total donor deexcitation have equal rates. This results in the expression

$$k_{D\to A} = \frac{1}{\tau_D}\left(\frac{R_o}{R}\right)^6 = \frac{1}{\tau}\left(\frac{\bar{R}_o}{R}\right)^6 \qquad (1.28)$$

where $\bar{R}_o = \phi_F^{1/6} R_o$, $\tau = \phi_F \tau_o$ is the measured donor lifetime, and ϕ_F is the fluorescence quantum yield of the donor when no acceptor is present. Figure 1.4 illustrates the relationships among R_o, $\bar{R}_o$, and κ

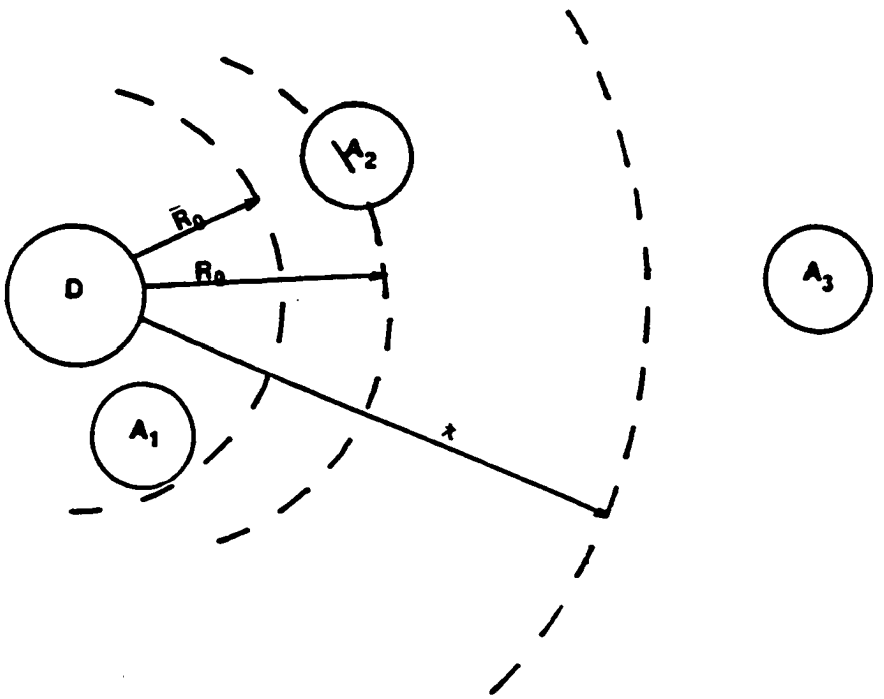

Figure 1.4. Diagram showing the distance relationships between the initially excited donor molecule, D, and the acceptor molecules A_1, A_2, and A_3. A_1 and A_2 accept energy through the Förster-type dipole-dipole interaction. A_3, the far-field acceptor, has to absorb the radiation from D in order for energy transfer to occur

where $\chi = \lambda/2\pi_n$ is the distance past which the acceptor behaves as only an absorber of electromagnetic radiation [43]. In the figure, the rate of excitation transfer to A_1 is greater than the total rate of radiation decay, the rate of transfer to A_2 is equal to the radiative rate, and transfer to A_3 is solely by absorption of radiation.

Once the form of the rate constant for excitation transfer is known, it is possible to find the probability p(t) that the excitation resides on the donor after a certain amount of time, t. Förster [37] derived the expression for this quantity in three dimensions. The master equation describing this probability for a system of N molecules is

$$\frac{-d\rho}{dt} = \frac{1}{\tau_o} + \frac{1}{\tau_o} \sum_{k=1}^{N} \left(\frac{R_o}{R_k}\right)^6 \tag{1.29}$$

where τ_o is the natural lifetime of the initially excited molecule and the second term is a sum of transfer rate constants having the form

$$k_{D \rightarrow A} = \frac{1}{\tau_o} \left(\frac{R_o}{R}\right)^6 \tag{1.26}$$

Integration of this equation along with the initial condition $\rho(0) = 1$ gives the result [37]

$$\rho(t) = \exp\left\{-\left[1 + \sum_{k=1}^{N} \left(\frac{R_o}{R_k}\right)^6\right] \frac{t}{\tau_o}\right\}$$

$$= \exp\left(\frac{-t}{\tau_o}\right) \prod_{k=1}^{N} \exp\left[\left(\frac{-R_o}{R_k}\right)^6 \frac{t}{\tau_o}\right] \tag{1.30}$$

If w(R) dR is the probability that an acceptor is located at a distance between R and R + dR away from the initially excited donor molecule then the average excitation probability will be [37]

$$\tilde{\rho}(t) = \exp\left(\frac{-t}{\tau_o}\right) \prod_{k=1}^{N} \int_o^{R_g} \exp\left[-\left(\frac{R_o}{R}\right)^6 \frac{t}{\tau_o}\right] w(R_k) d R_k$$

$$= \exp\left(\frac{-t}{\tau_o}\right) [J(t)]^N \tag{1.31}$$

where $J(t) = \int_o^{Rg} \exp\left[-\left(\frac{R_o}{R}\right)^6 \frac{t}{\tau}\right] w(R)\, dR$ (1.32)

In three dimensions, the volume, V, of a sphere with a center located at the initially excited donor, D, and a radius of R_g is

$$V = \frac{4\pi}{3} R_g^3 \tag{1.33}$$

This means that the distribution function w(R) must satisfy the relationship

$$w(R)\, dR = \frac{4\pi R^2\, dR}{V} \tag{1.34}$$

Substitution of equation (1.34) into the expression for J(t) gives [37]

$$J(t) = \frac{4\pi}{V} \int_o^{R_g} \exp[-(\frac{R_o}{R})^6 \frac{t}{\tau}] \, R^2 \, dR \tag{1.35}$$

By defining the new variables ζ and ζ_g such that $\zeta \equiv (\frac{R_o}{R})^6 \frac{t}{\tau}$ and $\zeta_g \equiv (\frac{R_o}{R_g})^6 \frac{t}{\tau_o}$ it is possible to rewrite J(t) in the form [37]

$$J(t) = \frac{1}{2} (\zeta_g)^{1/2} \int_{\zeta_g}^{\infty} \exp(-\zeta) \, \zeta^{-3/2} \, d\zeta \tag{1.36}$$

Since R_o is much smaller than the macrosopic radius of the sphere, R_g, the result is that for all times t the quantity ζ_g is much smaller than one. This allows the integral to be expressed as a series in increasing powers of $\zeta_g^{1/2}$. The integral is evaluated using integration by parts to give the expression [37]

$$\int_{\zeta_g}^{\infty} \exp(-\zeta_g) \, \zeta^{-3/2} \, d\zeta = -[2\exp(-\zeta)\zeta^{-1/2}]_{\zeta_g}^{\infty} - 2\int_{\zeta_g}^{\infty} \exp(-\zeta)\zeta^{-1/2} \, d\zeta$$

$$= 2\exp(-\zeta_g)\zeta_g^{-1/2} - 2\int_o^{\infty} \exp(-\zeta) \, \zeta^{-1/2} \, d\zeta + 2 \int_o^{\zeta_g} \exp(-\zeta)\zeta^{-1/2} \, d\zeta$$

$$= 2\zeta_g^{-1/2} - 2\pi^{1/2} + \ldots \tag{1.37}$$

where $\exp(-\zeta_g)$ goes to one as ζ_g goes to zero and $\int_o^{\infty} \zeta^{-1/2} \exp(-\zeta) \, d\zeta = \Gamma(\frac{1}{2}) = \pi^{1/2}$ [44]. The succeeding terms will involve $\zeta_g^{1/2}$, $\zeta_g^{3/2}$, . . ., and will disappear as ζ_g goes to zero.

Substitution of equation 1.37 into equation (1.36) gives for J(t) [37]

$$J(t) = \frac{1}{2}\,\zeta_g^{1/2} \int_{\zeta_g}^{\infty} \exp(-\zeta)\zeta^{-3/2}\, d\zeta$$

$$= \frac{1}{2}\,\zeta_g^{1/2}[2\zeta_g^{-1/2} - 2\pi^{1/2}] = 1 - (\pi\zeta_g)^{-1/2} \qquad (1.38)$$

The result for the average probability, $\bar{\rho}(t)$, is [37]

$$\bar{\rho}(t) = \exp(\frac{-t}{\tau_o})\ [J(t)]^N$$

$$= \exp(\frac{-t}{\tau_o})\ [1 - (\pi\zeta_g)^{1/2}]^N \qquad (1.39)$$

where N is the number of molecules located in the volume V and is very large for the cases where R_o is much smaller than the radius of the sphere, R_g. Therefore, the limit as N goes to infinity is taken and the result obtained is [37]

$$\bar{\rho}(t) = \exp(\frac{-t}{\tau_o}) \lim_{N\to\infty} [1 \frac{-1}{N} (\pi\zeta g)^{1/2}]^N$$

$$= \exp(\frac{-t}{\tau_o})\ \exp[-N\ (\pi\zeta g)^{1/2}]$$

$$= \exp(\frac{-t}{\tau_o})\ \exp[\frac{-NR_o^3}{Rg^3}\ \pi^{1/2}\ (\frac{t}{\tau_o})^{-1/2}] \qquad (1.40)$$

after substituting the defined value of τ_g back into the equation. If a reduced concentration, C, is defined as

$$C = N \frac{R_o^3}{R_g^3} \tag{1.41}$$

then the average probability that the excitation resides on the initially excited donor is

$$\bar{\rho}(t) = \exp(\frac{-t}{\tau_o}) \exp[-C\pi^{1/2}(\frac{t}{\tau_o})^{1/2}] \tag{1.42}$$

Equation (1.42) illustrates that the fluorescence lifetime does not obey a single exponential decay law. The physical interpretation for this Förster decay is that the donor molecules located near an acceptor quickly undergo excitation transfer while those located farther away from acceptor molecules give up the excitation more slowly. The net result is that as the concentration increases the greater the probability of excitation transfer by the donor, which means that more of the fluorescence is quenched and the fluorescence lifetime is shortened in a nonexponential fashion.

If the donor and acceptor molecules are attached to a surface, as would be the case for dye-sensitized semiconductors and insulators, the interactions between the dye molecules should occur, depending on the surface flatness, in a dimensionality somewhere between two and three. The equation for the average probability that excitation is still on the donor molecules that obey the dipole-dipole Förster-type

interaction in two dimensions is obtained in the same manner as the three-dimensional equation. In two dimensions the distribution function w(R) dR has the form

$$w(R)\ dR = \frac{2\pi}{A}\ R\ dR \tag{1.43}$$

which means that the integral J(t) becomes

$$J(t) = \frac{2\pi}{A} \int_0^{R_g} \exp[-(\frac{R_o}{R})^6 \frac{t}{\tau_o}]\ R\ dR \tag{1.44}$$

Substituting is ζ and ζ_g as in the three-dimensional case gives

$$J(t) \alpha \int_{\zeta_g}^{\infty} \exp(-\zeta)\ \zeta^{-4/3}\ d\zeta \tag{1.45}$$

This time evaluation of the integral results in a power series involving $\zeta^{-1/3}$ instead of $\zeta^{-1/2}$. The final result as given by Nakashima, Yoshihara, and Willig [30] is

$$\bar{\rho}(t) = \exp(\frac{-t}{\tau_o})\ \exp[-\Gamma\ (\frac{2}{3})\ C\ (\frac{t}{\tau_o})^{1/3}]$$

$$= \exp(\frac{-t}{\tau_o})\ \exp[-1.354\ C\ (\frac{t}{\tau_o})^{1/3}] \tag{1.46}$$

where $\Gamma(\frac{2}{3}) = 1.354$ [30].

The differences between the two- and three-dimensional cases are that the $(\frac{t}{\tau_o})$ term in the second term has a one-third power

dependence instead of a one-half power dependence, the coefficient has changed from $\Gamma(\frac{1}{2}) = \pi^{1/2}$ to $\Gamma(\frac{2}{3}) = 1.354$, and the orientational factor in the Förster rate expression has changed from κ^2 to $\kappa^{2/3}$ [30] where $\kappa^{2/3}$ has been determined by numerical integration to be 0.847.

There are certain limitations in Förster's theory of excitation transfer some of which have been examined by other researchers. One limitation is that Förster restricted his theory to dipole-dipole type interactions. Dexter [45] extended the theory to consider dipole-quadrupole interactions and exchange effects. According to Dexter, the dipole-dipole interactions apply to allowed transitions only. To account for forbidden transitions, the interaction between the dipole of the donor and the quadrupole of the acceptor must be examined. This applies to the case where the donor transition is allowed while the acceptor transition is forbidden, and the rate of transfer is proportional to R^{-8} instead of R^{-6} as was found for the dipole-dipole interaction. The dipole-quadrupole terms become important only at close distances where the wavefunctions of the molecules begin to overlap.

Another limitation to the Förster theory is that he assumed that the acceptor molecule and donor molecule are the nearest neighbors of each other [36]. Ore [46] pointed out that while A might be the nearest neighbor of D there could be another molecule closer to A than D is. If this is the case, once the excitation has been transferred from D to A the probability that it will return to D is small. Knox

[43, 47] and Craver and Knox [48] also looked at the possibility of excitation transfer to molecules other than the initially excited donor and its nearest neighbor. They were interested in measuring the depolarization of the fluorescence as a means of studying energy transfer. The assumption is made that excitation transfer in a disordered system is an incoherent process, so that fluorescence from randomly oriented molecules other than the initially excited donor will be depolarized. This means that the degree of polarization determines the probability that the fluorescence came from the initially excited molecule. Craver and Knox [48] allowed the donor to transfer the excitation to both the nearest and next-nearest neighbors.

Förster also assumes completely random orientation of the dipoles. Blumen [49] derived exact expressions describing ensemble averaged excitation decays for excitation transfer by means of dipole-dipole interactions from a donor to acceptors randomly located on a lattice. He looked at the situations where the dipoles have random angular orientations, as in the Förster case, and where the dipoles have preferential orientation. The expressions derived by Blumen are very similar to those of Förster [41]. In both cases the transfer rate depends upon τ^{-1} and R^{-6}. Also the orientational factor for randomly oriented acceptors is equal to 2/3 the same as what Förster determined. However, Blumen shows that for the acceptors oriented parallel to the donor this factor is 4/5 while for acceptors parallel to the donor it is 3/5. This shows that even for fixed

acceptor orientations the factor κ^2 will only have values ranging from 0.60 to 0.80 and will not make a large difference in either the transfer rate or the time-dependent probability.

Perhaps the most important limitation of the Förster theory is that it assumes energy will be transferred from an excited donor to an acceptor molecule, i.e., it neglects the possibility that the excitation can be transferred from one donor molecule to another. Because of this assumption the Förster theory is accurate only in the region of low donor or high acceptor concentration. If this is not true then the Förster model does not hold at short times when donor to donor transfer is likely to occur. Haan and Zwanzig [50] made use of a master equation to derive a diffusion equation describing the excitation transfer in a one-component system between sites randomly distributed on a lattice. Their derivation involved a Green Function solution to the master equation and then a density expansion of the Green Function. The expansion was truncated after the first two terms to give a result that is accurate at short times and low concentrations but not at longer times and higher concentration where transfer to molecules outside the initial donor ensemble becomes important.

Gochanour, Andersen, and Fayer [51] and Loring, Andersen, and Fayer [52] also took the approach of finding the Green Function solution to the master equation. However, they used a diagrammatic procedure to obtain an equation that approximates the higher order terms in the density expansion of the Green Function. The master

equation used by Haan and Zwanzig [50] and Gochanour et al. [51] and Loring et al. [52] has the form

$$\frac{d\rho_i^*(r, t)}{dt} = \frac{-\rho_i^*(r, t)}{\tau} \sum_i k_{ij}[\rho_j^*(r, t) - \rho_i^*(r, t)] \qquad (1.47)$$

where $\rho_i^*(r, t)$ is the probability that the excitation is on molecule i in the rth configuration at time t, τ is the excitation lifetime, and k_{ij} is the rate of excitation transfer. Using the substitution

$$\rho_i(r, t) = \rho_i^*(r, t) \exp(\frac{t}{\tau}) \qquad (1.48)$$

to eliminate the decay term, Haan and Zwanzig [50] obtained as a solution to the master equation

$$\underline{\rho}(r, t) = \exp(t\,\underline{W}) \cdot \underline{\rho}(r, o) \qquad (1.49)$$

where $\underline{\rho}(r, t)$ is a vector having the components $(\rho_1(r, t), \rho_2(r, t), \ldots, \rho_N(r, t))$, $\underline{\underline{W}}$ is a matrix given by

$$W_{ij} = k_{ij} - S_{ij} \sum_{\ell} k_{j\ell} ,$$

and $\rho_i(r, o)$ depends only on $\underline{r}_i$, the position of the ith molecule. The ensemble average density of excitations is

$$P(\underline{r}, t) = \langle \sum_i \delta(\underline{r}_i - \underline{r})\, \rho_i(r, t) \rangle \qquad (1.50)$$

and can be expressed in terms of a Green Function as

$$P(\underline{r}, t) = \int d\underline{r}' \; G(\underline{r}, \underline{r}', t) \;\; P(\underline{r}', o) \tag{1.51}$$

where $G(\underline{r}, \underline{r}', t) = N^{-1} \langle \sum_i \sum_j \delta(\underline{r}_i - \underline{r}) \; \delta(\underline{r}_j - r') [\exp(t\underline{\underline{W}})]_{ij} \rangle$,

$$P(\underline{r}', o) = \langle \sum_i \delta(\underline{r}_i - \underline{r}') \; F(\underline{r}_i),$$

$$F(\underline{r}_i) = p_j(r, 0)$$

and N is the number density of randomly distributed molecules in the volume being considered. The Green Function is a sum of two types of terms

$$G(\underline{r}, \underline{r}', t) = G^S(\underline{r} - \underline{r}', t) + G^m(\underline{r} - \underline{r}', t) \tag{1.52}$$

where integration of $G^S(\underline{r}, \underline{r}', t)$ gives the probability that the excitation is still on the initially excited donor at time t and integration of $G^m(\underline{r}, \underline{r}', t)$ gives the probability that the excitation is on a donor other than the initially excited donor at time t. Loring, Andersen, and Fayer [52] included the possibility that the excitation is transferred out of the donor ensemble to an acceptor or trap. They add in the term $G^T(\underline{r} - \underline{r}', t)$ that is related to the probability that the excitation to a trap at time t and get

$$G(\underline{r}, \underline{r}', t) = G^{S}(\underline{r}-\underline{r}', t) + G^{m}(\underline{r}-\underline{r}', t) + G^{T}(\underline{r}-\underline{r}', t) \qquad (1.53)$$

The Laplace-Fourier transforms of these probabilities are taken and expansions are obtained in powers of $\underline{\underline{W}}$ to get an ensemble average of infinite series of products of transfer rate factors. Diagrams are constructed for each product. In a one-component system each molecule is represented by a circle and the transfer from one donor to another is shown as a solid arrow between circles. The inverse of the transfer is shown by an dashed arrow and results in lowering the probability that the excitation is on the second donor. A trap site is represented by a square and once the excitation is transferred to a trap it can not be transferred again. These types of diagrams are illustrated in Figure 1.5. The solid dots on the diagram are called vertices and represent the intersection of two arrows as long as the arrow leaving the vertex represents a transfer process. The diagrams are evaluated by means of an ensemble average of the product represented by the diagram. Simplification of the diagrams involves identifying the loops and nodes, where a loop consists of a series of arrows that begin and end on the same site and the sites in the loop do not interact with other sites in the diagram except for the initial site, and a node is a vertex that essentially joins two separate diagrams together. Figure 1.6a is a diagram containing a loop beginning a vertex α and ending a vertex β, while the diagram in Figure 1.6b is an example of a diagram containing a node at vertex

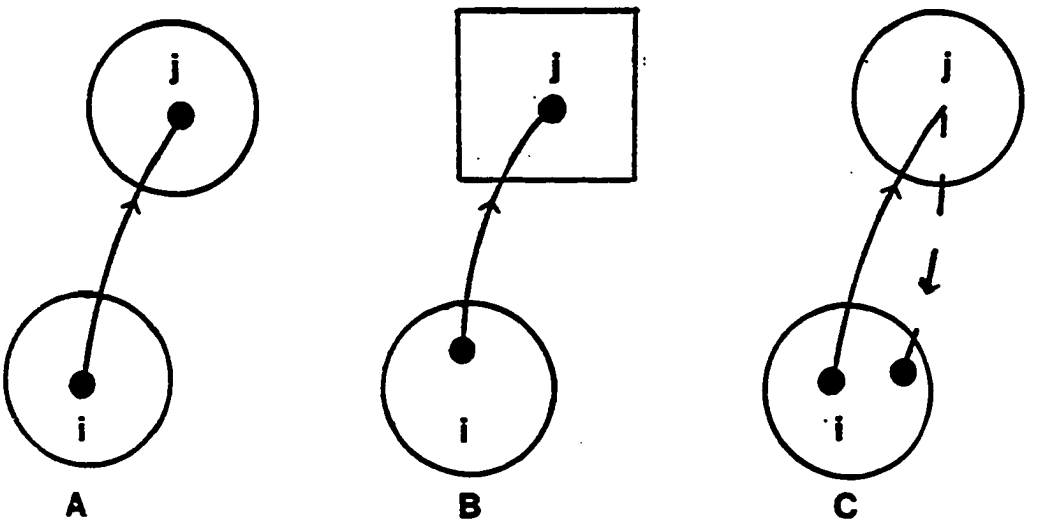

Figure 1.5. Types of Fayer diagrams. A is a Fayer diagram for excitation transfer from molecule i in the donor ensemble to molecule j also in the donor ensemble. B is the diagram for transfer from a donor i to a trap j. C is the same as A except the inverse of the transfer (dashed line) is also included

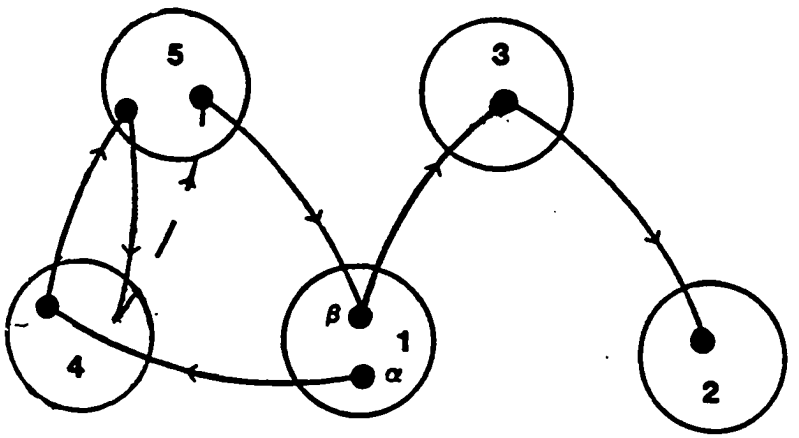

Figure 1.6a. Example of diagram containing a loop. The loop involved begins on vertex α and ends on vertex β. Elimination of the loop results in a three-body diagram

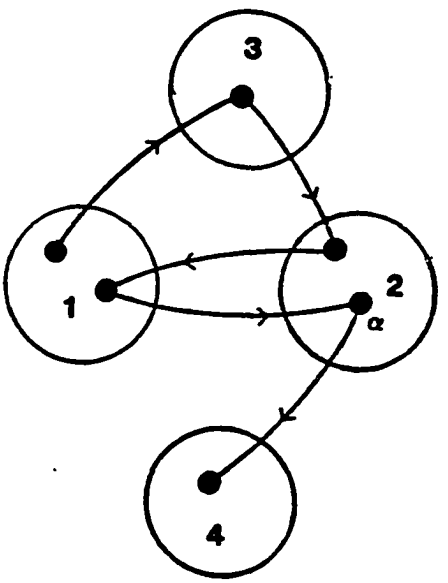

Figure 1.6b. Diagram containing a node at vertex α. Total diagram can be split into a diagram involving sites 1, 2, and 3 and another diagram involving sites 2 and 4

α. By eliminating the loops from the diagrams and expressing those diagrams with nodes as the component diagrams it becomes easier to write expressions for the diagrams. The two-body approximation involving summing those diagrams which after simplification contain only two circles, or sites, while sums of diagrams involving a maximum of three circles is called the three-body approximation. In theory it should be possible to sum the diagrams containing more than three circles but the expressions for the corresponding diagrams of more than three circles become too complex for straightforward evaluation [51]. In both papers [51, 52], the authors pointed out that their diagrammatic approximations are much different from Haan and Zwanzig's [50] truncated density expansion because each of the simplified diagrams also represents an infinite number of diagrams of higher order.

According to Loring, Andersen, and Fayer [52] the two-body approximation to the master equation for excitation transport and trapping has the form

$$\rho(t) = A \exp(\frac{-t}{\tau})\ G^{D}(t) \tag{1.54}$$

where $G^{D}(t)$ is evaluated by taking the numerical inverse Laplace transform [53] of

$$\hat{G}^{D}(t)[0,\ \varepsilon] = \frac{[\hat{G}^{S}(\varepsilon)]^{2}}{\hat{G}^{S}(\varepsilon) - \tilde{\Delta}_{2}[0,\ \hat{G}^{S}(\varepsilon)]} \tag{1.55}$$

where $\hat{G}^S(\varepsilon)$ is evaluated from

$$[\hat{G}^S(\varepsilon)]^{1/3} = [\frac{1}{2\varepsilon} + (\frac{1}{4\varepsilon^2} + \frac{C^3}{27\varepsilon^3})^{1/2}]^{1/3} + [\frac{1}{2\varepsilon} - (\frac{1}{4\varepsilon^2} + \frac{C^3}{27\varepsilon^3})^{1/2}]^{1/3} \tag{1.56}$$

and the other quantities are

$$\tilde{\Delta}_2 [0, \hat{G}^S(\varepsilon)] = \frac{2^{1/3} C_D [\hat{G}^S(\varepsilon)]^{4/3}}{3^{3/2} \tau^{1/3}} \tag{1.57}$$

$$C = \frac{2\pi}{3^{3/2} \tau^{1/3}} (2^{-2/3} C_D + C_T) \tag{1.58}$$

$$C_D = \pi (R_o^{DD})^2 N_D \tag{1.59}$$

$$C_T = \pi (R_o^{DT})^2 N_T \tag{1.60}$$

N_D and N_T are the donor and trap surface number densities, and R_o^{DD} and R_o^{DT} are the Förster-type energy transfer distances for donor to donor and donor to trap transfer, respectively.

The results given above are for the two-dimensional case because energy transfer between dye molecules attached to insulator or

semiconductor surfaces is more likely to occur in two rather than three dimensions. In the case of an insulator, e.g., glass or fused silica, where the possibility of electron injection or energy transfer to the substrate is very unlikely, the quantity of interest is the probability that the excitation resides on a particular type of molecule, whether it be donor or trap. The donor molecules are usually the monomer form of the organic dye molecules while the traps consist of nonfluorescent dimers or higher aggregates [30].

The next chapter discusses experiments measuring the lifetime shortening of a dye molecule, cresyl violet, adsorbed on the surface of an insulator, fused silica. The fluorescence profiles are collected using the picosecond time-correlated single photon counting technique. These profiles are then fit with various decay models including single exponential, bi-exponential, two-dimensional Förster decay, and two-dimensional Fayer decay along with certain combinations of these models in order to better characterize the excitation transfer processes between molecules on surfaces. Later chapters will examine possible mechanisms for excitation transfer from organic dye molecules to wide bandgap semiconductors such as TiO_2 and ZnO. Picosecond photon counting is used to examine these energy transfer processes with dye molecules spaced at various distances from the surface of the semiconductor and with the dye molecules directly adsorbed on the semiconductor surface.

CHAPTER II. AN EXPERIMENTAL STUDY OF EXCITATION TRANSPORT AND TRAPPING

Introduction

In this section the phenomena of excitation transport and trapping will be examined for essentially two-dimensional systems. The specific system that is considered is an organic dye molecule, cresyl violet (CV), adsorbed on the surface of an insulator, fused silica (quartz). The experimental details, results, and discussion are given in the following publication. The data collection technique of time-correlated single photon counting is described first, and some of the specifics of the sample preparation and characterization are given later.

Photon counting

The primary advantage of photon counting is that it allows acquisition of data with high statistical quality, thereby making it possible to accurately determine fluorescence lifetimes. With single photon counting, the data are obtained in the form of a probability distribution for single photon emission due to excitation of the sample. This probability distribution is actually the intensity versus time distribution of all emitted photons from the excited sample [54]. To obtain the probability distribution, a detector, usually a photomultiplier tube with a fast response to incoming photons, is used to detect the photons emitted by the sample due to repetitive excitation from a pulsed light source.

Figure 2.1 gives a block diagram for the experimental apparatus used to obtain the probability distributions (fluorescence decay profiles) in this experiment. The specifics about the equipment actually used are given in the experimental section of the publication; the following is a more general description of the time-correlated single photon counting concept.

The excitation source has to be capable of producing light pulses in a repetitive, reproducible manner. In our case, it consists of a synchronously pumped mode-locked dye laser system. The pump laser is a mode-locked argon ion laser which lases at 514.5 nm with pulses having a full width at half maximum (fwhm) of between two and three hundred picoseconds. These pulses are used to pump a solution of organic dye in a solvent (in our case Rhodamine 6G in ethylene glycol) flowing through a jet. The dye lases inside its cavity and a circulating pulse is formed which is synchronously amplified by the argon ion laser pulses. This synchronous pumping results in laser pulses having a fwhm of less than fifteen picoseconds. The pulse trains leaving the dye laser can be split by a beam splitter with one fraction used to trigger the photon counting electronics while the other fraction goes on to excite the chemical sample.

The photons emitted by the sample following excitation are focussed onto the photocathode of a high-gain fast photomultiplier situated at a right angle from the incident laser beam. The spread in transit time of the photoelectrons in the photomultiplier tube, PMT, is important in determining the width of the instrument response

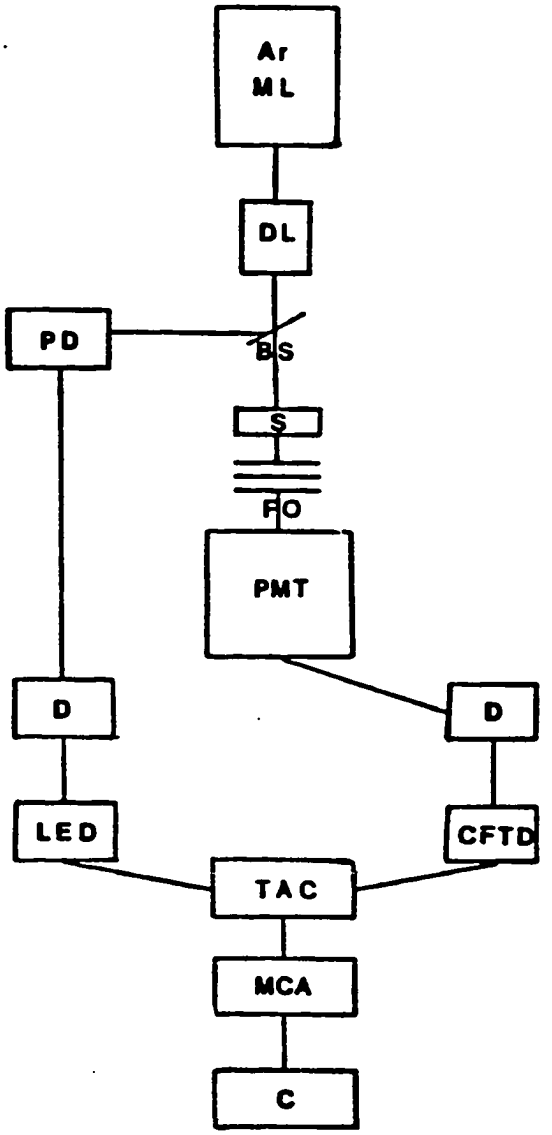

Figure 2.1. Block diagram for generalized picosecond photon-counting apparatus. Individual components are explained in the text. Specifics of the publication used in the experiment are given in the following publication

function which limits the time resolution of the system. The fluorescence photons strike the photocathode, which is made of a photoemissive material, and electrons are ejected. These photoelectrons are then amplified by a series of dynodes under high voltage until they reach the anode. The anode then sends out a signal to the photon counting electronics.

The heart of these electronics is the time-to-amplitude converter, TAC. When the trigger (START) pulses derived from the output of the laser reach the TAC, a charging voltage ramp is initiated on a capacitor inside the TAC. This charging ramp continues to build up until the signal from the photomultiplier tube (the STOP pulse) is received by the TAC. This halts the charging ramp, and the TAC then sends out a pulse, with amplitude proportional to the voltage across the capacitor, to the multichannel analyzer (MCA). Sometimes it is necessary to correct for nonlinearity of the TAC, which is associated with the sweep of the voltage ramp. The correction can be made by collecting a data file in the MCA obtained using temporally random stop pulses. This file can be used in the deconvolution of the experimental data in order to remove the artifacts due to TAC non-linearity.

The MCA makes use of an analog-to-digital converter to sort and accumulate the signals from the TAC. These signals are stored in data channels which are arranged according to the measured amplitudes of the TAC pulses. The signals due to early time events are stored in lowest-numbered channels while those due to later occurring emission

are stored in the higher-numbered channels. As long as the excitation and fluorescence intensities are low, the detected fluorescence photons will be due to excitation by single photons. The fluorescence photons are collected until the desired number of counts in the peak channel is obtained. If the photon counting electronics are configured to operate in the "inverted mode", as was the case in this experiment, the early time events are stored in the higher-numbered channels and the later time events are stored in the lower-numbered channels. To configure the electronics in this manner the detected fluorescence photons are used to derive the START pulses and the STOP pulses are obtained from the excitation source. For excitation sources having a high repetition rate, this configuration allows many more of the fluorescence signals to be processed by the TAC than is possible in the normal configuration in which START and STOP pulses are derived from excitation and fluorescence pulses respectively.

In order to achieve time correlation between the START and STOP pulses, delays are present in both paths for signals from the PMT and from the trigger source. When these delays are appropriately set, a STOP and a START pulse will be derived from the same initial laser pulse. Also the delays can be varied slightly to position the collected fluorescence decay profile in the proper channels of the MCA so that the maximum amount of usable data are obtained within the MCA window.

The actual output of the PMT consists of pulses with varying amplitudes. Among these pulses are those due to the dark current of

the PMT, single photon events, and multiple photon events. To remove the undesired pulses, i.e., those due to dark current and multiple photon events, the PMT output is routed through a discriminator. The effect of the discriminator is to improve the signal-to-noise ratio and to provide the TAC with pulses of constant amplitude that are independent of the original shapes of the pulses coming from the PMT. Leading edge discrimination is acceptable for pulses having little variation in amplitude, e.g., pulses from the trigger source. In leading edge discrimination, pulses above and below certain preset values are rejected and the discriminator monitors the incoming or leading, edge of the pulse. If there is a fairly wide variation in the pulse heights a leading edge discriminator can give rise to fairly large errors in estimating the time of arrival of the pulses. O'Connor and Phillips [54] have demonstrated the kind of timing errors that would result for pulses arriving at the same time but having different amplitudes. To obtain the correct arrival times, a constant fraction timing discriminator is used for the pulses coming from the PMT. When a constant fraction timing discriminator (CFTD) is used, the timing of the pulses occurs at a point on the leading edge that is a constant fraction of the pulse height. The timing point will be the same for those pulses having the same shape but differing heights.

In an ideal situation, the response of the instrumentation would be infinitely fast as long as the excitation pulses were infinitely narrow. If this were the case, the fluorescence decay profile obtained would be for the true fluorescence decay profile G(t). In

reality, the recorded decay profile (I(t)) will differ from G(t) because the excitation pulses have a finite pulse-width and the photon counting electronics have a nonzero response time. I(t) can be expressed as a convolution of the true decay with the instrument response function (E(t)) to give the relationship

$$I(t) = \int_0^t E(t-t')\, G(t')dt' \qquad (2.1)$$

For the situations where E(t) is extremely narrow compared to the fluorescence lifetime of interest the collected decay profile will be a very good approximation to the true decay profile; otherwise the true decay is obtained by deconvolution of the measured decay with the instrument response function.

Experimentally, the instrument response functions are obtained by collecting excitation light that has been scattered off a material that does not emit in the spectral region being studied. This material is positioned so that the collection geometry of the focussing optics is the same as when the sample is examined. The primary factors in determining the width of E(t) are the finite lifetimes of the excitation pulses, the distribution of times required for photoelectrons to travel from cathode to anode in the PMT, and the difference in arrival timing for signals to the photon counting electronics due to intrinsic jitter in the electronics and discriminator walk caused by differing pulse amplitudes in the signals from both the trigger source and the PMT. Robbins [55] discusses

these factors and the contribution that each makes to the instrument response function width. He states that for most systems the intrinsic jitter is on the order of twenty to twenty-five picoseconds. For a synchronously pumped dye laser system the widths of the excitation light pulses are very short (<15ps) and are not an important contribution. Robbins [55] concludes that the principal contributions to the width of E(t) comes from the timing walk in the discriminators and the photoelectron transit time in the PMT. He examined a number of PMT-discriminator combinations and found instrument response function widths varying from about 200 picoseconds to about 650 picoseconds. It is difficult to determine the exact contribution of discriminator walk, since it depends on the variation in amplitude of the incoming pulses. The photoelectron transit time in the PMT depends upon the path and the initial velocity of the photoelectrons and secondary electrons; it can be optimized by adjusting the potentials between the photcathode, the focussing grid, and the first few dynodes.

The fluorescence decay profiles collected with the time-correlated single photon counting method are of high statistical quality and obey Poisson probability statistics [56]. According to Poisson statistics, the mean of a Poisson distribution of events recorded per channel can be estimated by the number of counts in that channel. In other words, the mean number of events recorded in channel i, μ_i, is equal to N_i, the number of counts in channel i, and also σ_i^2, the variance. This implies that the uncertainty in the

number of counts in channel i, σ_i, is given by

$$\sigma_i = (N_i)^{1/2} \tag{2.2}$$

To reduce the ratio (σ_i/N_i) of uncertainty to number of counts it is necessary only to increase the number of counts. The easiest ways to accomplish this are to increase the amount of time for which data are collected, or to increase the rate at which data are collected. For example, if the number of counts in the channel containing the largest number counts is 10,000, the precision of the data will be

$$\frac{\sigma_i}{N_i} = \frac{1}{(N_i)^{1/2}} = \frac{1}{(10,000)^{1/2}} = \frac{1}{100} = 1\%$$

By increasing the number of counts by two orders of magnitude the data will become one order of magnitude more precise. The more precisely the data are determined, the more accurately the analysis of the data can be carried out. The number of counts to which the data are collected depends upon various experimental conditions such as photodecomposition of the sample, intensity of the excitation source, and intensity of light reaching the PMT. Since the PMT can be damaged if the light intensity incident upon it is too great, the easiest way to increase the number of counts is to collect for larger periods of time, which will work as long as the emission from the sample does not drop off to unacceptably low levels during the counting time.

The analysis of the data consists of deconvoluting the measured decay profile from the instrument response function and fitting of the resultant true decay to various mathematical models. This is accomplished by use of a convolute-and-compare algorithm based on the Marquardt nonlinear least squares fitting technique [57]. The degree of accuracy with which a model fits the data is judged by two criteria. One criterion is the reduced chi-square (χ_r^2) which is a weighted sum of the square of the difference between the actual data points and the points determined with the fitting model. If the data obey the Poisson distribution, χ_r^2 should ideally be close to one. In reality acceptable χ_r^2 values can range from 0.8 to 1.2 [57], since there is thought to be a small non-Poissonian contribution to the noise in photon counting experiments. Also, χ_r^2 does not take into account some systematic deviations of the fitted curve from the experimental data. Therefore, χ_r^2 by itself is not adequate for determining the quality of the fit. A second criterion, the autocorrelation function of the residuals, must also be examined. The autocorrelation of residuals is based upon the concept that a model which perfectly fits the true decay profile will have an autocorrelation function which is randomly distributed about zero. The residual is defined as the difference between the experimental data points and the corresponding points on the curve obtained from the fitting model. The autocorrelation function (C(t)) of the weighted residuals (Δi) is calculated from the equation

$$C(t_j) = \frac{\frac{1}{m} \sum_{i=1}^{m} (w_i)^{1/2} \Delta i (w_{i+j})^{1/2} \Delta_{i+j}'}{\frac{1}{n} \sum_{i=1}^{n} W_i \Delta i^2} \qquad (2.3)$$

where

$$W_i - \frac{\frac{1}{F_o(t_i)}}{\frac{1}{n} \sum_{i=1}^{n} \frac{1}{F_o(t_i)}}$$

is the weighting factor,

$F_o(t)$ is the experimentally determined fluorescence decay curve, $F_c(t)$ is the decay curve calculated from the model, n is the number of channels used to collect the data, and m is the number of terms in the numerator [57]. If the data points are randomly distributed about the calculated curve and the number of channels is infinite, then each residual is perfectly correlated with itself and the autocorrelation function is zero everywhere. However, the number of channels is not infinite so the autocorrelation function exhibits oscillations of low amplitude and high frequency when plotted versus the correlation channel. If the data are not randomly distributed about the proposed decay model, then the autocorrelation function exhibits periodic low frequency oscillations as well [54]. A particular model is thought to fit the data only when the reduced chi-square is low and the autocorrelation of the residuals has oscillations due solely to

statistical, and not systematic, deviations. Examples of data fit with models satisfying these criteria are given in the following publication, but next some details pertaining to the preparation and characterization of the samples will be given.

Sample preparation and characterization

The samples used in this experiment consisted of an insulator with less than a monolayer of organic laser dye molecules adsorbed on the surface. The dye molecule used was cresyl violet (CV), which was chosen because its absorption spectrum [35] indicated a favorable overlap with the usable wavelengths of light emitted by the synchronously pumped dye laser. CV in solution has a peak absorbance at 601 nm with a maximum absorption coefficient of 7.5×10^4 l mol^{-1} cm^{-1} at this wavelength [35]. The laser wavelength used in the experiment was 585 nm, which was the shortest wavelength attainable in a Rhodamine 6G laser without significant reduction in power. Other available sample dyes that were considered were Rhodamine B and Rose Bengal. It turned out that these dyes absorbed too far to the blue to be effectively excited by the laser system. The quartz substrates were prepared by cutting a piece of optically polished fused silica, 2 millimeters thick, into sections measuring approximately one centimeter by one centimeter. By using an insulator for the substrate, it should be possible to examine the excitation transport

and trapping among dye molecules without observing complications due to dye → surface nonradiative decay.

The purity of the CV was checked by means of Thin Layer Chromatography (TLC). The TLC plates were obtained from Analtech, and the solvent mixture used was acetic acid:ethanol (approximately 80:20 by volume). These TLC experiments showed only one spot from CV, even when examined under ultraviolet light. The solutions used to deposit CV on quartz were prepared with ethylene glycol as the solvent for several reasons. Aqueous solutions of CV were not easily made because CV did not readily dissolve in water. Also at the higher concentrations (10^{-5} M and greater) CV existed in predominantly dimeric form in aqueous solution. Methanolic and ethanolic monomer CV solutions were easily prepared. However, when the solutions were placed on the substrate, the solvent rapidly evaporated resulting in dye layers that were extremely nonuniform and nonreproducible. With ethylene glycol as the solvent, the solutions were easy to prepare and the adsorbed dye was deposited more uniformly and reproducibly. The solutions were prepared by initially making a stock solution having a concentration of 10^{-3} M and then diluting aliquots of this stock solution in order to obtain a series of solutions covering about three orders of magnitude. The actual solution concentrations were determined from the absorption spectra taken with a Perkin-Elmer ultraviolet-visible dual-beam recording spectrophotometer using ethylene glycol as a reference.

The deposition or coating of the substrates was performed in the following manner. A few drops of a CV-ethylene glycol solution were placed on the fused silica substrate and left for approximately five minutes to establish equilibrium between dye adsorbing on the surface and dye remaining in solution. Leaving the solution in contact with the substrate for longer periods of tme produced no discernible difference in the amount of adsorbed dye. After the equilibrium had been established, the excess solution was spun off using a centrifuge. By centrifuging the samples at 1500 rpm for about one minute the solvent and excess solution were removed in a uniform fashion. In order to remove the adsorbed dye, if the same substrate was to be reused, the sample was rinsed in methanol and distilled water. Extra care was taken in preparing the samples to ensure that no finger oils reached the samples as these were found to fluoresce in the spectral region being studied.

Two methods were used to characterize the samples. The first was measurement of the absorption spectra on the Perkin-Elmer 320 spectrophotometer. These spectra indicated that CV adsorbed on the quartz in primarily the dimer form. This was discovered by comparing the absorption spectra of the samples to absorption spectra of CV in aqueous solutions at higher concentrations. Further studies indicated that this is also the situation when other dyes of the oxazine family, e.g., Nile Blue or Oxazine 750, were adsorbed on quartz. The second method consisted of scanning the laser beam over the surface of the sample. This was done by moving the sample with a translatable holder

driven by a computer-controlled stepper-motor while the laser beam was kept in a fixed position. The fluorescence intensity was monitored with the multichannel analyzer operated in the multichannel scaling (MCS) rather than pulse height analysis (PHA) mode. In this way, the uniformity of the deposition was monitored and only for areas of the samples where the coating was fairly homogeneous were fluorescence decay profiles measured.

The surface number densities of CV molecules adsorbed on the substrate were calculated from the absorption spectra of the samples. According to Beer's Law, the optical density is given by

$$\log\left(\frac{I_o}{I}\right) = \varepsilon\, bc = \sigma\, Nx \qquad (2.4)$$

in three dimensions, where ε is the molar extinction coefficient in liters $\cdot$ mole^{-1} $\cdot$ cm^{-1}, C is the concentration in mole $\cdot$ l^{-1}, b is the path length in cm, σ is the absorption cross section in cm^2, N is the number of absorbers per unit volume with units cm^{-3}, and x is related to the pathlength and also has units of cm. In two dimensions, the expression becomes

$$\log\left(\frac{I_o}{I}\right) = N_s\, \sigma \qquad (2.5)$$

where N_s is the surface number density given with units cm^{-2}. The absorption cross section can be obtained from the molar extinction coefficient. For CV monomers the extinction coefficient is 7.5×10^4

$l \cdot mole^{-1} \cdot^{-1}$ at 601 nm in solution. This means that the absorption cross section is

$$\sigma = \frac{\varepsilon C}{N} = \frac{\varepsilon \ (1 \text{ mole} \cdot l^{-1}}{(6 \times 10^{23} \text{ molecules} \cdot 10^{-3} \text{ cm}^{-3})}$$

$$= \frac{7.5 \times 10^{4} \ l \cdot mole^{-1} \cdot cm^{-1} \ (1 \text{ mole} \cdot l^{-1})}{(6 \times 10^{23} \text{ molecules} \cdot 10^{-3} \text{ cm}^{-3})} = 1.3 \times 10^{-16} \text{ cm}^2.$$

The molecular area of the CV monomer is approximately 10^{-14} cm^2. In two dimensions a complete monolayer will occupy 10^{-14} cm^2 or N_s will have a value of 10^{14} cm^{-2} and the resulting optical density will be

$$\log\left(\frac{I_o}{I}\right) = N_s \sigma = 10^{14} \text{ cm}^{-2} \cdot (1.3 \times 10^{-16} \text{ cm}^2)$$

$$= 1.3 \times 10^{-2}$$

This is very close to the optical density of 10^{-2} that Spitler and Calvin [10] gave for a monolayer of dye adsorbed on a surface. Since CV was found to exist mainly in the dimer form when adsorbed on TiO_2 the numbers are actually somewhat different. The maximum extinction coefficient was found to be 1.04×10^5 $l \cdot mole^{-1} \cdot cm^{-1}$ which gives an absorption cross section of 1.7×10^{-16} cm^2. If the molecular area of the dimer is assumed to be twice that of the monomer, or 2×10^{-14} cm^2, then N_s for a monolayer of dimers is 5×10^{13} cm^2 and the optical density is 8.5×10^{-3} which is still approximately 0.01. The absorption spectra for the samples indicate that in all cases less

than a monolayer of dye has been deposited. At the highest solution concentration studied, the surface coverage was about one-third of a monolayer while the lowest concentrations resulted in surface coverages of less than one-tenth monolayer. The actual values for surface optical density and surface number density are given in the following publication.

Excitation transport and trapping in a two-dimensional disordered system: Cresyl violet on quartz

Picosecond photon counting fluorescence profiles have been evaluated for cresyl violet (CV) adsorbed on amorphous quartz with submonolayer coverages ranging over more than two orders of magnitude. A number of model functions for the time-dependent fluorescence intensity have been tested by nonlinear least squares convolute-and-compare analysis of the profiles. The autocorrelation functions of the resulting residuals provide a sensitive criterion for the model functions. Convolutions of single-exponential, biexponential, and two-dimensional Förster-type decay models with the instrument function yield poor autocorrelations, while a fluorescence intensity model function of the form $I(t) = A_1\exp(-t/\tau_1) + A_2\exp[-t/\tau_2 - 1.354\ C_T(t/\tau_2)^{1/3}]$ yields autocorrelation functions which are dominated by statistical noise. The observed long-time fluorescence decay at most coverages is consistent with emission by adsorbed CV monomers, with time dependence governed by two-dimensional

excitation trapping by CV dimers. No conclusive evidence for CV dimer fluorescence is found. CV orientational diffusion on the surface is shown to be unimportant. The range of applicability of the Loring-Fayer two-body approximation to the master equations for energy transport and trapping in two-dimensional disordered systems has been tested for our CV coatings on quartz and is found to be marginally valid for the lowest coverages studied, for which the reduced dimer (trap) density is less than ~ 0.25.

Introduction

Energy transport and trapping processes involving organic dye molecules are relevant to the efficiency of dye sensitizers on semiconductor surfaces in liquid-junction solar energy cells [58,59] and have received considerable recent theoretical study in two-dimensional [30,60] and three-dimensional [50,51,52,61,62] systems. Coating ultraviolet-bandgap semiconductors such as TiO_2 with a visibly absorbing dye has been proposed for extending solar cell photoconductivity response to overlap the solar blackbody spectrum [58,59]. Similar sensitization of visible photoconduction in organic molecular crystals has yielded sensitive probes of electrolyte-dissolved dye concentrations at the picogram level [63]. For such dye coatings, photoejection of an electron from an electronically excited dye monomer into the solid is expected to compete with (a) radiative decay of the S_1 state of surface-adsorbed monomers, (b) intramolecular nonradiative decay of S_1 state monomers, (c) resonant electronic

excitation transport between adsorbed S_1 state and S_0 state monomers due to Förster-type dipole-dipole interactions [36], and (d) nonresonant excitation transport from S_1 state monomers to dye dimers and/or higher oligomers.

It is logical to focus on the dynamics of processes (a) through (d) by examining time-resolved fluorescence profiles of dyes adsorbed onto insulators into which the electron photoinjection channel is energetically closed. Kenmitz et al. [31] have recently carried this out for submonolayers of rhodamine B on naphthalene and on glass. The resulting fluorescence profiles exhibited more rapid decay at higher surface coverages, were invariably nonexponential, and could sometimes be simulated with a biexponential decay law. At higher coverages, excitation transport and trapping was clearly the primary decay route for fluorescing S_1 state rhodamine B monomers. The details of the experimental profiles were found to be consistent with the existence of two distinct monomer surface adsorption geometries, which exhibited phenomenological lifetimes differing by a factor of ~ 4. At the highest dye coverages, an additional, rapidly decaying single-exponential component appeared whose intensity increased with dye coverage; this was attributed to rhodamine B dimer fluorescence.

In an earlier study, Liang et al. [32] examined fluorescence decay for rhodamine B on glass at ~ .5 monolayer coverage. Like Garoff et al. [64], who studied rhodamine B on silica, they found that the adsorbed dye fluorescence lifetimes were far shorter than for

rhodamine B in dilute solution, presumably in consequence of excitation trapping by dye aggregates.

In this paper, we report a picosecond photon counting fluorescence study of cresyl violet (oxazine 9 [35], hereafter CV) adsorbed onto fused quartz. We address the following questions: (i) What are the number of identities of dye species which fluoresce? (ii) To what extent can a careful analysis of the fluorescence profiles differentiate among the accuracies of alternative model functions for the time-dependent fluorescence intensity? (iii) How uniquely can the final fluorescence decay parameters be determined from such an analysis without resort to independent knowledge of, e.g., the dye monomer surface number density? The total CV surface coverages are systematically varied over more than two orders of magnitude. A comparison of absorption spectra for CV on quartz with those of CV in dilute ethylene glycol solution indicates that CV dimers are far more prevalent on quartz than in alcoholic solution, and much of the laser absorption necessarily produces electronic excitation in CV dimers rather than monomers. We also obtained fluorescence profiles for rose bengal and rhodamine B on quartz. CV was chosen for detailed experiments, because the substantial overlap between its 600 nm monomers $S_1 \leftarrow S_0$ absorption band and our rhodamine 590 laser tuning bandwidth afforded higher fluorescence signal-to-noise ratios, and thus a much broader surface coverage range, than was possible with the other dyes. The surface deposition techniques - substrate coating with dye solution,

followed by centrifugation and evaporation [65] - are similar to those used in recent surface-adsorbed dye fluorescence experiments [31,32,64]. This approach prepares a surface coating in which the CV species are imbedded in solvent and air multilayers, rather than adsorbed onto clean, well-characterized surfaces in the ultrahigh vacuum sense. Our purpose in following established coating techniques is to facilitate comparisons between our results and the earlier work [31,32,64]. It is expected that the surface cleanliness of the insulators will have little influence on the energy transport/trapping dynamics on insulators, since the transport processes depend primarily on the dye Förster interaction parameters rather than on dye-surface interactions.

If the profiles of fluorescence components from individual emitting species can be separated, they may be compared with theoretical time-dependent excited-state populations N(t) corresponding to two-dimensional excitation transport and trapping. Several levels of approximation to the exact solutions $N_E(t)$ to the energy transport and trapping master equation [51] are available for disordered systems. The two-body approximations $N_2(t)$ to $N_E(t)$ may be obtained for <u>arbitrary</u> times and monomer and trap coverages from a Dyson equation in which the self-energy has been approximated by a sum of two-site graphs in the diagrammatic expansion of the Green function solution [52] to the master equation. Higher n-body approximation $N_3(t)$, <u>etc.</u>, may be analogously obtained, and are expected to converge to $N_E(t)$ in the limit of large n. The two-body approximations $N_2(t)$

are readily obtained in terms of inverse Laplace transforms of closed-form expressions in both three [52] and two [60] dimensions, while the three- and higher n-body approximations are much more involved [51,52].

When the trap coverage greatly exceeds the monomer coverage, so that negligible monomer-monomer excitation transfer occurs, the Förster limit [36] is obtained in which the excited state population is given exactly in two dimensions by [30].

$$N_F(t) = A\exp[-t/\tau - 1.354\ C_T(t/\tau)^{1/3}], \tag{2.6}$$

where τ is the fluorescence lifetime of isolated monomers and C_T is the reduced trap coverage. Kenmitz et al. [31] found that their fluorescence profiles for rhodamine B on naphthalene and glass were consistent with a sum of two expressions of the form of Equation (2.6) for two independently decaying excited dye monomer species, or with Equation (2.6) plus a single rapidly decaying exponential term.

The two-body approximations $N_2(t)$ to the master equation solutions $N_E(t)$ break down at high trap coverages and long times in three- [52] and two- [60] dimensional systems. The three-body approximation quantitatively describes transport and trapping phenomena with high accuracy over a wide range of monomer and trap concentrations in three-dimensional systems [52,66] but is very ill-behaved in two-dimensional system [67]. It is therefore pertinent to ask whether among the monomer and trap coverages studied here there

are regimes in which the Förster limit supplies a better description of the transport/trapping dynamics than, say, the two-body approximations $N_2(t)$ to the master equation solutions, and conversely whether such a low-order approximation can simulate the fluorescence decay where the Förster limit expression $N_F(t)$ fails.

Finally, at long times both the Förster population $N_F(t)$ in Equation (2.6) and the two-body approximation $N_2(t)$ [60] become indistinguishable from single-exponential decay. When fluorescence is emitted by two independent species with excited-state populations decaying by trapping processes, the apparent decay law will be biexponential if the photon counting instrument function profile obscures the early-time nonexponentiality in $N_F(t)$ or $N_2(t)$. The resulting variety of possible decay laws, coupled with the number of possible emitting species - monomers adsorbed onto surface with different configurations [31], dimers, etc. - requires a careful analysis of model function fits for fluorescence profiles in order to differentiate among alternative assignments of even the most prominent fluorescence components to a particular dye species.

Experimental section

An acousto-optically mode-locked argon ion laser pumped a synchronous dye laser containing rhodamine 590 to produce tunable picosecond pulses whose fwhm was shown by zero-background autocorrelation [66] to be ~ 15 ps. The ion laser was a Control Laser model 553-A with 6-W plasma tube operated at 26-A current, modulated

by a Harris Corporation H-401 mode-locker with H-402 RF driver to yield 5145-Å pulses with 47.614-MHz repetition rate and 170-mW average power. The dye laser was a Coherent Radiation model CR-599-01 tuned with a three-plate birefringent filter. Its output coupler was replaced by an extended cavity 95% reflector mounted on a Line Tool Co. translator for synchronization with the argon laser pulse repetition rate. Conversion efficiencies from argon to dye laser wavelengths averaged ~ 15% at 5850 Å, the wavelength used for most of the CV fluorescence experiments.

Fluorescence from CV samples on quartz was collected at a right angle from the laser beam using a 5-cm focal length quartz lens and focussed through a variable rectangular slit before impinging on a Philips XP2020Q photon counting phototube with DU photocathode. A 3 mm Schott RG-610 filter and a CVI dichroic filter (optical density ~ 2 at 5850 Å, <0.1 at 6300 Å) screened 5850-Å laser scatter from the phototube. Laser pulses were focussed with a 15-cm focal length quartz lens to a diameter of ~ 0.1 mm at the substrate surface, which was enclosed in a ~ 2ft x 2ft x 2ft dark chamber with entrance and exit baffle tubes ~ 1ft long. The dye laser polarization was purified with an Oriel 2730 linear polarizer prior to striking the coated substrate, which was oriented at Brewster's angle. With this arrangement, scattered laser light contributed negligibly to the measured fluorescence profile at all times for all CV samples.

Photocurrent pulses from the phototube were amplified and inverted using a Hewlett-Packard 8447D 26 dB preamplifier and EG & G

IT100 inverting transformer. Fluorescence profiles were obtained by picosecond time-correlated photon counting [67]. Amplified photocurrent pulses were passed through an Ortec 583 constant fraction discriminator before serving as START pulses in an Ortec 457 time-to-pulse height converter (TAC). STOP pulses for the TAC were derived by processing mode-locker driver synchronization output pulses through an Ortec 934 updating discriminator, and adjusting their delay with respect to incidence of START pulses using an Ortec 425A nanosecond delay box. TAC-processed output pulses were stored as fluorescence profiles in a Canberra Industries, Inc. Series 30 multichannel analyzer (MCA) operated in the PHA mode. Depending on the CV fluorescence decay timescale, profiles were stored in 511 MCA channels with a channel resolution of 6.25, 12.5 or 25 psec. Instrument functions for deconvolution of raw data were obtained by measuring time-correlated profiles of 612 nm laser pulses scattered from a clean quartz substrate, and were typically 275-300 psec fwhm (the major contribution arising from electron transit spread in the phototube). Fluorescence profiles were transferred to a Digital Equipment Corporation MINC-23 minicomputer system with dual floppy disk drive operating in an RT-11 environment with FB monitor. They were normalized for TAC nonlinearity and then analyzed with a FORTRAN IV convolute-and-compare algorithm built around the Marquardt nonlinear regression technique [68], which is capable of fitting data sets with an arbitrary mathematical model. Single-exponential, biexponential, and Förster-limit decay fits to CV fluorescence profiles were

efficient on the MINC-23 (~ 3 min. per six iteration deconvolution in the biexponential case), but the nonanalytical Anderson-Fayer-type decay fits typically required ~ 180 min. per deconvolution.

The cresyl violet was commercially obtained laser dye from Exciton and was used without further purification. The absorption spectrum of CV in dilute diethylene glycol solution, given in Figure 2.2(a), nearly replicates the one reported by Drexhage for CV in ethanol [35]. Surface substrates were optically polished fused quartz with $\lambda/4$ flatness obtained from George Behm and Sons, Dayton, OH. Coating these substrates by placing drops of methanolic CV solution on the substrate and permitting evaporation [32] resulted in macroscopically fluctuating CV surface coverages with large variations in fluorescence decay times. Use of ethylene glycol as coating solvent and substrate centrifugation during evaporation [65] reduced the point-to-point variations in phenomenological time constants τ to $\lesssim$ 10% in most samples for τ comparable to or larger than the instrument function width; sample inhomogeneity effects were further minimized by the small size of the focussed laser beam diameter.

For all but the lowest two CV surface coverages studied, the adsorbed CV absorption spectrum was measurable on a Perkin-Elmer 320 UV-visible dual-beam spectrophotometer (optical density threshold ~ 0.0005) with uncoated quartz as reference. The adsorbed CV optical densities at 5300 Å, the concentrations of CV solutions in ethylene glycol used for substrate coating, and estimated CV surface number are listed in Table 2.1. Within the considerable scatter in measured

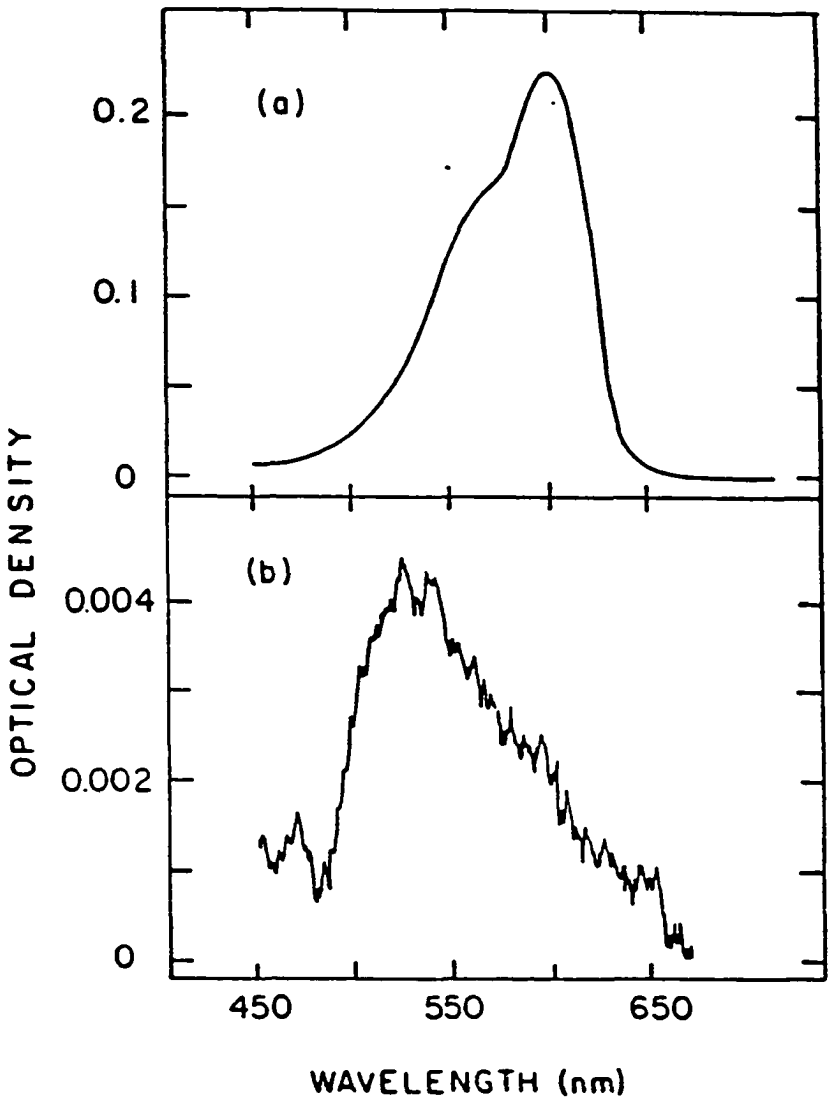

Figure 2.2. Comparison of absorption spectra cresyl violet in solution and on a surface. (a) Absorption spectrum of 3.04×10^{-6} M cresyl violet in diethylene glycol, 1-cm path length; (b) absorption spectrum of cresyl violet on quartz, sample 1 of Table 1

Table 2.1. Cresyl Violet Sample Characteristics

Sample	Concentration in diethylene glycol coating solvent (M)	Surface optical density ±0.0005	Surface number density (cm^{-2})
1	6.78×10^{-4}	0.0033	1.9×10^{13}
2	3.81×10^{-4}	0.0024	1.4×10^{13}
3	1.84×10^{-4}	0.0015	8.8×10^{12}
4	1.41×10^{-4}	0.0010	5.9×10^{12}
5	1.13×10^{-5}	--	--
6	3.04×10^{-6}	--	--

adsorbed-CV optical densities, the latter correlate monotonically with the concentrations of coatings solutions. A typical adsorbed-CV absorption spectrum is given in Figure 2.2(b). The substantial blue shift from ~ 6010 Å to ~ 5300 Å of the surface-adsorbed CV spectrum, along with the appearance of a long-wavelength tail not present in the spectrum of CV in ethylene glycol, render Figure 2.2(b) analogous to the solution absorption spectra of dye dimers reported for rhodamine B, sulforhodamine B [69], eosin, fluorescein [70], rhodamine 6G [71], and rose bengal [72]. The blue-shifted bands of such dimers have been interpreted [72-74] as arising from $\psi_+ \leftarrow \psi_0$ transitions from the ground states which result from strong mixing of degenerate ground state monomer-excited-state monomer states by the electric dipole-dipole interaction. Effects of vibronic coupling on dimer absorption spectra have been discussed by Beddard et al. [69].

We show in Figure 2.3 the absorption spectrum of 2.96×10^{-6} M CV in water, which resembles that in Figure 2.2(b) apart from a ~ 100 Å solvent shift, we obtain $\varepsilon_{max} = 1.04 \times 10^5$ ℓ/mole•cm at 5200 Å assuming complete dimerization in water (vs $\varepsilon_{max} \sim 7 \times 10^4$ ℓ/mole•cm of 6010 Å for CV monomers in ethanol [35]. This extinction coefficient (which provides a lower limit for ε_{max} for dimers in water) is used to estimate CV molecular number densities for the samples whose optical densities are listed in Table 2.1. The largest CV number density in Table 2.1. is ~ 1 order of magnitude smaller than required for monolayer CV coverage on a flat surface, so the dye coating on amorphous quartz may be regarded as a two-dimensional

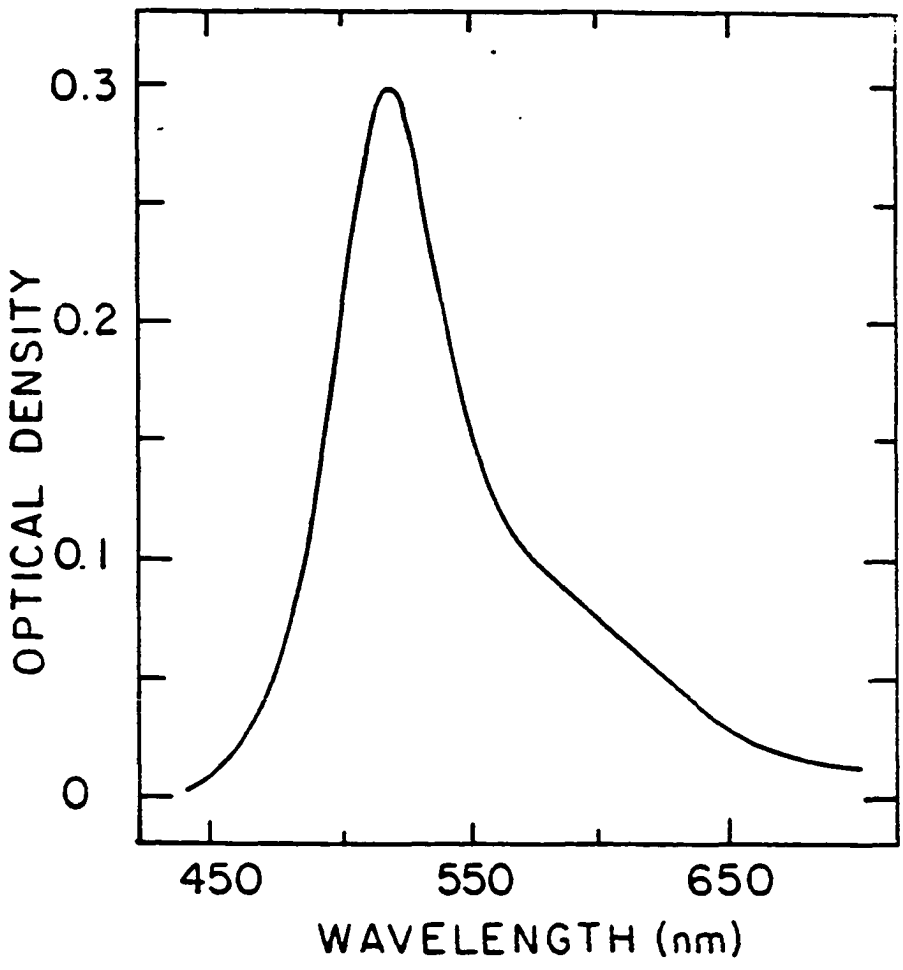

Figure 2.3. Absorption spectrum of 2.96×10^{-6} M aqueous cresyl violet solution, 1-cm path length

disordered system for all experimental conditions used here. The absorption spectra of adsorbed CV in samples 1-4 of Table 2.1., which all exhibit intense 5300 Å bands without prominent features near 6010 Å (the CV monomer band position in ethanol [35], clearly indicate that the surface densities of CV dimers in these higher-density samples are considerably larger than those of CV monomers. The moderate spectral broadening of the 5300 Å band in Figure 2.2(b) relative to the shape of the $\psi_+ \leftarrow \psi_0$ dimer band in solution (Figure 2.3) may be evidence of formation of higher oligomers on the surface.

Convolute-and-compare analysis

For an assumed fluorescence decay law N(t), the convolute-and-compare algorithm forms the discrete convolution C_n of N(t) in the nth channel,

$$C_n = \sum_{i=1}^{n} x(i-s)N(n-i), \tag{2.7}$$

where x(k) is the value of the instrument response function stored in the kth MCA channel using laser light scattered from a clean quartz substrate. The shift parameter s arises primarily from the laser tuning wavelength dependence of the laser pulse phase shift relative to the arrival time of STOP pulses derived from the mode-locker synchronization output. Besides the Förster limit decay law $N_F(t)$ (Equation (2.6)), we used as initial trial decay functions the single- and biexponential forms

$$N_e(t) = A\exp(-t/\tau) \tag{2.8}$$

$$N_b(t) = A_1\exp(-t/\tau_1) + A_2\exp(-t/\tau_2) \tag{2.9}$$

as well as the decay law for a single emitting species which obeys the Loring-Fayer two-body approximation [52] to the master equations for two-dimensional energy transport and trapping [60]

$$N_2(t) = A\exp(-t/\tau)G^D(t). \tag{2.10}$$

Here $G^D(t)$ is the inverse Laplace transform of

$$\hat{G}^D[0,\varepsilon] = \frac{[\hat{G}^S(\varepsilon)]^2}{\hat{G}^S(\varepsilon) - \tilde{\Delta}_2[0,\hat{G}^S(\varepsilon)]} \tag{2.11}$$

with

$$[\hat{G}^S(\varepsilon)]^{1/3} = [\frac{1}{2\varepsilon} + \sqrt{\frac{1}{4\varepsilon^2} + \frac{C^3}{27}}\,]^{1/3} + [\frac{1}{2\varepsilon} - \sqrt{\frac{1}{4\varepsilon^2} + \frac{C^3}{27}}]^{1/3} \tag{2.12a}$$

$$\tilde{\Delta}_2[0,\hat{G}^S(\varepsilon)) = 2^{1/3}\,\frac{\pi C_M[\hat{G}^S(\varepsilon)]^{4/3}}{3^{3/2}\tau^{1/3}} \tag{2.12b}$$

$$C = \frac{2\pi}{3^{3/2}\tau^{1/3}}\,(2^{-2/3}C_M + C_T). \tag{2.12c}$$

$\hat{G}^D[0,\varepsilon]$ is inverted numerically using the Stehfest algorithm [75]. It contains three adjustable parameters: the isolated-monomer

lifetime τ, and the reduced monomer and trap surface densities

$$C_M = \pi(R_o^{MM})^2 \rho_M \tag{2.13a}$$

$$C_T = \pi(R_o^{MT})^2 \rho_T \tag{2.13b}$$

The monomer and trap surface number densities are ρ_M and ρ_T; R_o^{MM} and R_o^{MT} are parameters which characterize the orientationally averaged Förster monomer-monomer and monomer-trap excitation transfer rates [36]

$$w_{jk} = \frac{1}{\tau_M} \left(\frac{R_o^{MM}}{r_{ij}}\right)^6 \tag{2.14a}$$

$$v_{jk} = \frac{1}{\tau_M} \left(\frac{R_o^{MM}}{r_{ij}}\right)^6 \quad . \tag{2.14b}$$

The decay laws $N_e(t)$, $N_b(t)$, $N_F(t)$, and $N_2(t)$ nominally contain two, four, three, and four adjustable parameters, respectively. The additional parameters s and the zero-fluorescence baseline are introduced in the calculation of the convolution C_n in Equation (2.7). When the fluorescence decay is not strictly rapid compared to the 10.50 nsec laser pulse spacing, the 95.228 MHz periodicity was built into the modeling function to account for small contributions to the fluorescence profile from molecules excited by the laser pulse which preceded the one which appeared in the TAC window.

A Marquardt nonlinear regression [68] program was used to minimize

$$\chi^2 = \sum_i w_i(C_i - Y_i)^2 \qquad (2.15)$$

with respect to the adjustable parameters. Y_i denotes the number of counts accumulated in channel i, and the weight w_i in channel i was equated to $1/Y_i$. For slow decays, the final χ^2 was improved by assigning the baseline as an adjustable parameter, rather than estimating it from the portion of the TAC window for early times prior to excitation.

For single- and biexponential fits, the convolute-and-compare procedure converged to unique final parameter sets which were insensitive (< 1% variation in lifetimes for τ appreciably longer than the instrument function width, ~ 5% for τ comparable to the instrument function width) to initial parameter choices. (Biexponential fits with $\tau_2/\tau_1 \sim 1$ are a well-known exception to this uniqueness property [76].) χ^2 minimization using simultaneous variation of <u>all</u> parameters in $N_F(t)$ and $N_2(t)$, however, tended to produce convergence to local minima whose locations depended on initial parameter choice. This occurred in $N_F(t)$ because C_T and τ are coupled in the product $C_T(t/\tau)^{1/3}$ in Equation (2.6); for $N_2(t)$, the problem arose from the nearly symmetrical appearance of C_T and C_D in Equation (2.12). Initial Förster-limit fits using $N_F(t)$ and $N_2(t)$ were therefore

guided by setting τ at a physically reasonable value corresponding to a fluorescence lifetime of CV is solution.

Results

Fluorescence profiles are shown in Figure 2.4 for each of the samples listed in Table 2.1. Increasing the CV surface coverage on quartz accelerates the overall decay, in analogy to the fluorescence behavior reported by Liang et al. [32] and by Kenmitz et al. [31] for rhodamine B on insulators. Each of the trial functions $N_F(t)$, $N_e(t)$, $N_b(t)$, and $N_2(t)$ (Equations (2.6) and (2.8) - (2.12)) was tested on most of the profiles. Of these model functions, only $N_b(t)$ yielded convolutions of the instrument function which were good fits to the fluorescence profiles in Figure 2.4 ($1.1 < \chi^2 < 5.9$); these optimized convolutions are plotted as continuous lines in Figure 2.4. The final parameters for the biexponential fits are reported in Table 2.2. for the profiles analyzed in Figure 2.4. It should be noted that the derived short- and long-component lifetimes τ_1 and τ_2 are generally disparate by one order of magnitude, so that the final lifetimes obtained from minimization of χ^2 in these cases are relatively insensitive to initial parameter choice. The ratio $A_1\tau_1/A_2\tau_2$ of integrated fluorescence profiles for the long and short components varies from 0.020 (at the lowest CV coverage) to the order of 2.0. The fluctuations in this ratio at high coverages arise because in this limit, where τ_1 becomes much shorter than the instrument function width, the fractional uncertainty in τ_1 becomes large.

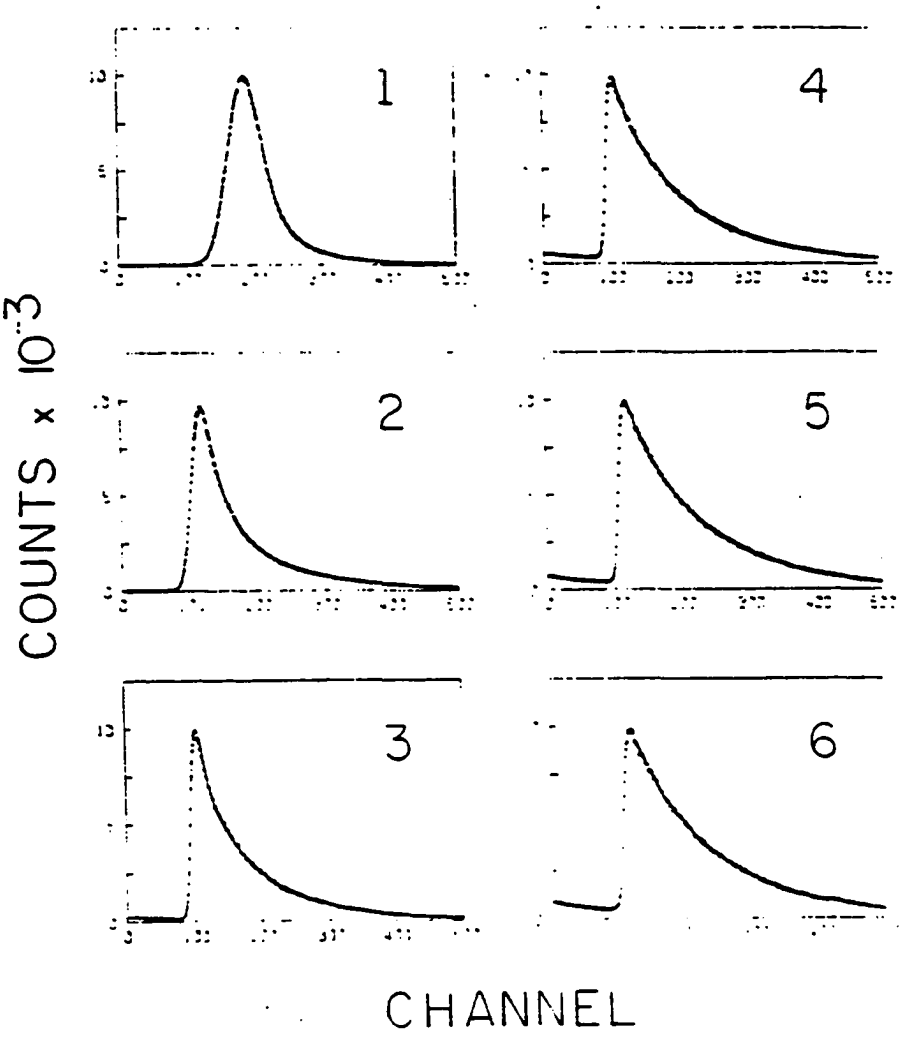

Figure 2.4. Typical cresyl violet fluorescence profiles from samples 1-6 of Table 2.1. The channel calibrations are 6.25 and 12.5 ps/channel for samples 1 and 2, respectively, and 25.0 ps/channel for samples 3-6. 10^4 counts were accumulated in the peak channel in each case. Continuous curves are biexponential fits, with optimized parameters listed in Table 2.2.

Table 2.2. Biexponential fitting parameters $N_b(t) = A_1\exp(-t/\tau_1) + A_2\exp(-t/\tau_2)$

Sample	A_1	τ_1, ps	A_2	τ_2, ps	$A_1\tau_1/A_2\tau_2$	χ^2
1	0.235	20.2	0.00519	392	0.428	1.42
2	0.0548	192	0.173	1143	2.04	5.89
3	0.0499	312	0.0522	2150	0.139	2.16
4	0.0349	220	0.0626	2653	0.0463	1.57
5	0.0320	185	0.0657	2862	0.0315	1.28
6	0.0183	216	0.0665	2927	0.0203	1.27

Since our CV deposition method produced nonuniform coverages on quartz, Table 2.3. gives the variations in final biexponential decay parameters for several randomly selected points on samples 4 and 6 of Table 2.1. While the point-to-point variations in τ_1 and τ_2 are substantial, they are smaller than the sample-to-sample variations of the average τ_2 for a given sample. Also included for both samples in Table 2.3. are biexponential fitting parameters for consecutive fluorescence profiles taken with the same 0.1-mm-diameter region exposed to the laser beam for counting periods of less than 6 min. The derived long-component lifetimes τ_2 are not significantly affected by these exposures (although the fluorescence count rate typically decreased 10% per counting period on sample 4, and 70% on sample 6), so the collected profiles show little evidence of contributions from photoproduct emission.

The inability of the elementary decay laws $N_e(t)$, $N_F(t)$, and $N_2(t)$ to reproduce the experimental profiles in Figure 2.4 suggests the existence of at least two emitting species. The conclusion of several emitting species was reached by Kenmitz et al. [31] for fluorescence from rhodamine B adsorbed on naphthalene and on glass. These workers used an expression of the form

$$N_{eF}(t) = A_1\exp(-t/\tau_1) + A_2\exp[-t/\tau_2 - 1.354\ C_T(t/\tau_2)^{1/3}] \quad (2.16)$$

to simulate some of their decays. This model function would correspond to two independently emitting dye ensembles: one decaying

Table 2.3. Local Variations in biexponential fitting parameters

Sample	A_1	τ_1, ps	A_2	τ_2, ps	χ^2
6	0.0203	216	0.0183	2927	1.27
	0.0264	176	0.0288	2941	1.14
	0.0314	120	0.0477	2945	1.28[a]
	0.0255	90	0.0533	2876	1.21
4	0.0291	336	0.0614	2660	1.35
	0.0328	276	0.0607	2642	1.76[a]
	0.0291	318	0.0615	2666	1.40
	0.0349	220	0.0626	2652	1.57

[a]Continued laser exposure of same substrate location as profile yielding parameters listed on previous line.

intramolecularly with lifetime τ_1, and the second decaying via excitation trapping in addition to intramolecular relaxation with lifetime τ_2. Such a mechanism for decay in the second ensemble would be applicable in the Förster limit where the reduced number of density of the second emitting species is negligible compared to C_T, the reduced number density of species responsible for trapping of excitation in the second species. The decay law in Equation (2.16) exhibits a high degree of parameter correlation in that changes in χ^2 in Equation (2.15) attending variations in one parameter are readily compensated by variations in the remaining parameters. Initial fits of Equation (2.16) to the profiles in Figure 2.4 were therefore performed with τ_2 fixed at 3000 ps, which approximates typical fluorescence lifetimes of CV monomers in dilute alcoholic solution [77]. The optimized parameters from the initial fits guided the choice of initial parameters in final fits, in which all of the parameters (including τ_2) were simultaneously varied in $N_{eF}(t)$. The values of the final parameters for the resulting fits, based on Equation (2.16), are given in Table 2.4. The optimized χ^2 values vary between 1.04 and 1.55, and are in most cases not significantly different from χ^2 for the biexponential fits. The corresponding convolutions of Equation (2.16) with the instrument function, if plotted on the scale of Figure 2.4, would be nearly indistinguishable in most cases from the displayed biexponential convolution.

Table 2.4. Fitting Parameters for $N_{ef}(t) = A_1 \exp(-t/\tau_1) + A_2 \exp[-t/\tau_2 - 1.354C_T(t/\tau_2)^{1/3}]$

Sample	A_1	τ_1 ps	A_2	τ_2, ps	C_T	χ^2
1	0.282	15.7	0.00770	436	0.377	1.39
2	0.252	8.8	0.0879	2432	1.97	1.55
3	0.119	22.2	0.118	3231	0.980	1.09
4	0.133	21.3	0.0866	3280	0.418	1.06
5	0.0700	38.6	0.0832	3381	0.306	1.04
6	0.0329	90.8	0.0776	3425	0.226	1.09

The qualities of fits based on the decay models $N_b(t)$ and $N_{eF}(t)$ may be differentiated by evaluating the respective autocorrelations of the residuals [76],

$$A_n = \left(\frac{N}{M}\right) \sum_{i=1}^{M} w_i^{1/2}(C_i - Y_i)w_{i+n}^{1/2}(C_{i+n} - Y_{i+n}) / \sum_{i=1}^{N} w_i(C_i - Y_i)^2. \quad (2.17)$$

Here N is the number of channels which comprise the fluorescence profile, and M is taken to be 250 channels. A_1, the autocorrelation in channel 1, is unity. For good quality fits, the autocorrelation function in channels for other n is dominated by random statistical fluctuations symmetrically scattered about $A_n = 0$. Systematic deviations $(C_i - Y_i)$ which alternate in sign between contiguous channel spaces (in consequence of using a functionally incorrect model N(t)) produce an autocorrelation function with well-defined low-frequency periodicity. We show in Figure 2.5 the autocorrelation functions computed for n up to 250 channels for the $N_b(t)$ and $N_{eF}(t)$ fits to each of the profiles of Figure 2.4. At the lowest CV coverage, the autocorrelation functions from both models are similar, implying that in this limit they provide similarly valid approximations to the data. For the four intermediate coverages (samples 2 through 5), the $N_{eF}(t)$ autocorrelations are markedly better than those from $N_b(t)$. Each of the profiles in Figure 2.4 exhibits similar counting statistics, since 10^4 counts were always accumulated in the peak channel. Hence, the normalization of A_n in Equation (2.17)

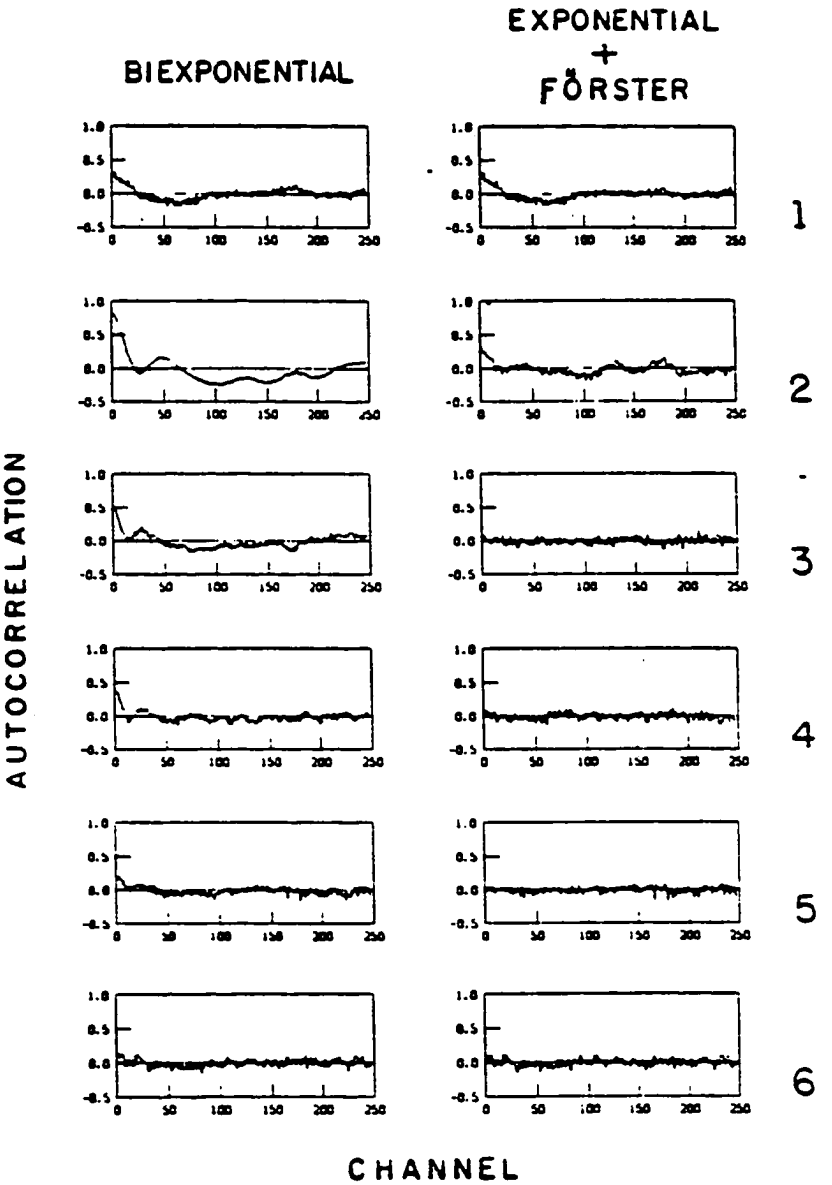

Figure 2.5. Autocorrelation function for biexponential and exponential plus Förster fits to profiles 1-6 in Figure 2.4

implies that the rms noise amplitude for an autocorrelation function in Figure 2.5 will be larger for the higher-quality fits, as is the case for the $N_{eF}(t)$ fits to the profiles from samples 2 through 5. At the highest coverage (sample 1), neither fit yields a statistical autocorrelation. In high-coverage profiles in which the decay is rapid relative to the instrument function width, the calculated convolutions are highly sensitive to the evaluation of the instrument function. The details of the latter are necessarily suspect because the phototube electron transit time distributions depend on the detected photon wavelength, and because the autocorrelation functions for both models in Figure 2.5 tend to worsen at higher coverages, where the instrument function becomes critical. The autocorrelation functions for $N_{eF}(t)$ fits with τ_2 fixed at 3000 ps (not shown in Figure 2.5) were intermediate in quality between those shown in Figure 2.5 for $N_b(t)$ and the fully optimized $N_{eF}(t)$. Since $N_{eF}(t)$ has the same number of adjustable parameters (with τ_2 fixed) as $N_b(t)$, the better autocorrelations from $N_{eF}(t)$ at intermediate coverages are not an artifact of higher functional flexibility, particularly since τ_2 varies little for the full-optimization fits in this coverage range (Table 2.4.). Finally, we give the fluorescence profile, single-exponential fit using $N_e(t)$, and autocorrelation function obtained from 5.0×10^{-6} M CV in aqueous solution in Figure 2.6. This profile was obtained using an analyzing polarizer inclined 54.7° from the laser polarization by Faraggi et al. [78] in order to remove the fluorescence anisotropy r(t) due to orientational relaxation by

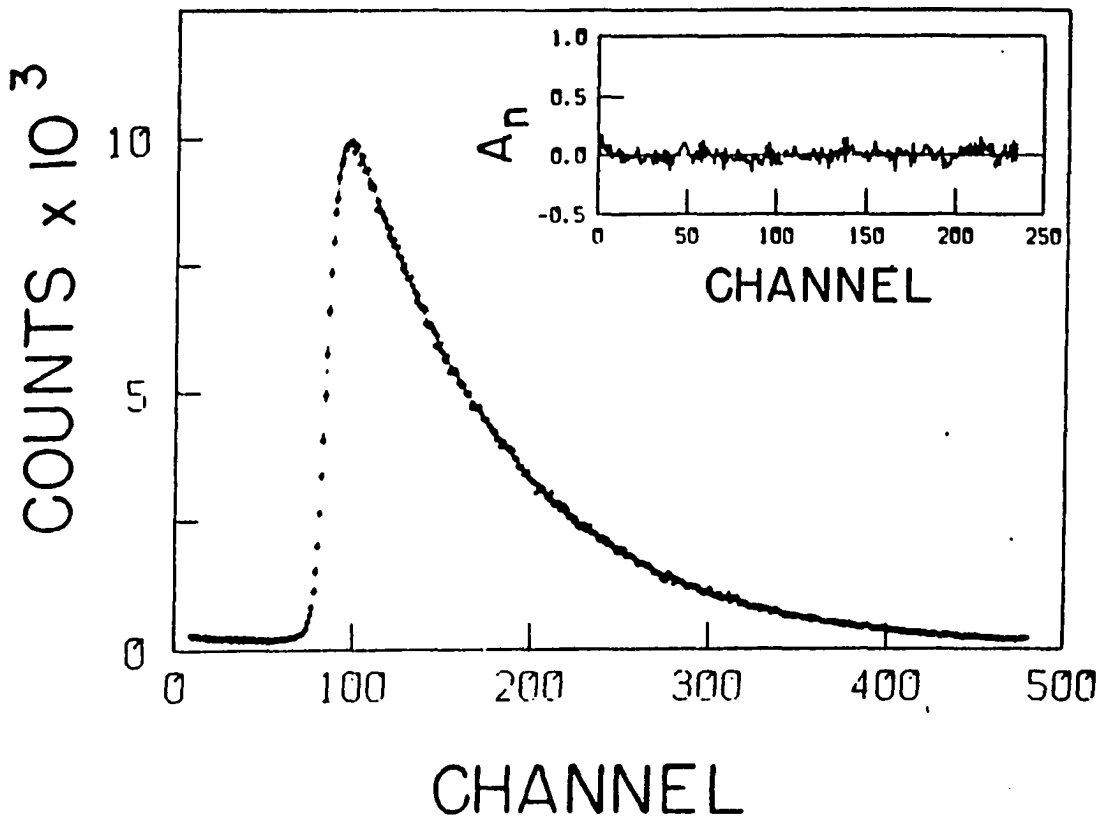

Figure 2.6. Fluorescence profile and autocorrelation function for single-exponential fit for 5.0×10^{-6} M aqueous cresyl violet solution with orientation fluorescence anisotropy suppressed. The optimized lifetime is 2235 ps, vs. 2390 ps reported in reference 79 for isotropic lifetime decay. Channel calibration is 25 ps

Sadkawski et al. [79], thereby rendering the measured profiles single-exponential. The autocorrelation in Figure 2.6 exemplifies the limiting quality of fits attainable with our apparatus.[1] Hence, the nonstatistical character of the autocorrelations for the $N_b(t)$ fits for samples 2-5 in Figure 2.5 does not arise from instrumental factors such as TAC nonlinearity.

Fluorescence spectra were evaluated for the samples in Table 2.1., using a J-Y H20 scanning monochromator operated with 0.5-nm bandpass and detecting the fluorescence with an Amperex 56DUVP photomultiplier. A typical fluorescence spectrum for adsorbed CV is shown in Figure 2.7; no evolution was observed in this spectrum, whose band maximum fluctuated between 6230 and 6290 Å over the coverages listed in Table 2.1. However, the biexponential fitting parameters in Table 2.2. predict that the time-integrated fluorescence intensity $A_1\tau_1$ for the short-lifetime component should become comparable to $A_2\tau_2$ at high concentrations, meaning the fluorescence spectrum should vary with coverage if the τ_1 and τ_2 components are emitted by species with different fluorescence spectra and similar oscillator strengths. The $N_{eF}(t)$ fitting parameters in Table 2.4., however, predict, in agreement with our flourescence spectra, that the short-component

---

[1]The autocorrelation functions for CV fluorescence in solution are particularly sensitive to the alignment of the 54.7° analyzer. A misalignment of ~ 5° yielded poor single-exponential autocorrelations for CV in ethanol and glycol, but gave statistical biexponential autocorrelations; the resulting biexponential lifetimes τ_1 and τ_2 for CV in ethanol were similar to those reported by Beddard et al. [80].

fluorescence should be masked by the long-component spectrum at all coverages if the short component does not exhibit a much larger transition moment than the long component. The position of the fluorescence band maximum in Figure 2.7 nearly coincides with that reported by Drexhage [35] for dilute CV solution in ethanol.

For all but the highest coverages, the two-species decay law $N_{eF}(t)$ is sufficient for yielding nearly statistical autocorrelations of the residuals. We attribute the long-component decay to CV monomer fluorescence because (i) the τ_2 parameter in the phenomenological biexponential fits of Table 2.2., which yields a statistical autocorrelation at the very lowest coverage (sample 6), converges in this limit to a value of ~ 3000 ps, within the range of solvent-dependent fluorescence lifetimes τ_f of CV in solution [79]; and (ii) fits based on the $N_{eF}(t)$ model yield nearly statistical autocorrelations with τ_2 between 3200 and 3450 ps at most coverages. The identity of the promptly emitting short-component species is more problematic. A priori, several of the possibilities are fluorescences from directly excited impurities, or directly excited CV monomers adsorbed onto the quartz with a different configuration than that of the CV species responsible for the long component τ_2, in analogy to the assignment suggested for one of the emission components from rhodamine B on insulators [31]. Impurity fluorescences are unlikely because we obtain good statistical autocorrelations for single-exponential fits for CV in dilute ethanol and ethylene glycol

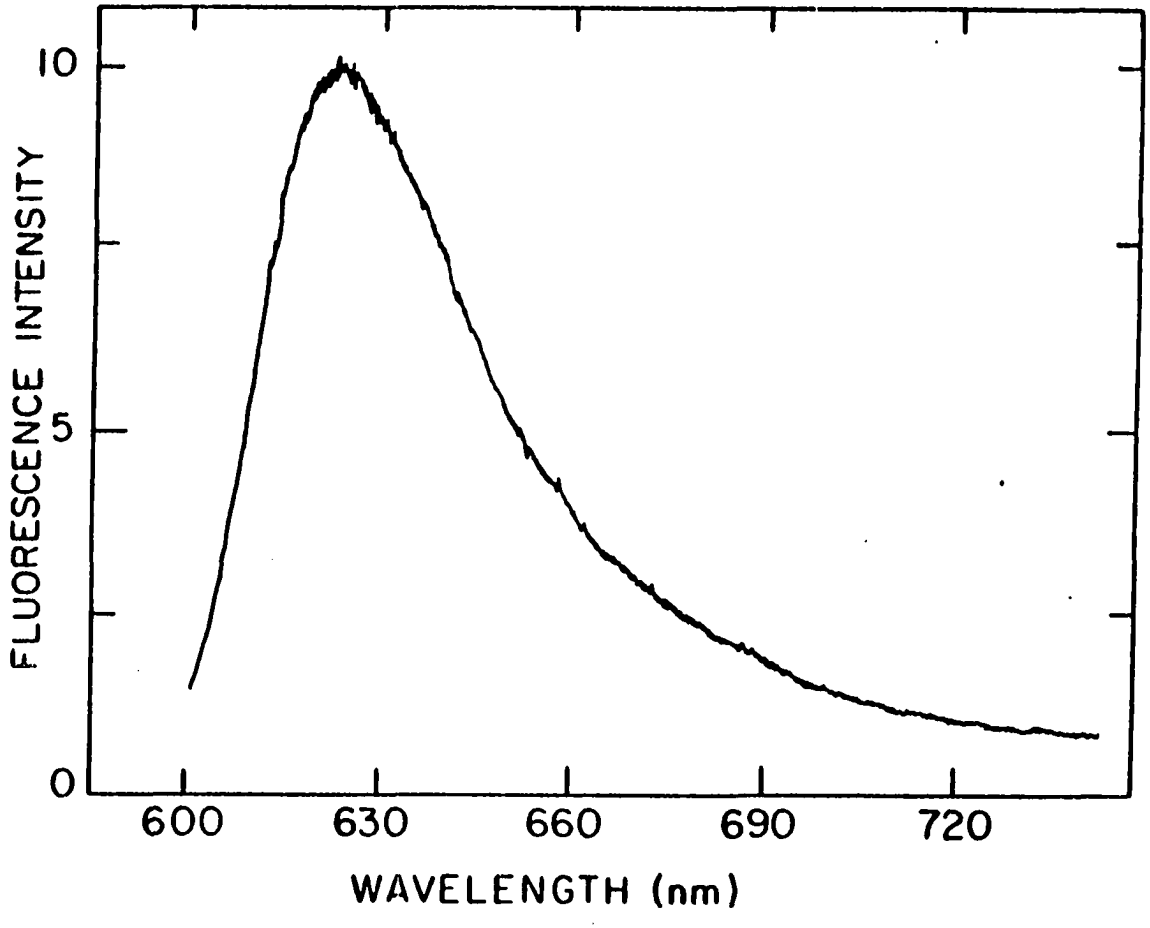

Figure 2.7. Fluorescence spectrum, uncorrected for instrumental response, for cresyl violet on quartz, sample 1 of Table 2.1

solutions, and because thin-layer chromatography of our CV solutions in ethanol yielded no extraneous bands. The lifetimes τ_1 of the short component extracted from the $N_{eF}(t)$ fits (Table 2.4.) are in the range 8.8-90.8 ps. These are subject to large statistical error because they amount to three channel widths at most, but they are so short compared to the CV monomer solution lifetimes that it is difficult to attribute them to CV monomers having special adsorption geometry. Another possible assignment is emission from the ψ_+ exciton component of CV dimers [69], which would be consistent with the large $\psi_+ \leftarrow \psi_0$ oscillator strength in CV (Figure 2.3). Picosecond $\psi_+ \rightarrow \psi_-$ internal conversion (IC) of the emitting ψ_+ state to a nonfluorescing ψ_- CV dimer state would be consistent with the observation that $S_n \rightarrow S_1$ IC is an ultrafast process in the majority of aromatic molecules [53]. Prompt emission by CV dimers is also favored by the predominance of dimer absorption in our adsorbed CV absorption spectra, which are typified by the spectrum in Figure 2.2(b). However, no dimer fluorescence appears in the aqueous CV profile in Figure 2.6 (which exhibits a statistical autocorrelation function with the single-exponential model $N_e(t)$), although this solution exhibits the CV dimer absorption spectrum in Figure 2.3. This indicates that in aqueous solution the ψ_+ state is so short-lived that its fluorescence profile is effectively swamped by fluorescence from a small concentration of CV monomers. It would thus be necessary to hypothesize that $\psi_+ \rightarrow \psi_-$ IC is appreciably slower on a quartz surface than in solution in order

to attribute our short emission component to CV dimers. While conceivable, such an assignment requires further proof.

Still another possibility is that orientational diffusion of adsorbed CV monomers on quartz, rather than a second CV species, produces the short emission component. In the presence of orientational diffusion, the detected fluorescence intensity would become [81]

$$I(t) = I_{\parallel}(t) + 2\, I_{\perp}(t) = \left[\frac{2}{3} + \frac{1}{3}\, r(t)\right] N(t), \qquad (2.18)$$

where r(t) is the time-dependent fluorescence polarization anisotropy. For isotropic rotational diffusion with diffusion coefficient D,

$$r(t) = \frac{2}{5}\, e^{-6Dt}. \qquad (2.19)$$

The fluorescence intensity for a CV monomer ensemble which undergoes orientational diffusion as well as Förster trapping decay will then obey

$$I(t) = \left[\frac{2}{3} + \frac{2}{15} \exp(-6Dt)\right] N_F(t)$$

$$= \left[\frac{2}{3} + \frac{2}{15} \exp(-6Dt)\right] A \exp\left[-t/\tau - 1.354\, C_T (t/\tau)^{1/3}\right]. \qquad (2.20)$$

Equation (2.20) is valid only if negligible monomer-monomer excitation hopping occurs during the monomer fluorescence profile, since such excitation transfer destroys orientational correlation in the emitting ensemble. This is exactly the regime in which the Förster limit applies. When the anisotropy function, proportional to exp(-6Dt), decays rapidly compared to $N_F(t)$, the decay law in Equation (2.20) will closely resemble $N_{eF}(t)$ [Equation (2.16)], particularly when the reciprocal of 6D spans only a few MCA channels. The $\exp(-t/\tau_1)$ term in $N_{eF}(t)$ would then phenomenologically represent the $\exp(-6Dt)N_F(t)$ term in Equation (2.20), with the consequence that τ_1 would shorten with increased CV coverage (owing to the more rapidly decaying $N_F(t)$ factor for larger C_T) when the profiles are fitted with the $N_{eF}(t)$ model. This behavior is exhibited by τ_1 in Table 2.4., although excessive significance should not be attached to this trend because τ_1 is never wider than three channels. Chuang and Eisenthal [82] have shown that for completely anisotropic rotational diffusion ($D_x \neq D_y \neq D_z$), r(t) contains five distinct exponential decay times. It is likely that adsorbed CV would rotate about one axis at most, yielding an essentially single-exponential anisotropy function.

We searched for effects of orientational diffusion by obtaining profiles using an analyzing polarizer aligned 0°, 54.7°, and 90° from the laser polarization. The three profiles were evaluated sequentially with unshifted laser beam exposure on two samples with CV coverages similar to those of samples 3 and 4. In both cases, analyses of the profiles yielded no polarization dependence

commensurate with that predicted for orientational diffusion (e.g., the r(t) term in I(t) should drop out entirely when the 54.7° polarizer is used). The foregoing discussion is based on three-dimensional orientational diffusion and adsorbed CV molecules may be constrained to rotate about axes with special orientations relative to the surface. The anisotropy function r(t) would then be different than in the three-dimensional case, but the fluorescence profiles would still exhibit a polarization dependence if r(t) were responsible for the rapidly decaying component. Hence, contributions from orientational diffusion can be ruled out.

The possibility that the short-lifetime component is scattered laser fundamental light was checked and discounted by testing the effect of an additional RG-610 filter (optical density > 2 at 585 nm) on the profiles.

In summary, the biexponential decay law fortuitously yields fits with low χ^2, and gives integrated fluorescence ratios $A_1\tau_1/A_2\tau_2$ which would be expected to cause observable spectral evolution in fluorescence emitted by samples 1-6. For profiles in which the decay is slow over the instrument function width, the $N_{eF}(t)$ model yields fitted functions whose deviations from the data points are smaller than the rms statistical noise. The long decay component in $N_{eF}(t)$ is CV monomer emission. The origin of the fast decay component is unproven, but it is not orientational diffusion, impurity fluorescence, or laser scattering. We caution that instrument function errors may contribute substantially to the fast component

under the present resolution: we have observed large fluctuations in the preexponential factors of the first (but not the second) term of $N_{eF}(t)$ from run to run using similar samples. We expect to resolve this question by incorporating a microchannel plate phototube with an instrument function of <80 ps in our apparatus. It is unnecessary to postulate more than two emitting CV species to account for our profiles. The fact that CV, unlike rhodamine B [35], exhibits an inherently rigid skeletal structure may account for the apparent absence of adsorption geometrical effects on CV fluorescence lifetimes, since Kenmitz et al. [31] attributed their rhodamine B lifetime dichotomy to contrasting rigidities of dye monomers adsorbed in different ways on the surface.

Excitation transport and trapping

We have shown that at all but the highest CV surface coverages, the fluorescence profiles are described within photon counting error by the model function $N_{eF}(t)$, the sum of a rapidly decaying single-exponential term and a term representing intramolecular plus Förster-type excitation trapping decay, whose lifetime approaches the fluorescence lifetime of CV monomers at low coverage. The Förster limit expression [Equation (2.6)] for monomer excitation trapping is valid when the reduced monomer density is negligible compared to the reduced trap density, $C_T/C_M \gg 1$ [30]; under this qualification, it will hold for arbitrary C_T. In the presence of trapping by CV dimers, the Förster limit is likely to be approximately obeyed in all samples

listed in Table 2.1. for which absorption spectra were obtained, since the latter are all strongly dominated by the 520 nm $\psi_+ \leftarrow \psi_o$ dimer band. The reduced trap densities C_T derived from the N_{eF} fits to the fluorescence profiles (Table 2.4.) extend from 0.226 to 1.97. For samples 2-4 (the ones for which approximate values of ρ_T are available in Table 2.1. and for which instrument function uncertainty is less critical to the accuracy of the fluorescence profile), C_T varies roughly linearly with p_T as predicted by equation 2.13(b). The derived R_0^{MT} parameter varies from 15 to 21 Å.

We now consider whether the Loring-Fayer two-body master equation solutions for transport and trapping in a two-dimensional disordered system can model the fluorescence profiles when combined with a rapidly decaying single exponential term,

$$N_{e2}(t) = A_1 \exp(-t/\tau_1) + A_2 \exp(-t/\tau_2) G^D(t). \qquad (2.21)$$

To compare the properties of this model function with those of $N_{eF}(t)$, we plot $[G^D(t) - f(t)]/f(t)$ vs. times for various C_T in Figure 2.8, where $f(t) = \exp[-1.354\ C_T(t/\tau)^{1/3}]$. This shows that when $C_M = 0$ and $t < 2_\tau$ the two-body function is a good approximation to the exact Förster expression for $C_T \lesssim 0.20$, and then fails badly for larger C_T. It is thus anticipated that Equation (2.21) should yield a fit of fair statistical quality to the profile from sample 6 (and of poorer quality for other). In practice, the number of independent parameters in convolutions of $N_{e2}(t)$ - A_1, A_2, τ_1, τ_2, C_M, C_T, s, and the base

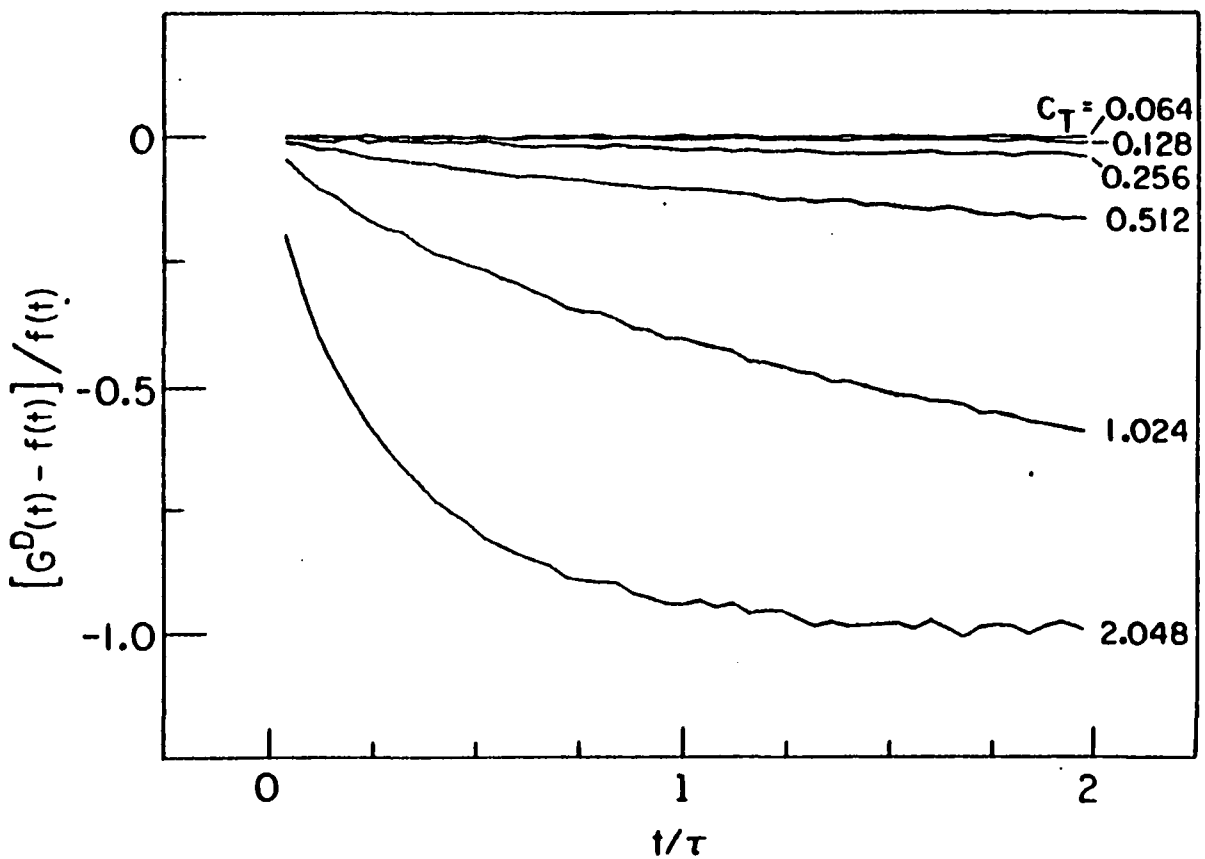

Figure 2.8. Comparison of the Loring-Fayer two-body approximation to $G^D(t)$ with $f(t) = \exp[-1.354C_T(t/t)^{1/3}]$. The time axis is calibrated in units of the monomer lifetime t

line parameter yield eight in all-leads to severe convergence problems in the convolute-and-compare analysis. The "true" optimized parameters are difficult to find even in samples in which $N_{e2}(t)$ yields a fair approximation to $N_{eF}(t)$, e.g., sample 6. Further, we found that in sample 3 an analysis based on $N_{e2}(t)$ fortuitously led to a low χ^2 (= 1.22) and a fair autocorrelation function, even though the $N_{eF}(t)$ analysis for sample 3 yields C_T = 0.980 (Table 2.4.). For such C_T, $N_2(t)$ is a poor approximation to $N_F(t)$, as shown in Figure 2.8. Hence, the final parameters from that analysis (C_M = 0.037, C_T = 0.679, τ_1 = 56 ps, τ_2 = 3.20 ns) must be regarded with suspicion. It is interesting to note that if the final parameters from the $N_{eF}(t)$ fits are simply substituted into $N_{e2}(t)$ and if C_M is set equal to 0, convolutions of $N_{e2}(t)$ yield computed decay curves with χ^2 = 149, 11.2, and 2.20 for samples 3, 4, and 6, respectively. Since the corresponding reduced trap concentrations are 0.980, 0.418, and 0.226, these χ^2 reflect on the quality of the two-body approximation to $N_F(t)$. Even for the latter fit (sample 6), the autocorrelation function is poorer than any of the ones shown in Figure 2.5.

The Förster limit expression for the monomer excitation decay fails when monomer-monomer excitation transport becomes important, i.e., when $C_M \gtrsim C_T$. This situation is evidently not reached in any of the samples studied here, as the $N_{eF}(t)$ decay model provides a statistical-limit fit to the emission profiles even for samples prepared from the most dilute coating solutions used (3.2×10^{-6} M). Hence, the Förster limit model satisfactorily accounts for the

monomer excitation trapping decay in all of our cases (except at the highest coverage-sample 1- where instrument function uncertainty becomes important). There is no regime among the samples of Table 2.1. in which the Anderson-Fayer two-body approximation to N(t) provides a uniquely accurate description of the trapping dynamics; such a regime would likely be one in which C_M and C_T are comparable and less than ~ 0.20. For larger reduced surface coverages, higher-order master equation solutions would be required if C_M were not negligible compared to C_T.

Huber has calculated $G^D(t)$ for excitation trapping in three-dimensional disordered systems in which C_T is much lower than C_M [83]. His results correspond approximately to the Loring-Fayer two-body approximation [51] (and somewhat more closely to their three-body approximation) in this regime. Since CV dimers are the overwhelmingly predominant species on quartz at all coverages, the Huber limit does not apply here. Very recently, Loring, Anderson, and Fayer have extended their excitation transport and trapping theory to the case of dilute traps randomly substituted on a regular lattice [29]. Our profiles, emitted by CV monomers on amorphous quartz, are well fit by the continuum model $N_{e2}(t)$ at trap coverages C_T for which $N_2(t)$ is a good approximation to the Förster limit $N_F(t)$. The substituted lattice model may be necessary for dyes adsorbed on single-crystal naphthalene [31].

Conclusions

For the fluorescence profiles emitted by cresyl violet adsorbed onto quartz, our conclusions are as follows:

(i) The bulk of the observed fluorescence from samples 1-6 is emitted by CV monomers whose excitation decays via trapping by dimers in the Förster limit, $C_T >> C_M$. The fast-component emission is unassigned and may be an artifact of the instrument function uncertainty. It is not emitted by impurities but may be CV dimer fluorescence. However, no CV dimer fluorescence is observed in an aqueous CV solution, even though CV dimers absorb strongly at the laser excitation wavelength.

(ii) The autocorrelation functions (Figure 2.5) readily differentiate the qualities of the biexponential and single-exponential plus Förster decay models, although both models yield similar χ^2 in optimized fits. In samples 3-6, the $N_{eF}(t)$ fits yield autocorrelation functions of statistical quality. More flexible model functions (e.g., postulating more than two emitting species) are unnecessary for replicating the decay dynamics.

(iii) The final fluorescence decay parameters for fits based on $N_2(t)$, $N_{eF}(t)$, and $N_e(t)$ [the latter for aqueous CV] correspond to well-defined convergences in the convolute-and-compare analyses. For $N_{ef}(t)$, the extracted C_T and τ_2 values in samples 3-6 (which are less subject to instrument function uncertainty) prove to be physically reasonable (Table 2.4.). Analyses based on the single-exponential plus two-body approximation function $N_{e2}(t)$ will require independent

knowledge of some of the parameters, such as C_M and C_T; these are considerably more difficult to ascertain for dye submonolayers on surfaces than for dyes in solution.

(iv) The long-time emission component originates from CV monomers on quartz, and the Förster term in the single-exponential plus Förster decay model arises from trapping of monomer excitation by CV dimers. The short-time component is unassigned. It is not emitted by CV dimers with structure similar to that found in aqueous solution, although such dimers (cf. Figures 2.2(b) and 2.3) are likely to be the most numerous species on quartz.

Acknowledgments

We thank Professor Duane Smith and Dennis Jensen for their help in the computer analysis of the fluorescence profiles. The Ames Laboratory is operated for the U.S. Department of Energy by Iowa State University under Contract No. W-7405-Eng-82. This work was supported by the Office of Basic Energy Sciences.

CHAPTER III. THE THEORY OF EXCITATION TRANSFER TO DIELECTRIC SURFACES

Introduction

The effect that a metal substrate can have on the excited state lifetime and quantum yield of a luminescing molecule has been the object of scientific interest for approximately the last twenty years. Since the changes in the emission lifetime and quantum yield of molecules located near metals appear to follow some of the same general trends as for molecules adsorbed onto semiconductors, it would be interesting to examine the theoretical and experimental results obtained by the research groups which have worked with metal substrates.

One of the first sets of experiments was performed by Drexhage et al. [84,85] and Drexhage [86,87] who studied the emission behavior of a europium complex in the late 1960s and early 1970s. The emitting molecules were spaced at various distances away from the metal surface by cadmium-arachidate monolayers, which had been deposited on the substrate with the aid of a Langmuir-Blodgett monolayer assembly apparatus. The results of these experiments showed that, for an excited molecule located at distances on the order of or greater than the wavelength of light being emitted by the molecule, the measured lifetime oscillated as a function of distance about a value approximately equal to the natural lifetime of the emitter. When the molecule-to-surface separation distance was much smaller than the

wavelength of emitted light, the excited state lifetime became progressively shorter as the molecule was located nearer and nearer to the surface.

These experimental results stimulated attempts to explain them using classical electromagnetic theory [88-90]. In variations of this theory, the excited molecule was treated as an oscillating point dipole and the metal surface was assumed to be a reflecting boundary. The oscillating dipole is the source of an electric field which is reflected back towards the dipole by the metal surface. This reflected field can interact either constructively or destructively with the dipole. If the reflected field is in phase with the dipole, the radiative rate will increase and the lifetime will decrease. When the reflected field and the dipole are out of phase, the radiative rate decreases and the lifetime increases. The type of interference that the molecule experiences depends on the distance traveled by the reflected field. This explains why at long distances the observed lifetime oscillates around the natural lifetime of the molecule, but it does not explain the behavior seen at the shorter separations. Kuhn [88] was the first to propose that the lifetime reduction at short distances from the surface could be explained by energy transfer from the excited molecule to the substrate. Kuhn's theory gave qualitative agreement with the experimental results, but the quantitative fit to the data obtained for short distances of separation was not very accurate. Chance, Prock, and Silbey, using Kuhn's theory as a starting point, developed their own classical

theory (henceforth called the CPS theory) in a series of papers [91-97] published in the mid-1970s. They showed that this theory gave a better fit to Drexhage's data than Kuhn's theory at all distances. The theory was developed in a general manner allowing it to be applied to substrates other than metals [91]. This aspect opens the possibility of using the theory to explain the behavior of dye molecules adsorbed on semiconductors. For this reason, the CPS theory and some modifications to it will now be examined.

Chance, Prock, and Silbey Theory

As in Kuhn's theory [88], the CPS theory views the emitting molecule as an oscillating point dipole and the metal substrate as a partially absorbing and partially reflecting surface [97]. According to the authors, the system is analogous to a situation described by Sommerfeld, where a radio antenna acting as an oscillating dipole is located near the earth, which behaves as a partially absorbing and partially reflecting surface. The electric field of the antenna can be reflected back, causing constructive and destructive interferences. When examining the excitation decay-rate constant for the emitting molecules, the CPS theory identifies two distinct components. One of these is a radiative component, which is particularly important for large molecule-metal separation distances, and gives rise to the oscillatory behavior of the lifetime. The other component is nonradiative energy transfer due to dipole-dipole

interactions, which cause the reduction in the emission lifetime and become dominant at short distances.

In the CPS theory, the molecule is assumed to be a harmonically bound oscillating dipole which obeys the equation of motion

$$\ddot{\mu} + \omega^2 \mu = \frac{e^2}{m} E_R - b_o \dot{\mu} \tag{3.1}$$

where ω is the frequency of the oscillation of the dipole in the absence of the surface, m is the effective mass of the dipole, E_R is the electric field reflected back from the surface to the dipole, b_o is the excitation decay rate in the absence of the metal, and μ is the dipole moment of the molecule. The oscillation frequencies of the dipole moment and the reflected field are described by the equations

$$\mu = \mu_o \exp[-i(\omega + \Delta\omega)] \exp(-bt/2) \tag{3.2}$$

and

$$E_R = E_o \exp [-i(\omega + \Delta\omega)t] \exp(-bt/2) \tag{3.3}$$

respectively. In these equations $\Delta\omega$ is the frequency shift of the oscillator and b is the decay rate in the presence of a metal surface. By rearranging equations (3.2) and (3.3), these quantities can be expressed as

$$\Delta\omega = \frac{b^2}{8\omega} + \left[\frac{e^2}{2\mu_o m\omega}\right] R_e(E_o) \tag{3.4}$$

and

$$b = b_o + \left[\frac{e^2}{2\mu_o m\omega}\right] \mathrm{Im}\ (E_o) \tag{3.5}$$

where the fact that b^2 and $(e^2/\mu_o m)$ are much smaller than ω^2 has been used. The expression for the radiative decay constant can be written as

$$b_r = \frac{2}{3}\ \frac{e^2 k_1^{\,3}}{m\ \omega n_1} \tag{3.6}$$

where $k_1(=\omega n_1/c)$ is the propagation constant and n_1 is the refractive index of the material in which the dipole is embedded. A normalized decay constant is obtained by dividing by the decay constant b_o in the absence of the metal to give

$$\hat{b} \equiv \frac{b}{b_o} = \frac{1 + 3q\ n_1^{\,2}}{2\mu_o k_1^{\,3}}\ \mathrm{Im}(E_o) \tag{3.7}$$

where $q \equiv b_r/b$ is the quantum yield of the dipole. In order to determine the decay constant all that is necessary is to find the reflected electric field at the position of the dipole.

Figure 3.1 gives a diagram depicting the conditions described by the CPS theory. The coordinates are defined such that the Z axis is perpendicular to the surface of the substrate while the x and y axes are parallel to the surface. Region 1 is the material in which the emitting molecule is embedded and is assumed to be nonabsorbing, having a dielectric constant $\varepsilon_1 = n_1^{\,2}$. The substrate is described as

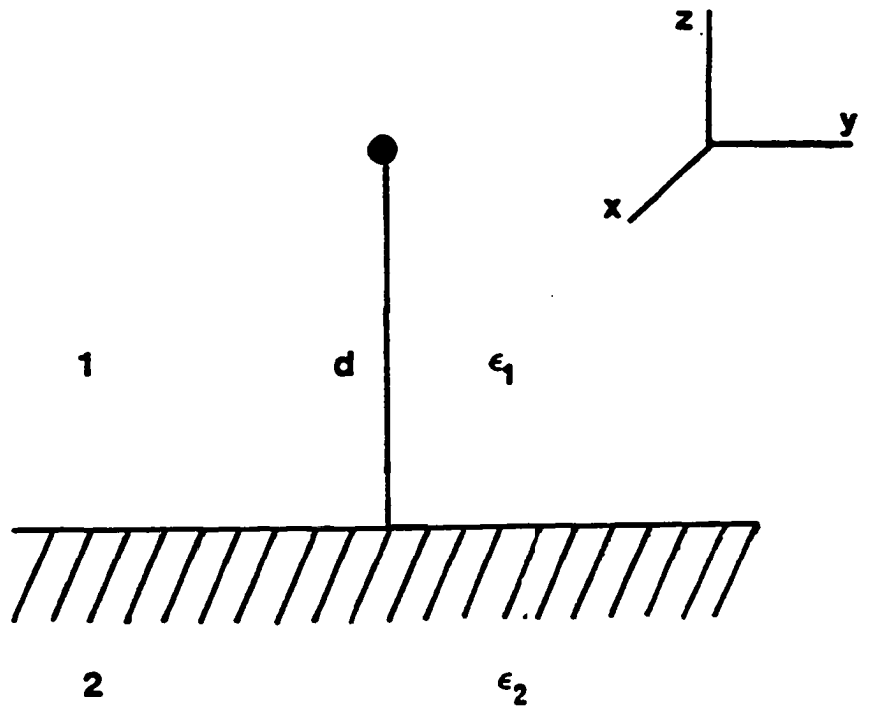

Figure 3.1. Diagram of Model used in CPS theory Region 1 is a nonabsorbing medium having a dielectric constant ε, used to space the emitting molecule a distance d away from the metal surface. Region 2 is a partially absorbing, partially reflecting material with a complex dielectric constant ε_2

region 2, which is partially absorbing and partially reflecting, and there has a complex dielectric constant $\varepsilon_2 = n_2^2 - \kappa_2^2 + 2\, i n_2 \kappa_2$, where n_2 is the real part of the refractive index (sometimes called the dispersion), and κ_2 is the imaginary part of the refractive index and is related to the absorption of the material.

To calculate the electric field, the CPS theory follows the methods of Sommerfeld [98] who made use of the Hertz vectors $\underline{\pi}_1$ and $\underline{\pi}_2$ for regions 1 and 2, respectively. The equations describing these Hertz vectors are

$$\underline{\pi}_1 = e_z \mu k_1 \int_0^\infty du\, J_0(ur) \frac{u}{\ell_1} \left(\exp[\pm \ell_1(z-d)] + \exp(-\ell_1 z)\right) \tag{3.8}$$

and $$\underline{\pi}_2 = e_z \mu k_1 \int_0^\infty f_2 e^{\ell_2 z} J_0(ru) \frac{u}{\ell_1} du \tag{3.9}$$

where $\hat{d} \equiv k_1 d$, $\ell_j \equiv -i\,(\varepsilon_j/\varepsilon_1 - u^2)^{1/2}$, and $J_0(ur)$ is the zeroth-order Bessel function. The electric field of a perpendicular dipole anywhere in region 1 is given by

$$\underline{E} = \frac{1}{\varepsilon_1} \left[k_{1_2} \underline{\pi}_1 + \underline{\nabla} (\underline{\nabla} \cdot \underline{\pi}_1)\right] \tag{3.10}$$

By using the boundary conditions for z=0,

$$\varepsilon_1 \underline{\Pi}_1 = \varepsilon_2 \underline{\Pi}_2 \tag{3.11}$$

and $$\frac{\partial \underline{\pi}_1}{\partial z} = \frac{\partial \underline{\pi}_2}{\partial z} \tag{3.12}$$

the following expressions for the Fresnel coefficients of the electric field are obtained

$$f_1 = -R'' \exp(-\ell_1 \hat{d}) \text{ and } f_2 = \frac{\varepsilon_1}{\varepsilon_2} (1-R'') \exp(-\ell_1 d) \tag{3.13}$$

R" is the reflection coefficient for an incident ray polarized parallel to the plane of incidence and is given by

$$R'' = \frac{\varepsilon_1 \ell_2 - \varepsilon_2 \ell_1}{\varepsilon_1 \ell_2 + \varepsilon_2 \ell_1} \tag{3.14}$$

Therefore, for an emitting dipole oriented perpendicular to the substrate surface, the reflected electric field is given by

$$E_R^{\perp} = \frac{-k_1^3}{\varepsilon_1} \mu \int_0^{\infty} R'' \exp(\ell_1 \hat{d}) \frac{u^3}{\ell_1} du \tag{3.15}$$

which, when used in equation (3.7), gives for the normalized decay rate constant

$$\hat{b}_{\perp} = 1 - \frac{3}{2} q \text{Im} \left(\int_0^{\infty} R'' \exp(-2\ell_1 \hat{d}) \frac{u^3}{\ell_{1-}} du \right) \tag{3.16}$$

If the dipole is oriented parallel to the substrate surface a similar analysis can be used to find the reflected field and the decay rate constant. In this analysis the following equations are used:

$$\underline{\Pi}_1 = e_x \mu k_1 \int_0^\infty \left(\exp[\pm \ell_1 (z-\hat{d})] + f_1 \exp(-\ell_1 z)\right) \frac{u}{\ell_1}\, du\, J_0(ur)$$

$$+ e_z \mu k_1 \frac{x}{r} \int_0^\infty g_1 \exp(-\ell_1 z)\, J_1(ur)\, du \tag{3.17}$$

$$\underline{\Pi}_2 = \hat{e}_x \mu k_1 \int_0^\infty f_2 \exp(\ell_2 z)\, J_0(ur)\, \frac{u}{\ell_1}\, du$$

$$+ e_z \mu k_1 \frac{x}{r} \int_0^\infty g_2 \exp(\ell_2 z)\, J_1(ur)\, du \tag{3.18}$$

$$\frac{\partial \underline{\Pi}_{1z}}{\partial z} - \frac{\partial \underline{\Pi}_{2z}}{\partial z} = \frac{\partial \underline{\Pi}_{2x}}{\partial x} - \frac{\partial \underline{\Pi}_{1x}}{\partial x} \tag{3.19}$$

$$\varepsilon_1 \frac{\partial \underline{\Pi}_{1x}}{\partial z} = \varepsilon_2 \frac{\partial \underline{\Pi}_{2x}}{\partial x} \tag{3.20}$$

$$\varepsilon_1 \underline{\Pi}_{1x} = \varepsilon_2 \underline{\Pi}_{2x}, \quad \varepsilon_1 \underline{\Pi}_{1z} = \varepsilon_2 \underline{\Pi}_{2z} \tag{3.21}$$

$$f_1 = R^{\perp} \exp(-\ell_1 \hat{d}), \quad f_2 = \frac{\varepsilon_1}{\varepsilon_2} (1 + R^{\perp}) \tag{3.22}$$

$$g_1 = (R'' - R^{\perp}) \exp(-\ell_1 \hat{d}), \quad g_2 = \left(\frac{\varepsilon_1}{\varepsilon_2}\right) \exp(-\ell_1 \hat{d}) \tag{3.23}$$

and

$$R^{\perp} = \frac{\ell_1 - \ell_2}{\ell_1 + \ell_2} \tag{3.24}$$

The resultant relationships for the reflected electric field and the decay constant are

$$E_R'' = \frac{k_1^3 \mu}{2\epsilon_1} \int_0^\infty [(1-u^2)R'' + R^\perp] \exp(-2\ell_1 \hat{d}) \frac{udu}{\ell_1} \tag{3.25}$$

and

$$\hat{b}_n = 1 + \frac{3q}{4} \operatorname{Im} \int_0^\infty [(1-u^2)R'' + R^\perp] \exp(-2\ell_1 \hat{d}) \frac{udu}{\ell_1} \tag{3.26}$$

In order to identify the specific contributions to these decay rate constants, the CPS theory calculates the energy flux through a plane above the dipole ($F\uparrow$) and through a plane below the dipole ($F\downarrow$) by integration of the normal component of the complex Poynting vector, $\underline{S}^*$, over the area of the plane of interest

$$F\uparrow,\downarrow = \operatorname{Re} \int_{A\uparrow,\downarrow} \underline{S}^* \cdot \underline{n} \, dA \tag{3.27}$$

where $\underline{S}^* = (\frac{c}{8\pi}) \underline{E} \times \underline{H}^*$ and $\underline{H} = -i (\frac{\omega}{c})$ curl $\underline{\pi}$.

Upon making the appropriate substitutions and evaluating the integrals, the energy flux through a plane above a perpendicular dipole was found to be [97]

$$F\updownarrow = k_1^3 |\mu|^2 \operatorname{Re} \int_0^\infty (\frac{i\omega}{4\epsilon_1}) \frac{u^3}{\ell_1^*} / \exp[-\ell_1(z-d)]$$

$$-R'' \exp[-\ell_1(z+d)]|^2 \, du \tag{3.28}$$

The decay constant associated with this energy flux is

$$b^{\downarrow}_{\uparrow} = \left(\frac{2e^2 k_1^3}{3m\omega n_1^2}\right) \left[1 - \frac{3}{4} \operatorname{Im} \int_0^1 (1-|R''|^2) \frac{u^3 du}{\ell_1}\right.$$

$$\left. - \frac{3}{2} \operatorname{Im} \int_0^1 R'' \exp(-2\ell_1 \hat{d}) \frac{u^3 du}{\ell_1}\right] \tag{3.29}$$

When expresed as a normalized decay rate the equation becomes

$$b^{\downarrow}_{\uparrow} = q - \frac{3}{4} q \operatorname{Im} \int_0^1 (1 - |R''|^2) \frac{u^3 du}{\ell_1}$$

$$- \frac{3}{2} q \operatorname{Im} \int_0^1 R'' \exp(-2\ell_1 \hat{d}) \frac{u^3 du}{\ell_1} \tag{3.30}$$

In a similar way it can be shown that the downward flux gives for the normalized decay rate constant

$$b^{\downarrow}_{\downarrow} = \frac{3}{4} q \operatorname{Im} \int_0^1 (1 - |R''|^2) \frac{u^3 du}{\ell_1}$$

$$- \frac{3}{2} q \operatorname{Im} \int_1^{\infty} R'' \exp(-2\ell_1 \hat{d}) \frac{u^3 du}{\ell_1} \tag{3.31}$$

If the same thing is done for the dipole oriented parallel to the surface, the decay rate constants are written as

$$b^{''}_{\uparrow} = q \frac{-3}{8} q \operatorname{Im} \int_0^1 du \frac{u}{\ell_1} [(1-|R^{\perp}|^2) + (1-u^2)(1 - |R''|^2)]$$

$$\frac{+3}{4}\, q\, I_m \int_0^1 du\, \frac{u}{\ell_1} \exp\,(-2\ell_1 \hat{d})\, [R^{\perp} + (1-u^2)R''] \tag{3.32}$$

and $$b_{\downarrow}'' = \frac{3}{8}\, q\, \mathrm{Im} \int_0^1 du\, \frac{u}{\ell_1}\, [(1-|R^{\perp}|^2) + (1-u^2)(1-|R''|^2)]$$

$$+ \frac{3}{4}\, q\, \mathrm{Im} \int_1^{\infty} du\, \frac{u}{\ell_1}\, [R^{\perp} + (1-u^2)R'']\, \exp\,(-2\ell_1 \hat{d}) \tag{3.33}$$

The first integral in each of the four preceding equations is the term that determines the contribution due to the far field wavevectors, i.e., energy transfer by a radiative mechanism. This component is distance-independent and is dominant at distances far from the surface. The second integral in each equation describes the contribution due to the near field wavevectors, i.e., energy transfer to the substrate via a nonradiative pathway. The nonradiative transfer has a strong distance dependence and becomes very important when the emitter molecule is located close to the surface. CPS [97] derived expressions for the radiative and nonradiative rate constants which for the perpendicular dipole are

$$\hat{b}_r^{\perp} = q - \frac{3}{2}\, q\, \mathrm{Im} \int_0^1 R''\, \exp(-2\ell_1 \hat{d})\, \frac{u^3 du}{\ell_1} \tag{3.34}$$

$$\hat{b}_{nr}^{\perp} = (1-q) - \frac{3}{2}\, q\, \mathrm{Im} \int_1^{\infty} R''\, \exp\,(-2\ell_1 \hat{d})\, \frac{u^3 du}{\ell_1} \tag{3.35}$$

and for the parallel dipole are

$$\hat{b}_r'' = q - \frac{3}{4} q \, \mathrm{Im} \int_0^1 du \, \frac{u}{\ell_1} \left[(1-|R^{\perp}|^2) + (1-u^2)(1-|R''|^2) \right] \qquad (3.36)$$

$$\hat{b}_{nr}'' = (1-q) + \frac{3}{4} q \, \mathrm{Im} \int_1^{\infty} du \, \frac{u}{\ell_1} \left[R^{\perp} + (1-u^2) \, R'' \right] \exp(-2\ell_1 d) \qquad (3.37)$$

The nature of the nonradiative energy transfer has been explained by considering the oscillating dipole as interacting with image dipoles created in the substrate. This interaction should be very similar to the dipole-dipole interactions derived by Förster [36-41] which show the interaction energy to vary as d^{-6}. In this situation, however, the interaction would be between the oscillating point dipole and an entire volume of acceptors. To take this into account, the integration is done over the volume to give the result that the rate will depend inversely on the distance cubed, i.e., $\hat{b}_{ET} = \beta \, d^{-3}$.

According to CPS (97), this rate constant is

$$\hat{b}_{ET} = \frac{-q\theta}{4d^3} \, \mathrm{Im} \, (R''_{d \to o}) = \frac{q\theta}{4d^3} \, \mathrm{Im} \left(\frac{\varepsilon_2 - \varepsilon_1}{\varepsilon_2 + \varepsilon_1} \right) \qquad (3.38)$$

and the energy transfer parameter, β, is given by

$$\beta = \frac{q}{k_1^3} \, \frac{\theta \, n_1^2 \, n_2 \, \kappa_2}{(n_1^2 + n_2^2 - \kappa_2^2)^2 + 4 n_2^2 \, \kappa_2^2} \qquad (3.39)$$

where θ is an orientational parameter that has the values of 3/2 for perpendicular dipoles, 3/4 for parallel dipoles, and 1 for isotropic orientation of the dipoles. For very thin substrates the energy

transfer is assumed to occur into a two-dimensional space which means the integration is done over the surface area so that the transfer rate will be proportional to d^{-4} instead of d^{-3}. CPS theory predicts that this change in the distance dependence should occur when the substrate thickness is about the same as the separation distance from the dipole to the surface. Figure 3.2 is a plot showing the dependence of the energy transfer parameter, β, on the ratio of substrate thickness to distance from the surface to the dipole, $\frac{d_2}{d_1}$, for various values of the substrate's absorption coefficient κ_2. Since $\beta = b_{ET}\, d^3$, the region in the plot where the curves are constant is where the transfer rate varies as d^{-3} and the region where the curves slope downward illustrates the d^{-4} dependence. The peaks shown in the curves for κ_2 larger than n_1 are a result of the thin-film enhancement effect. This indicates that for strong absorbers, large κ_2, a thin substrate may accept energy more efficiently than a thick substrate.

An alternate explanation of the CPS theory is given by Waldeck et al. [99]. The electric field is composed of wavevectors which interact with the substrate to set up a surface charge density oscillation which has its own wavevector components. The reflected field consists of these wavevector components which interfere constructively or destructively with the dipole field causing the lifetime to oscillate around the natural lifetime value. The wavevector components which cause this type of behavior are the far field components. The near field wavevector components also cause

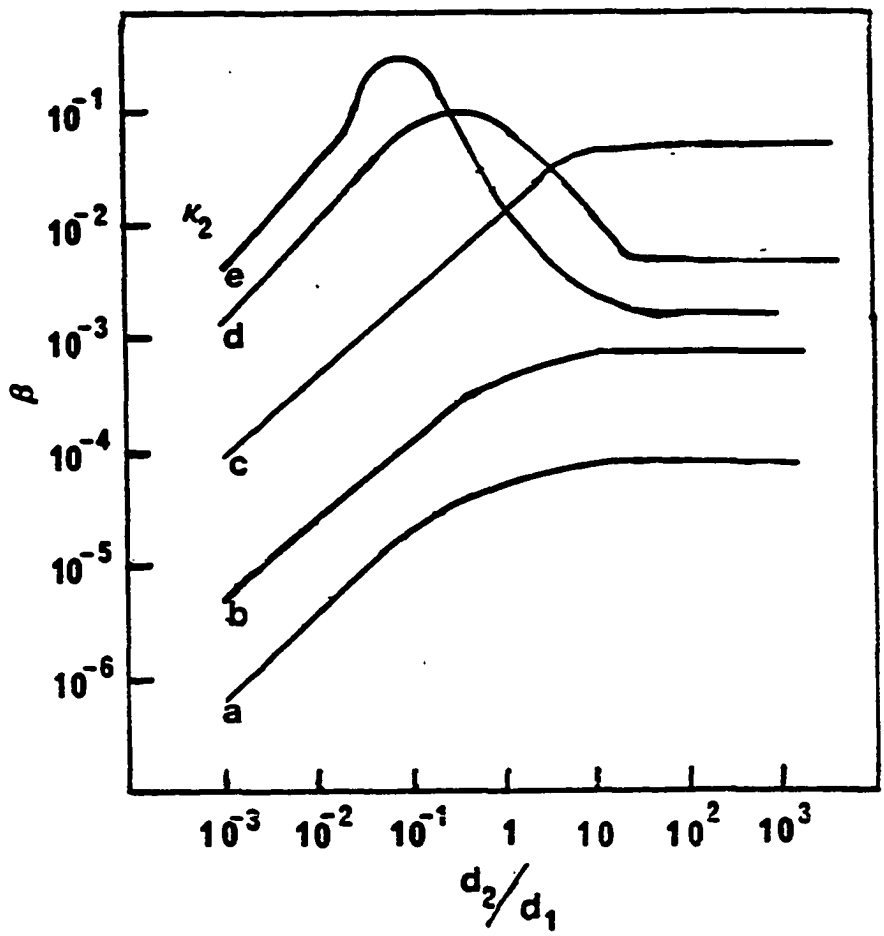

Figure 3.2. Plot of β vs. $\frac{d_2}{d_1}$ for various κ_2 values. The κ_2 values used are a = 0.01, b = 0.1, c = 1, d = 5, e = 10. The plot is for an isotropic orientation of dipoles where $n_1 = n_2 = 1.50$

surface charge density oscillations which act to transfer the energy to acceptor states in the substrate.

The identity of the energy-accepting states in the metal has not been established absolutely. It has been found that under the proper conditions at least some of the energy winds up in the form of surface plasmons [91,100-104]. A surface plasmon is an electromagnetic excitation mode of the conduction electrons which exists at the interface of a dielectric solid [105]. The propagation constant of a surface plasmon is determined by the magnetic permeabilities and the dielectric constants of the substrate as well as the material adsorbed on it [106]. If the wavevector of the surface plasmon is in resonance with the wavevectors from the surface charge density oscillation, then the surface plasmon can act as an effective energy acceptor according to the dispersion relationship.

$$k_{sp} = \left[\frac{\varepsilon_1 \varepsilon_2}{(\varepsilon_1 + \varepsilon_2)}\right]^{1/2} \frac{\omega}{c} \tag{3.40}$$

The energy in the surface plasmon is either dissipated through collisions or by reradiation under the appropriate experimental conditions. According to Weber and Eagen [107], for resonant energy transfer to a surface plasmon the distance dependence is exponential. CPS [97] show that for a metal the energy transfer parameter satisfies the relationship

$$\beta \propto \frac{\omega_p^2 \, \omega\varepsilon_1 \, \sigma}{(1 + \varepsilon_1)^2 \left[\left(\omega^2 - \frac{\omega_p^2}{1 + \varepsilon_1}\right) + \frac{\omega_p^4 \, \delta^2}{\omega^2}\right]} \tag{3.41}$$

where ω_p is the plasma frequency, and δ is the inverse relaxation time. This equation comes from the fact that

$$\varepsilon_2(\omega) = 1 - \frac{\omega_p^2}{\omega(\omega + i\delta)} \tag{3.42}$$

Examination of equation 3.41 shows that β has a resonance with the surface plasmon at $\omega = \omega_{sp} = \omega_p \, (1 + \varepsilon_1)^{-1/2}$.

If the energy being transferred is not in resonance with a surface plasmon, then the energy must be transferred to a nonresonant surface plasmon or to some other type of acceptor mode. The term used by Waldeck et al. [99], Alivisatos et al. [108], Campion et al. [109] and Whitmore et al. [110] for these acceptors is lossy surface waves. These are thought to be electron-hole pair excitations along the surface of the solid. According to momentum conservation, the excited electrons dissipate their energy through scattering with phonons or lattice impurities.

Inherent in the CPS theory are certain assumptions that may not be entirely satisfactory for the whole range of experimental conditions of interest. One of these assumptions is that the excited molecule can be treated as a harmonically bound point dipole

oscillator. This assumption is valid at distances far from the surface, but when the molecular dimensions are on the same order as the separation between the molecule and the surface, the validity of this assumption is in doubt. Another approximation is that the metal is a continuous medium having a uniform complex dielectric constant that is the same for both the surface and the bulk. The boundaries at the interfaces are assumed to be sharp and infinite. This eliminates the possibility of any interactions of molecular wavefunctions which could occur at very close distances. The surface itself is assumed to be perfectly flat so that it can be treated as a two-dimensional plane. In reality, there is a certain amount of surface roughness which could influence the energy transfer. Finally, the material in which the molecule is embedded is assumed to be a nonabsorbing lossless material so that the possibility of this material accepting energy from the emitting molecule can be neglected.

Modifications of the CPS Theory

Partially because of the aforementioned assumptions, several attempts have been made to improve on the CPS theory. In one of these attempts, Ford and Weber [111] examined the consequences of using a nonlocal dielectric constant to describe the substrate. They used a modified Lindhard dielectric constant that was derived from first order perturbation theory. In their analysis, Ford and Weber determined that for molecule-surface separations less than 50Å the distance dependence of the CPS theory is less steep than the results

with their modified dielectric constant. The effects of surface roughness have been considered by Arias et al. [112]. They found that for random roughness components on the order of 20Å, when the molecule-surface separation was less than 50Å, again the lifetime should decrease more rapidly than predicted by CPS theory.

Persson model

As can be seen from the work done by Ford and Weber [111] and Arias and co-workers [112] the region where the CPS theory is expected to have difficulties is when the molecule is located very close to the surface, i.e., at distances less than 50Å. Perhaps the most extensive modifications of the CPS theory for these distances has been performed by Persson [113], Persson et al. [114-116, 118] and Avouris and Persson [117]. The Persson treatment considers the substrate to be a semi-infinite electron gas that is enclosed by an infinite potential barrier as in the CPS theory. Persson also assumes that the metal substrate obeys the jellium approximation, i.e., it consists of a semi-infinite positive background, which results from a smearing out of the positive metal cores, containing the conduction electrons. The emitter molecule is again assumed to behave as an undamped harmonic oscillating point dipole. The primary difference between the CPS theory and the Persson model is that Persson attempted to differentiate the surface behavior from the volume behavior. To do this he made use of Fermi's golden rule to calculate the lifetime of the molecule.

Persson's approach consisted of decomposing the electric field of the oscillating dipole into real and complex wavevectors. The complex wavevectors are the ones that make up the near and far fields of the molecule. The reflection coefficients of these complex wavevectors consist of one term due to the excitation of electron-hole pairs in the substrate surface and another term due to the excitation of plasmons in the substrate bulk. The expected distance behavior of the lifetime should be different for each transfer mechanism. If the energy is transferred into bulk plasmons, where it can be dissipated in the form of heat, then the lifetime should be proportional to d^3 because for a bulk process the entire volume is integrated over when the decay rate constant is determined. If the energy is tranferred to the surface in the form of electron-hole pairs, then the decay constant is found by integrating over the surface area, as in the CPS theory for thin substrates, and the lifetime will vary as d^4.

As previously mentioned, to find the value of the decay rate and lifetime, Persson made use of Fermi's golden rule. The assumption was made that the initially excited molecule loses its energy to an electron in the surface of the substrate. This electron is promoted from an initial level $\underline{k}$ which is below the Fermi level, $\underline{k}_F$, to a level $\underline{k'}$ which is above the Fermi level. According to Fermi's golden rule, the decay rate is given by the equation

$$\frac{1}{\tau} = \frac{2\pi}{\hbar} \int d^3k \; d^3k' \; n_k(1-n'_k) |\langle \underline{k'}, \; n = 0|H'|n = 1\rangle|^2$$

$$x\ \delta(E_{k'} - E_k - h\omega) \qquad (3.43)$$

where $n_k = 1$ if $k<k_f$ and 0 if $k>k_f$, $H' = e\phi(x,t)$, $\phi(x,t)$ is the potential of the dipole when it is near the substrate, n stands for the ground (0) or excited (1) state of the dipole, and $E_k = h^2k^2/2m$. This equation implies that only those electrons having an energy E such that

$$E_F - h\omega<E<E_F$$

can be excited and still maintain the conservation of energy, i.e., in order for an electron to be excited it must be fairly close to the energy of the Fermi level. Since the potential of the dipole quickly disappears the further it penetrates into the substrate, only those electrons close to the surface are going to be able to dissipate the energy through surface collisions fast enough for momentum to be conserved. This is particularly true for cases (e.g., noble metals below the interband transition energy), in which the average time between collisions is sufficiently long that electrons in the bulk cannot satisfy momentum conservation by releasing energy through collisions. Persson reached the conclusion that for distances less than 100Å the excitation of electron-hole pairs along the substrate surface is the dominant mechanism in accepting energy transfer and that excitation of bulk plasmons is relatively unimportant at these

distances. For molecule-surface separations of less than 10Å, the theory has problems because the potential extends farther into the bulk and energy transfer to the bulk might become important. To satisfy the requirements of momentum conservation, Avouris and Persson [117] mentioned three possible sources of collisional scattering. One of these is scattering from phonons or impurities for intraband transitions or from the bulk crystal potential for interband transitions. Another source of momentum conservation is scattering from the surface potential. This is especially important for the excitation of electron-hole pairs along the surface. The final source of momentum conservation is the spatial variation of the near field of the excited molecule which requires a nonlocal dielectric constant.

A comparison of the CPS and Persson theories indicates similarities in the assumptions used but a difference in the types of interactions considered. In both models, the emitting molecule is assumed to be an oscillating point dipole located above a metal surface that has an infinitely sharp potential as a boundary. CPS assumes that this metal has a localized dielectric constant which determines the optical properties of the metal while Persson makes no such assumption. CPS theory allows energy transfer to surface plasmon modes which can decay into the bulk giving a distance dependence of d^3 to the lifetime for short distances. Persson ony looks at separations of less than 100Å and greater than 10Å and considers nonradiative energy transfer into electron-hole pair excitations along the surface having a lifetime variation of d^4 with separation distance. However,

both theories predict that the lifetimes should be fit to a single exponential decay. Finally, neither theory is able to deal effectively with a molecule adsorbed directly on the surface.

Experimental studies of the CPS Theory

Much of the experimental work done involving energy transfer to metal substrates has been summarized in a review article by Waldeck et al. [99]. For the most part, the experiments can be separated into several different categories. One category consists of experiments that tried to examine the energy transfer into surface plasmons. Another category of experiments attempted to measure the total energy transfer rate via the photophysics of the emitting molecule. A third set of experiments to be discussed dealt with energy transfer to semiconductors instead of metal substrates. These experiments are relevant to the applicability of the theories to dye-sensitized semiconductors. Finally, a couple of experiments examine the behavior of molecules directly adsorbed onto metal surfaces.

Measurements of energy transfer to surface plasmons [104, 119-125] has relied primarily on the experimental technique of attenuated total reflection (ATR) to monitor surface plasmon emission as an indication of the amount of coupling into surface plasmon modes. ATR measures the reflected intensity at a fixed wavelength as a function of the angle of incidence [120]. For substrates that are coated with a monolayer of organic dye molecules, the minimum in the reflected intensity is shifted. The amount of the shift and the depth

of the reflected minimum are used to measure the surface plasmon emission. Most of these experiments have been done on systems where the energy released by the emitting molecule was sufficient to excite an interband transition. It is clear that for these systems energy transfer to surface plasmons is an important mechanism. The experiments could not be used to evaluate the relative importance of energy transfer into surface plasmons as compared to energy transfer into other acceptor modes, e.g., electron-hole pair excitations. Certain experiments [104,121] did indicate that surface plasmon emission decreased for distances less than 150Å and vanished when the molecule was almost directly adsorbed on the metal.

A more convenient method of determining the distance dependence of the energy transfer rate is to examine the photophysics of the emitting molecules. The research that has approached the problem from this view point [69,108-110,126-128] has used the luminescence lifetime and quantum yield as the measurables from which information is obtained. These studies indicate that the data seem to be in agreement with the CPS theory at moderate distances (between 50 and 200Å). In this region the lifetime appears to have a d^3 dependence, although at shorter distances, where Persson's d^4 dependence could be of importance, there appear to be deviations from the CPS theory. However, there are not enough data points to favor one model over the other. In particular, some of the recent results from Harris' group for biacetyl molecules near a silver surface [108] show deviations from the d^3 dependence at separation distances less than 85Å that

could be due to excitation of electron-hole pairs, but could also be due to the limitations of the CPS theory that were mentioned earlier. Rossetti and Brus [127,128] also found deviations from the CPS theory when a silver substrate was used but obtained good agreement when the substrate was gold. This indicates that certain substrates might have inherent problems, e.g., formation of oxide layers, that do not affect other substrates. Energy transfer to thin metal films has also been studied with lifetime measurements [129,130]. The substrates were a 10Å thick gold layer [129] and a semi-transparent film of evaporated Al [130]. In both experiments the lifetime showed a d^4 dependence as expected.

To this point in the discussion, all the experiments have used metal substrates. In the development of the CPS theory, it was claimed [97] that the theory was completely general and could be extended to any substrate. So far there have only been a few publications that attempted to examine the distance dependence of energy transfer to other materials. Dexter [131] was among the first to suggest using the classical type model to investigate energy transfer into semiconductors. Two reports that attempted to do this were published at about the same time [132,133]. In one report by Hayashi et al. [132], the distance dependence of energy transfer from thin films of tetracene to Si and GaAs substates, where the emitting molecules were separated from the surface by LiF spacer layers, was examined. Their experimental results showed that for separation distance less than 200Å there was not a d^3 dependence to the lifetime

of the excited state. The tetracene film that was used was polycrystalline in nature and had a thickness close to 50Å. This aggregation and proximity of the tetracene molecules could have led to energy transfer among the molecules themselves which would interfere with the energy transfer to the semi-conductor.

The other study was done by Whitmore et al. [133]. They also used GaAs as a substrate but selected pyrazine as their emitting molecule. The separation distance was varied from a maximum of 430Å down to a minimum of 20Å by varying the thickness of a frozen-ammonia spacer layer. The pyrazine emission at 3.3 eV was sufficiently energetic to overlap with an interband transition in the GaAs. The experimental results appear to agree with the CPS theory at least down to 100Å. For shorter distances the lifetimes are shorter than predicted and barely within the reported experimental error. The authors credit energy transfer to interband electron-hole pair excitations of the semiconductor via the high-wavevector components of the dipole near field with being the dominant decay mechanism.

The last set of experiments to be examined in this section were performed by Avouris and co-workers [134,135] who looked at energy transfer by molecules directly adsorbed on the surface. The authors used high resolution electron energy loss spectroscopy (EELS) to investigate the importance of energy transfer into electron-hole pair surface excitations. The systems studied consisted of aromatic organic molecules (benzene, pyridine, and pyrazine) adsorbed on a silver surface [134] and nitrogen molecules adsorbed on aluminum

[135]. Even though the measurements were taken at only one distance, the authors claim that their results satisfy Persson's model since the lifetime calculated from the data is shorter than that predicted by CPS theory. The amount of useful information from these two experiments is fairly small. With data taken at only one distance, it is difficult to make a conclusion concerning the distance dependence of the lifetime. The lifetime was not a directly measured quantity but had to be extracted from a lineshape analysis of the EELS spectrum. Also, neither theory was predicted to hold for directly adsorbed molecules so some other mechanism might be important.

While the preceding experiments have all provided valuable information regarding energy transfer from an emitting molecule to metal or narrow-band gap semiconductors, several limitations on the relevance of these studies to dye-coated wide-band gap semicoductors need to be mentioned. In some of the experiments, excited state lifetimes were estimated from other quantities such as luminescent intensity, the angular dependence of the emission, or the lineshape variations in EELS spectra. Extraction of lifetimes from these data is subject to experimental limitations. Fluctuations in the intensity of the excitation source can lead to errors in experiments monitoring the luminescence of the molecule or surface plasmons. Because of interference effects from the metal substrate, the angle at which the emission must be detected will vary with the separation distance, which leads to experimental difficulties. Variations in the lineshapes of spectra can be due to other factors than a change in the

excited state lifetimes. More direct measurements of the lifetime should provide more reliable results. As discussed in Chapter II, time-correlated photon counting is an extremely useful method for measuring excited state lifetimes. It is relatively insensitive to fluctuations in the excitation source intensity, it presents no special problems in the emission collection geometry, and the extraction of the lifetime from the experimental data is straightforward.

Even in those experiments where more direct lifetime measurements were made [108-110,127-128,133], the available experimental apparatus dictated that the molecules used have long fluorescence lifetimes or high quantum yields of phosphorescence from the triplet state. This considerably narrowed the choice of emitting molecules and eliminated some molecules having very high fluorescence quantum yields in which competing relaxation processes are at a minimum. An experimental apparatus capable of picosecond time resolution does not have these limitations.

All of the experiments used either metals or narrow band gap semiconductors for substrates. In most of these studies the emission wavelength of the molecule was such that interband transitions in the substrate could be excited. In the dye sensitization experiments mentioned in Chapter I, the substrates of interest are wide-band gap semi-conductors, which absorb toward the ultraviolet region of the

electromagnetic spectrum, and the organic dye molecules used as sensitizers absorb and emit at the lower energies in the visible region.

Except for the experiments of Avouris et al. [134,135] there has been little research done on energy transfer from molecules directly adsorbed on a surface. Neither the CPS theory or the Persson model claim the ability to describe the behavior in this case. However, for most dye-sensitized semiconductors the molecules are directly adsorbed on the semiconductors surface.

The points raised above all indicate that studies of the behavior of energy transfer from organic dye molecules to wide-band gap semiconductors would be beneficial. In this light, the next chapter of this dissertation describes an experiment examining the distance dependence of the fluorescence lifetime of an organic dye molecule, cresyl violet, spaced at various distances from the surface of a wide-bandgap semiconductor, TiO_2, by cadmium-arachidate monolayers. The final section of this chapter gives a description and listing of a computer program used to calculate the distance dependence of the lifetime of an emitting molecule located near a substrate of known dielectric constant based on the CPS theory. The last chapter in this dissertation details studies of the fluorescence lifetime behavior for organic dye molecules directly adsorbed on the surface of wide-bandgap semiconductors.

Program for calculating lifetime distance dependence

This program is used to calculate the normalized decay constant of a molecule with a known emission wavelength imbedded in a nonabsorbing medium at various distances from the substrate, which has a known complex refractive index. Since the decay constant is simply the inverse of the lifetime, once the natural lifetime of the molecule is known it becomes an easy task to generate plots of the fluorescence lifetime versus separation distance from the surface.

The equations which are used in this program come from the CPS theory and are given earlier in the chapter (equations 3.30-3.37). Because the nonradiative and radiative components (equations 3.34-3.37) are derived from the expressions for the decay rates above and below the dipole (equations 3.30-3.33) either set of equations can be used to find the total decay rate. To make the programming easier, the decay rate for a perpendicular dipole is calculated from the equations for the the radiative and nonradiative components while the decay rate for a parallel dipole is calculated from the expressions for the rates above and below the dipole. The integrals cannot be evaluated analytically so a numerical quadrature routine must be used. The algorithm used in this program made use of Simpson's rule for numerical integration. According to Simpson's rule, the area under a curve is found by splitting the curve into small intervals, each of which has an area approximated by the area of a rectangle. The areas of the intervals are then summed to give the total area under the curve.

Certain numerical values are entered as input before the program is executed. These values are: the number of intervals N into which the curve is divided, the distance (D) that a layer of fatty acid molecules spaces the emitting molecule away from the surface, the number (L) of spacer layers, the emission wavelength (Y), the real refractive index (E1) of the medium containing the emitter molecules, and the complex refractive index (E2) of the dielectric substrate. These values are used both to calculate the other variables in the equations and in the equations themselves. The quantities generated by the program are the normalized decay rate constant, (1/B and RINV), the normalized separation distance DHAT which is a function of the emission wavelength, and the number of spacer layers I. Through trial and error it was determined that the minimum number of intervals the curve can be divided into is about 500; therefore this was the value used for N when the program was run. When the results were plotted, the decay rates were changed to lifetime values by inverting and multiplying by a natural lifetime, and the normalized distance was converted to the actual separation distance. The end of this chapter includes the listings of the computer programs for calculating the normalized decay rate constants as a function of the normalized distance (program SIMPS) and for plotting the lifetime versus distance curves (program PLOTIT). Also included are sample plots for silver and TiO_2 substrates, Figures 3.3 and 3.4 (see page 58). Figure 3.3 shows the lifetime distance dependence of a molecule near a silver surface. The parameters used in calculating the curves were the same

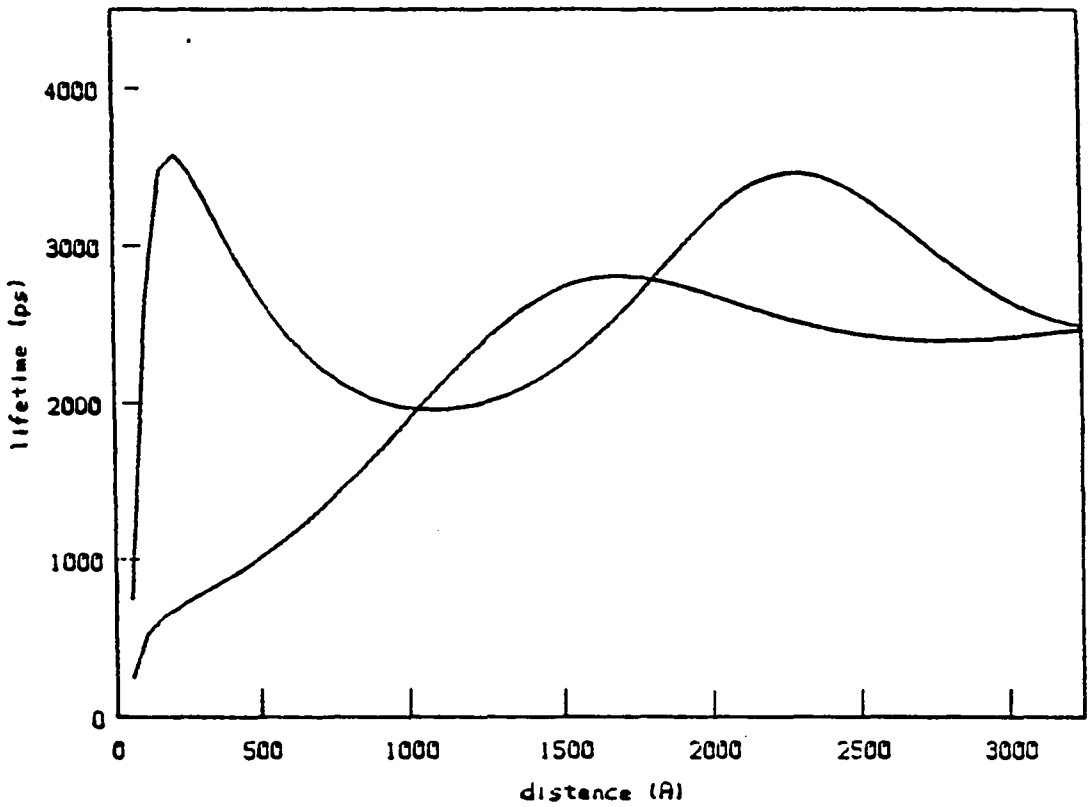

Figure 3.3. Distance dependence of the lifetime of an emitting molecule located near a silver surface. The natural lifetime of the molecule was assumed to be 3000 ps. The optical constants used were: $n_2 = 0.06$, $K_2 = 4.11$ for silver and $n_1 = 1.5$ [97] for the cadmium-arachidate spacer layers. The emission wavelength was taken to be 612 nm [97]. The curve having a maximum at a distance less than 500 Å is for the parallel dipole while the curve with a maximum at about 1500 Å is for the prependicular dipole

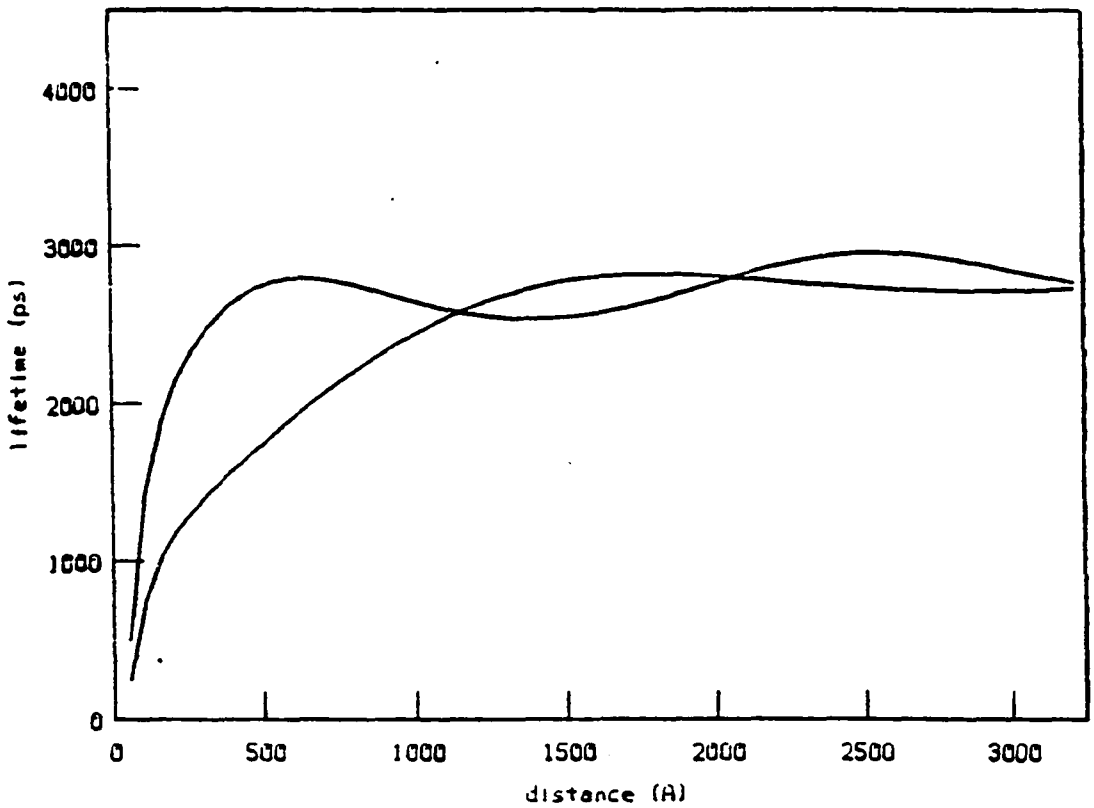

Figure 3.4. Distance dependence of the lifetime of an emitting molecule located near a TiO_2 surface. The natural lifetime was assumed to be 3000 ps. The optical constants used for TiO_2 were: $n_2 = 2.85$ and $K_2 = 0.05$. The emission wavelength was taken to be 630 nm and the cadmium-arachidate spacer layers had a refractive index $n_1 = 1.5$. The curves having a maximum at about 500 Å is for a parallel dipole while the curve with a maximum at about 1500 Å is for the perpendicular dipole

as those used by CPS [97] (n_1 = 1.5, n_2 = 0.06, κ_2 = 4.11, and λ = 612 nm). Figure 3.4 is the same type of plot for a TiO_2 substrate. In this case, the values used for the input parameters were: n_1 = 1.5, n_2 = 2.85, κ_2 = 0.05, and ±30 nm. The emission wavelength are different because the curve for silver was calculated for a europium complex which has a fluorescence maximum at 612 nm while the TiO_2 curves were generated for cresyl violet molecules which have a peak in the fluorescence emission at about 630 nm.

CHAPTER IV. AN EXPERIMENTAL STUDY OF THE DISTANCE DEPENDENCE OF EXCITATION TRANSFER

Introduction

The previous chapter discussed the theory of energy transfer from an emitting molecule to a dielectric substrate. In this chapter, we describe experiments which were designed to examine the energy transfer from an organic dye molecule to a semiconductor substrate. This set of experiments involved measuring the reduction in fluorescence lifetime of cresyl violet, an organic laser dye, located at various distances from the surface of single-crystal TiO_2, a wide-bandgap semiconductor. The results of the experiment are given in the attached publication at the end of the chapter. The details of the sample preparation are presented first.

Sample preparation

The separation between the cresyl violet molecules and the TiO_2 substrate was varied by depositing spacers consisting of monolayers of arachidic acid, a fatty acid, that were formed via interaction with Cd^{2+} ions at the surface of an aqueous solution. This technique has been used by many researchers including Drexhage, Kuhn, and various co-workers [84-87,136-137] who were studying energy transfer from molecules to surfaces and from one type of molecule to other types of molecules separated by these spacer layers. Drexhage [87] and Kuhn et al. [137] have both written review articles that describe the

techniques for preparing the fatty acid monolayers and transferring them to the substrate. Since the pioneering work in the formation of these monolayers was performed by Blodgett and Langmuir [138] these fatty acid layers are frequently referred to as Langmuir-Blodgett monolayers or films. A variety of fatty acids and counter ions can be used to prepare these monolayers, but the most widely used system consists of arachidic acid ($C_{19}H_{39}COOH$) as the fatty acid and cadmium ions (Cd^{2+}) as the cations needed for proper monolayer formation. This system is relatively easy to prepare and has been well characterized [87,137]. The cadmium-arachidate (Cd-C_{20}) monolayer has a thickness of 26.8 Å [87] and is easily transferred to substrates, which makes it a good candidate for use as a spacer layer separating a molecule from a surface.

The nature of the fatty acid molecules makes it possible for them to form monolayers when in contact with water. Each fatty acid molecule is composed of a long hydrocarbon chain with a carboxylic acid functional group at one end. The long hydrocarbon chain is nonpolar and forms the hydrophobic end of the molecule, while the carboxylic acid is polar and therefore is hydrophilic. When placed on the water surface the hydrophilic carboxylic acid group interacts with the water while the hydrophobic hydrocarbon chains interact with each other rather than with the water. Since the acid group will dissociate when in contact with water leaving the carboxylate anion (COO^-), the presence of cations in the water is beneficial to the monolayer formation. Applying a pressure to the fatty acid molecules

results in formation of an organized monolayer [137], with the carboxylate anions located at the water surface and the hydrocarbon chains oriented perpendicular to the surface. Figure 4.1 illustrates this situation.

The procedure used for forming and transferring the monolayers in the cresyl violet TiO_2 experiment is based on information given in Drexhage's review article [87]. The arachidic (also known as eicosanoic) acid was obtained from Aldrich Chemical Co. and had a stated purity of 99.99%. This was dissolved in chloroform to give a solution having 1.5 milligrams of fatty acid per milliliter of solvent. The Cd^{2+} ions were obtained by dissolving $CdCl_2$ (also obtained from Aldrich) in distilled water. The concentration of Cd^{2+} ions in this solution was 5×10^{-4} moles/liter.

To prepare the monolayers, the Cd^{2+}-water solution is poured into a Pyrex tray. Drops of the arachidic acid-chloroform solution are placed on the water surface using a disposable pipette. As the solution is placed on the water surface the drops spread out and the chloroform evaporates leaving a monolayer of arachidic acid. When the number of drops necessary to form a monolayer has been reached, additional drops no longer spread out but remain in the shape of lenses. Reducing the surface pressure by pulling back on the float will allow these drops to also spread out. The float is made of teflon and is used to exert the surface pressure on the fatty acid film resulting in an organized monolayer. According to Kuhn and co-workers [137], for surface pressures between 5 and 60 dynes per

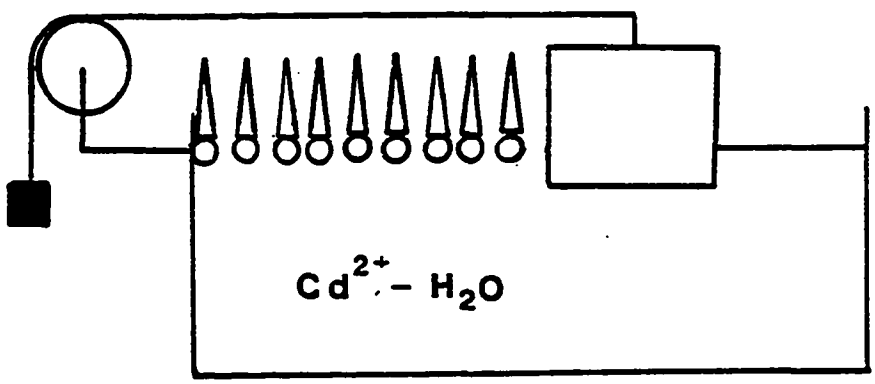

$O=COO^-$

$=C_{19}H_{39}$

Figure 4.1. Formation of Arachidic Acid Monolyers. After the solution containing the arachidic acid molecules is dropped onto the surface, the pressure exerted by the float through the weight and pulley arrangement forces the molecules into an organized monolayer

centimeter the organization of the monolayer remains constant. In this experiment, a surface pressure of approximately 30 dynes per centimeter is achieved by using a weight of one gram for every 30 centimeters of float width [87]. The weight is attached to the float by means of a monofilament line that is stretched (Figure 4.1) horizontal to the water surface before going over a pulley, on the other side of which the weight is suspended.

Once the cadmium-arachidate monolayer has been formed, it can be transferred to a substrate where it serves to space the dye molecules a known distance away from the surface. Transferring the monolayer onto a substrate in accomplished by simply lowering and raising the substrates through the Cd-C_{20} film. Figure 4.2 depicts the way the fatty acid layer is transferred for two different types of substrate. If the surface of the substrate is hydrophilic, when the substrate is lowered through the fatty acid-water interface it will first encounter the long chain hydrocarbon which because of its nonpolar nature is hydrophobic. The hydrophilic surface and the hydrophobic end of the fatty acid do not interact, which results in nothing being transferred to the substrate. As the substrate is drawn up through the fatty-acid water interface, the surface will first come into contact with the polar, hydrophilic, COO^{-}-Cd^{2+} portion of the monolayer. This hydrophilic end becomes attached to the hydrophilic surface resulting in one spacer layer being transferred or deposited on the surface. The next time this substrate is lowered, it will have the hydrophobic ends of the fatty acid molecules projecting out from

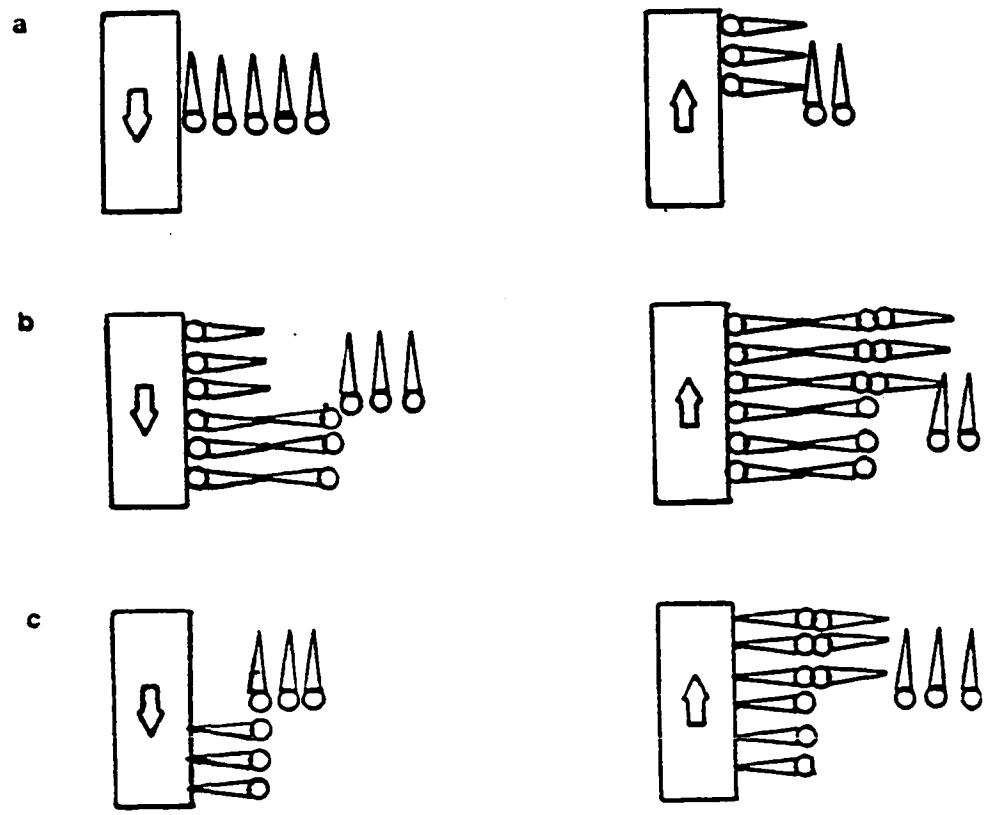

Figure 4.2. Transfer of fatty acid monolayers onto substrates. (a) The first lowering and withdrawal (dip) of a hydrophilic substrate through the fatty acid water interface, (b) is the second dip of the hydrophilic surface, and (c) represents the dipping of a hydrophobic surface

the substrate that will interact with the hydrophobic ends of the fatty acid molecules still at the fatty acid-water interface. This results in another layer being transferred. Upon withdrawal the hydrophilic ends of the transferred molecules will be exposed and interact with the hydrophilic ends of the molecules at the water surface giving a total of three spacer layers that have been deposited. For hydrophilic substrates, an odd number of layers can be deposited by lowering and raising the substrate through the fatty acid monolayer. For hydrophobic substrates on the other hand, an even number of layers are deposited. This is because as the substrate is first lowered, the hydrophobic ends of the fatty acid molecules become attached to the surface. The behavior is otherwise the same as for the hydrophilic substrate. In this experiment the substrates used (fused silica and TiO_2) were hydrophilic, so that after the substrate was dipped, i.e., lowered and then withdrawn through the fatty acid-water interface, an odd number of cadmium-arachidate layers were deposited on the substrate.

A synchronous motor was used to raise and lower the substrates in a controlled and reproducible manner. The motor, through a series of gears and belts, turned a pulley to which was attached a monofilament line having the sample holder affixed at the other end. The rate at which the sample was raised and lowered was set at about 5 cm/sec by choosing the appropriate gears for the synchronous motor.

Initial preparation of the substrates consisted of washes with methanol, dilute aqueous NaOH solution, and distilled water. Later

cleaning of the substrates omitted the NaOH wash unless there was a problem in obtaining good deposition of the cadmium-arachidate layers. This was done because the TiO_2 samples were somewhat soluble in basic solutions and repeated exposure to the NaOH solution could have damaged the surface. To ensure that the substrate was free of dye used in previous experiments, the cleaned substrates were examined with the photon counting apparatus for fluorescence from residual dye molecules. If any was observed, the cleaning procedure was repeated until the fluorescence profiles of the substrate showed no trace of dye fluorescence. After deposition of the arachidic acid layers, the substrates were examined visually for irregularities in the deposited layers. If necessary, the substrates were recleaned and the deposition process repeated.

After the substrate had been cleaned and the fatty acid spacer layers deposited, the dye molecules were adsorbed on top of the outermost cadmium-arachidate layer. This was accomplished by dipping the substrate into a small beaker containing an aqueous solution of cresyl violet having a concentration of approximately 10^{-5} moles/liter. Attempts were made to use ethanol and ethylene glycol solutions to minimize the effects of dimerization of CV in solution, but it was found that these organic solvent dissolved the fatty acid layers and therefore could not be used. The sample was lowered into the dye solution and left for about 1 minute before it was withdrawn. Leaving the sample in contact with the dye solution for longer periods of time did not measurably change the amount of

adsorbed dye as determined from absorption spectra and fluorescence intensities. The samples were lowered into and withdrawn from the CV solution by means of the same apparatus used to transfer the Cd-C_{20} layers onto the substrate. The details of the sample characterization are given in the following publication.

The time-correlated single photon-counting set-up was basically the same as described in Chapter II. The modifications that were made included changing the argon-ion pump laser from Control Laser model 553-A to a Coherent Laser Innova 90 with a 5 watt plasma tube and replacing the Philips XP2020Q photomultiplier with a Hamamatsu R1564U bialkali multichannel plate for detection of the fluorescence photons. The Coherent Innova 90 was implemented since the Control 553-A had to be sent in for a tube replacement; its average output power had dropped below the point where the laser could be used to pump the dye laser. The Philips XP2020Q photomultiplier was replaced because the instrument function width obtainable with the multichannel plate was much narrower than with the XP2020Q, about 120 ps fwhm as compared to about 275 ps fwhm. To prevent the scattered excitation light from reaching the photodetector, two RG610 3 mm Schott filters were placed in front of the collection optics.

The fluorescence decay profiles were deconvoluted and fit with various models. The CPS model and the Persson model both predict that the measured lifetimes should be single exponential, but the latter function gave very poor fits with reduced chi-squares in excess of 20. The bi-exponential function gave better fits, reduced chi-squares

ranging from 2 to 10, with the long-component lifetime increasing with the distance from TiO_2 surface while the short-component lifetime remained relatively constant. Tri-exponential fits were better than bi-exponential, reduced chi-squares between 1.5 and 3, but the middle lifetime fluctuated randomly while the short and long lifetimes behaved the same way as in the bi-exponential fits. Fits to Förster and Förster + exponential models resulted in poor reduced chi-squares and unrealistic lifetimes. The cleaned TiO_2 substrates did exhibit fluorescence having a lifetime approximately the same as that of the short component in the fits, but this does not explain why the bi-exponential model did not fit well. If the dye molecules diffused through the fatty acid spacer layers, a distribution of lifetimes could be possible. James et al. [139,140] have shown that a distribution of lifetimes can be fit satisfactorily with a tri-exponential or even a bi-exponential model. However, in this experiment the difference between the medium and long-component lifetimes is much greater than would be expected if it was due to diffusion of the CV molecules through a few spacer layers. Another possible experimental problem is that CV tends to dimerize on the surface resulting in the possibility of energy transfer between CV monomers and dimers as well as between CV monomers and the TiO_2 surface. Similar experiments were performed with Rhodamine B (Rh B) molecules, which absorption spectra indicate exist in predominantly the monomer form, and the same type of results were found. Therefore, the most realistic comparison to the theories mentioned in Chapter III

should involve the long-component lifetime from the bi-exponential model. As the Persson model is expected to apply at separation distances less than 50 Å and the distances involved in this experiment were between 80.4 Å and 509.2 Å the comparison is done solely between the experimental results and the Silbey theory.

Nonradiative excitation decay of cresyl violet on TiO_2: Variation with dye-surface separation

Dye-to-surface nonradiative excitation transfer is verified to be an important decay mode for S_1 state cresyl violet separated from a TiO_2 surface by distance between 80 and 509 Å. Fluorescence profiles have also been obtained for cresyl violet adsorbed directly onto TiO_2.

Introduction

Dye sensitization of ultraviolet-bandgap semiconductors has been extensively researched as a means for extending their photocurrent response in liquid-junction cells to the visible spectrum. Low photocurrent yields ($\lesssim 10^{-2}$) are typical for dye monomers on single-crystal semiconductors [141], and the origin of this inefficiency has been a subject of inquiry. It has long been appreciated [8] that excited states of dyes on metals decay rapidly and nonradiatively by a dipole mechanism, exciting surface plasmons in the substrate. Analogous

processes on semiconductors have received little attention as a decay pathway which can bypass electron injection into the semiconductor.

During the 1970s, Chance et al. [92,97] developed a classical electromagnetic theory for radiative and nonradiative decay of an excited molecule which fluoresces with wavelength λ in the presence of an arbitrary dielectric surface with structural properties phenomenologically embodied in a complex refractive index $\tilde{n}_2 = n_2 + i\kappa_2$. In the limit of small dye-surface separations $d \lesssim 0.1\lambda/2\pi n_1$, the presence of the surface is predicted to enhance the nonradiative decay rate by a factor

$$b = \frac{3q\lambda^3\theta}{32\pi^3 n_1} \frac{n_2\kappa_2 d^{-3}}{(n_1^2 + n_2^2 - \kappa_2^2)^2 + 4n_2^2\kappa_2^2}, \qquad (4.1)$$

where n_1 is the refractive index of the medium above the surface, q is the isolated-molecule fluorescence quantum yield, and $\theta = 1(2)$ for transition moments parallel (normal) to the surface. Whitmore et al. have already shown that this limiting d dependence is observed for phosphorescing pyrazine on GaAs [133]. Drexhage and co-workers previously obtained detailed lifetime data for a Eu^{3+} complex on metals like Ag and Cu with d behavior which is well simulated by the Silbey theory [142,143]. To date, the fact the equation (4.1) predicts rapid nonradiative decay rates for a dye separated by small d from semiconductors (e.g., ZnO, TiO_2) has not been emphasized. For cresyl violet (CV) on a wide-bandgap semiconductor with $\kappa_2 \approx 5 \times 10^{-4}$ at visible λ, a nonradiative decay rate $>2 \times 10^{10}$ s^{-1} is predicted for

d<5 Å - so this decay mode may account in part for the low photocurrent efficiencies.

We have evaluated fluorescence profiles for CV separated from an undoped rutile TiO_2 surface, cut normal to the c-axis, by odd numbers between 3 and 19 of eicosanoic acid spacer layers 26.8 Å thick. The CV long-component fluorescence decay times are compared with the Silbey theory for d between 80.4 and 509.2 Å, with results that argue strongly that dye-surface energy transfer is the major nonradiative decay mode at these separations. We have also obtained fluorescence profiles for CV adsorbed directly onto TiO_2, in order to measure the nonradiative decay rate at small distances.

Experimental

The laser system, optics, and time-correlated photon-counting system have been described previously [144]. The Philips XP2020Q photon counting tube was replaced with a Hamamatsu R1564U bialkali multichannel plate photodetector, giving a combined instrument function width of ≈ 120 ps fwhm. Fluorescence profiles were analyzed as before with a Marquardt nonlinear regression convolute-and-compare algorithm.

Cresyl violet obtained as laser dye from Exciton was used without further purification [144]. Rutile crystals (nominally λ/10 surfaces with 40/20 scratching) were purchased from Commercial Crystal Laboratories (South Amboy, NJ). Arachidic (eicosanoic) acid layers were deposited onto the TiO_2 surfaces using the Langmuir-Blodgett

technique as described by Drexhage et al. [142,143], whereby a monolayer of cadmium arachidate was formed on the surface of a 5×10^{-4} M $CdCl_2$ aqueous solution. The hydrophilic TiO_2 substrate (precleaned in CH_3OH, dilute NaOH, and distilled water and dried) was lowered through and raised from the monolayered solution surface N time at ≈ 5 cm/s, yielding 2N - 1 arachidic acid layers 26.8 Å thick [87] on the TiO_2 surface. CV was subsequently adsorbed onto the top layer by equilibration for ≈ 1 min with a 10^{-5} M aqueous CV solution; longer equilibration times did not increase the dye coverage as measured by optical density or fluorescence count rates. The reproducibility of the arachidic acid/CV coating procedure was tested by measuring 530 nm optical densities (at the $S_1 \leftarrow S_0$ band maximum of adsorbed CV [144]) of TiO_2 substrates which had repeatedly been alternately coated with two arachidic acid monolayers and one CV submonolayer. For samples thus prepared with 7, 11, 15, and 19 arachidic acid layers, the uncorrected optical densities (measured on a Perkin-Elmer 320 spectrophotometer) were 0.0022, 0.0066, 0.0112, and 0.015555 - meaning that the average adsorbed CV submonolayer optical density was 0.0022 to within 0.0001 for each increment. The CV surface density in each submonolayer was ≈ 1.3×10^{13} cm^{-2}. As in the case of CV on quartz [144], the number density of CV dimers was appreciable, and the bulk of detected fluorescence was emitted by CV monomers. This fact complicates the fluorescence profiles, because

the fluorescence dynamics are then influenced by dimer trapping of electronic excitation as well as by intramolecular and dye-surface nonradiative decay.

Results

Deconvoluted fluorescence profiles from CV on arachidic acid-layered TiO_2 should exhibit single-exponential decay if intramolecular and dye-surface nonradiative decay dominate the S_1 state dynamics. Convolute-and-compare analyses based on this decay law gave poor fits (reduced χ^2>20). Better convergences were obtained with biexponential fits (reduced $\chi^2 \approx 2$-10), for which we give optimized preexponential and lifetime parameters for several d in Table 4.1. An adsorbed impurity on the uncoated TiO_2 substrates luminesced with a lifetime on the order of 50 ps, which partially explains the necessity of using a biexponential model to obtain low χ^2. Excitation trapping by CV dimers is also appreciable at the present dye coverages [144]; in the Förster limit of high dimer coverage, the CV fluorescence intensity in a two-dimensional disordered system is [30,144]

$$I(t) = I_0 \exp[-t/\tau - 1.345 C_T (t/\tau)^{1/3}] \quad , \tag{4.2}$$

where C_T is a reduced trap coverage defined in ref. [144]. For $t \gg \tau$(τ^{-1} is the sum of the rate constants for radiative, intramolecular nonradiative, and dye-surface nonradiative decay) the decay law in eq. (4.2) is essentially single-exponential. Accordingly, the long-

Table 4.1. Fitting parameters for CV fluorescence profiles using $I(t) = A_1\exp(-t/\tau_1) + A_2\exp(-t/\tau_2)$

Number of arachidic acid spacers	τ_1(ps)	A_1	τ_2(ps)	A_2	x^2
3	72	0.088	946	0.020	7.31
5	78	0.081	1035	0.020	9.63
7	54	0.195	1267	0.038	3.06
9	50	0.241	1281	0.023	3.06
19	53	0.137	2012	0.065	7.44

component lifetime τ_2 in a biexponential fit will approximate τ, which contains information about the d-dependent nonradiative decay rate. Lower χ^2 can be exacted using triexponential or higher-exponential fits (reduced $\chi^2 \approx 1.5 - 3$ were obtained in the former case), but the greater model function flexibility tends to improve the fitting of short-to-medium time data at the expense of the long-time component. We plot the biexponential long-component lifetimes τ_2 in Figure 4.3 versus the dye-surface separation d. The curves in Figure 4.3 are computed from the classical electromagnetic theory [92,97]. Since our d regime extends considerably beyond that in which the asymptotic from of equation (4.1) is accurate, the theoretical enhancement factors for the total decay rate due to the presence of the surface must be evaluated numerically from [97]

$$\hat{b}(\perp) = 1 - \frac{3}{2}\mathrm{Im}\int_0^\infty R'' \exp(-2l_1\hat{d})u^3 du/l_1 \qquad (4.3)$$

and

$$\hat{b}(\parallel) = 1 + \frac{3}{4}\mathrm{Im}\int_0^\infty [R^\perp + (1-u^2)R'']u \exp(-2l_1\hat{d})du/l_1 \qquad (4.4)$$

for CV transition moments normal and parallel to the surface, respectively. The parameters in Equations (4.3) and (4.4) are defined [97] as

$$l_i = -i(\varepsilon_i/\varepsilon_1 - u^2)^{1/2}, \quad \hat{d} = 2\pi n_1 d/\lambda,$$

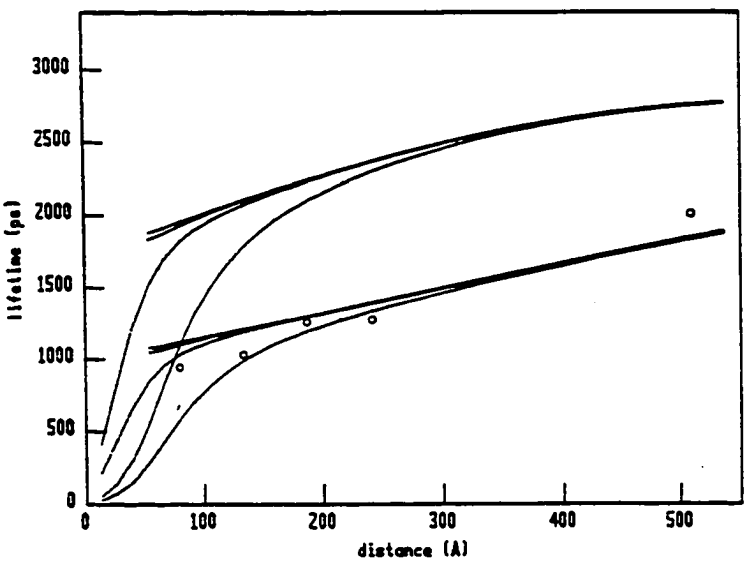

Figure 4.3. Comparison of theoretical lifetimes $\tau_{\parallel}$ (upper group of curves) and $\tau_{\perp}$ (lower group of curves), calculated for CV separated from TiO_2 surface by arachidic acid layers, with experimental long-component lifetimes (data points) from Table 4.1. The intromolecular lifetime τ_0 is taken to be 3000 ps in calculating the theoretical curves (see text). Within each group of curves, n_2 is constant (=2.66), and κ_2 is set equal to 4×10^{-6}, 4×10^{-3}, and 4×10^{-2} in descending order

$$R'' = (\varepsilon_1 I_2 - \varepsilon_2 I_1)/(\varepsilon_1 I_2 + \varepsilon_2 I_1),$$

$$R^{\perp} = (I_1 - I_2)/(I_1 + I_2),$$

with $\varepsilon_1 = n_1^2$ and $\varepsilon_2 = n_2^2 - \kappa_2^2 + 2in_2\kappa_2$. The integrals for $\hat{b}(\perp)$ and $\hat{b}(\parallel)$ were evaluated by Simpson's rule with $n_1 = 1.5$ for arachidic acid spacers [142,143]. TiO_2 is optically anisotropic [145], and for the present theory we used $n_2 = \frac{1}{3}[n_2(E \parallel c) + 2n_2(E \perp c)] = 2.66$ at 630 nm. Plots of n_2 and Im $\varepsilon_2 = 2n_2\kappa_2$ from absorption and reflectivity measurements [145] may be used in principle to estimate κ_2. However, κ_2 is so small at 630 nm that it has not been measured accurately to our knowledge. Typical κ_2 for semiconductors at energies far below bandgap are $<5 \times 10^{-4}$ ($\alpha<10^2$ cm^{-1}). The theoretical d-dependent lifetimes $\tau_{\perp}$ and $\tau_{\parallel}$ in Figure 4.3 were therefore computed for $n_2 = 2.66$ and $K_2 = 4 \times 10^{-2}$, 4×10^{-3}, 4×10^{-4}, and 4×10^{-6}; they are related to the intramolecular lifetime τ_0 by $\tau_{\perp}/b(\perp)$ and $\tau_{\parallel} = \tau_0/b(\parallel)$. For physically reasonable $\kappa_2 < 4 \times 10^{-3}$, K_2 has little effect on computed lifetimes for $d \gtrsim 80$ Å; the scaling factor τ_0 may thus be adjusted to bring the $\tau_{\perp}$ curves for $\kappa_2 < 4 \times 10^{-3}$ into approximate agreement with the data points. The value $\tau_0 = 3000$ ps used in Figure 4.3 is commensurate with isotropic CV lifetimes in ethanol (3510 ps), propanol (3870 ps), and water (2390 ps) [80]. Alternatively, the points may be approximated by $\tau_{\parallel}$ by setting $\tau_0 \approx$ 2000 ps. Since τ_0 in CV is sensitive to the environment, more data

are required to establish the orientation of the CV transition moment with respect to the surface.

Fluorescence profiles from CV adsorbed directly onto TiO_2 by a solution coating technique [144] exhibited much more rapid decay, strongly dominated by short components with lifetimes < 300 ps. A typical triexponential fit for CV on TiO_2 gave lifetimes of 36.8, 209, and 1555 ps with preexponential factors 0.097, 0.023, and 0.004 (χ^2 = 1.34). This decay was also much more rapid than was observed on quartz at similar coverage [144]. According to Equation (4.1), a superimposition of single-exponential decays is to be expected for dye adsorbed over a distribution of small d-values (e.g., on a rough surface, or with monolayers of air or solvent interspersed between dye and TiO_2). Equation (4.1) predicts $\tau_\perp$ = 38 ps and 614 ps for d = 2 and 5 Å, respectively when τ_0 = 3000 ps and $\kappa_2 = 2 \times 10^{-5}$, a physically reasonable order of magnitude for κ_2. Since κ_2 (which is so small at 630 nm that it is easily influenced by impurities) is not known accurately, this work does not prove that dye-surface non-radiative decay controls CV excited state decay near the surface. Figure 4.3 does show that this decay mode is important between 80 and 509 Å, but more controlled experiments are needed to be sure of the dominant CV decay mechanism at small separations.

Control experiments were done with fused quartz replacing the TiO_2 substrate. On quartz, the long-compared lifetime varied by less than 10% (≈ 2200-2400 ps) in this separation range, and hence (unlike on TiO_2) dye-surface energy transfer is not important. This is

consistent with the fact [144] that intramolecular decay plus excitation trapping account for nearly all of the features of fluorescence profiles on quartz. Calculations of $\tau_{\parallel}$ and $\tau_{\perp}$ using $\kappa_2 = 4 \times 10^{-5}$ (an upper limit to the actual value in quartz) and $n_2 = 1.55$ (the approximate refractive index of quartz) yield a constant lifetime down to d<25 Å. This arises physically from the near-match between the refractive indices of the spacers ($n_1 = 1.5$) and quartz, which greatly reduces the optical discontinuity at the interface.

An alternative decay mode whose rate would vary with dye-surface separation is electron tunnelling from excited dye into the TiO_2 conduction band. The sensitivity of tunnelling lifetimes to barrier width would show little resemblance to that in Figure 4.3. For 4.8 eV square barriers with 2.2 and 2.6 Å widths, the quantum mechanical electron tunnelling lifetimes would be ≈90 and ≈700 ps respectively.

The identity of the surface's energy-accepting mode is not addressed by the classical electromagnetic theory, since the empirical resonances in $\tilde{n}_2$ can arise physically from surface plasmons in metals [92], surface polaritons [146], or interband electronic transitions in semiconductors. The latter mechanism appears to govern $^3n,\pi^*$ pyrazine nonradiative decay on GaAs [133], for which bandgap energy is smaller than the electronic excitation energy in pyrazine. The reverse is true for S_1 CV on TiO_2 (rutile), and the question of the mechanism for the non-radiative energy transfer in this system remains open. Experiments are planned for resolving this, and for studying the small-d behavior of the nonradiative decay.

CHAPTER V. EXCITATION TRANSFER FROM A DIRECTLY ADSORBED DYE TO A SURFACE

Introduction

The previous chapters have examined energy transfer among molecules adsorbed on a fused quartz substrate, and from molecules to a semiconductor surface from which they are separated by fatty acid spacer layers. For dye-sensitized semi-conductors, the most interesting situation is energy transfer from dye molecules adsorbed directly onto the semiconductor. Neither of the theories developed to explain the lifetime shortening of molecules located near a dielectric surface, i.e., the CPS and Persson theories discussed in Chapter III, has been applied to this situation. In fact, Persson and Persson [114] states that his theory would not give an adequate description of the energy transfer that would occur. It is important, however, that the fluorescence lifetime behavior of emitting molecules directly adsorbed onto the surface of a dielectric substrate be examined and that an attempt be made to correlate this behavior with a model to describe the energy transfer. In this chapter experiments are described in which the fluorescence decay profiles of Rhodamine 3B molecules adsorbed onto fused quartz, TiO_2, and ZnO substrates were collected via single photon counting. These decay profiles were then analyzed with various models in an effort to find a realistic explanation of the energy transfer mechanism.

Experimental conditions

Several changes were made in the single-photon counting set-up to improve the time resolution of the experiments. As in the experiments described in Chapter IV, the photomultiplier tube was a Hamamatsu 1554U microchannel plate phototube (MCP) that had a bialkali photocathode and borosilicate glass window. The photocurrent output pulses from the MCP were amplified and inverted by means of a B&H MIC (3.15 GHz) 21 dB preamplifier and an EG&G IT100 inverting transformer. The Ortec 583 constant-fraction discriminator that had been used in previous experiments was replaced by a Tennelec TC 455 quad constant-fraction discriminator which resulted in an overall instrument response function of about 80 ps fwhm as compared to 125 ps fwhm yielded by the prior arrangement. The STOP pulses were obtained by routing a fraction of the pulses from the dye laser to an EG&G FOD-100 photodiode, with the photodiode output being sent through an Ortec 934 quad constant-fraction discriminator.

The primary modification to the laser system was the implementation of a cavity dumper. The purpose of the cavity dumper was to reduce the repetition rate of the laser pulses coming from the dye laser. The components of the cavity dumper were: a Harris Corp. H-102 driver, a Harris Corp. H-100 AOM crystal, and several Line Tool Company translation stages. By using the cavity dumper, it was possible to slow down the repetition rate of output pulses from the dye laser from 48 MHz to 4.8 MHz. This made it easier to accurately follow the fluorescence decay at longer times. When the repetition

rate was 48 MHz, fluorescence due to succeeding laser pulses could reach the MCP before the fluorescence decay profile was complete. A background correction term was used in the deconvolution program to account for this artifact. However, this background correction increased the number of adjustable parameters in the fitting routine which could have affected the results of the fitting procedure. With the cavity dumper this correction is no longer necessary and the data analysis is more straightforward.

In order to continuously monitor the laser output, a portion of the laser pulses was fractioned off with a beam splitter and sent through a real-time rotating-mirror zero-background autocorrelator based upon the design of Yasa and Amer [147]. By examining the autocorrelation traces on an oscilloscope, it was possible to determine if the laser performance had degraded during the time needed for data collection. Optimization of the laser output was also much easier to accomplish with the use of the real-time autocorrelator.

In these experiments, Rhodamine 3B (Rh 3B) was chosen as the emitting molecule because it offered several advantages over other available organic dye molecules. First, Rh 3B is a laser dye with a high fluorescence quantum yield, which indicates that competing intramolecular radiationless decay processes are minimized. Also absorption studies indicate that Rh 3B adsorbs on a surface in predominantly the monomer form which is vastly different than the oxazine dyes (including cresyl violet) that had been found to adsorb in mainly the dimeric form. Since Rh 3B is an esterfied version of

Rhodamine B (Rh B) it does not exhibit the complications due to acid-base equilibria that were observed in Rh B [79]. With an $S_1 \leftarrow S_0$ absorption band characterized by $\varepsilon_{max} \approx 1.2 \times 10^5$, at 555 nm in ethanol solution and at about 565 nm when adsorbed on a surface, the spectral overlap with the 575 nm dye laser is sufficient for collecting the fluorescence decay profiles even at the lowest dye coverages. The dye was purchased in the form of Rhodamine 3B perchlorate from Eastman Kodak Laser Products. No further purification was performed since thin layer chromatography experiments of Rh 3B showed only one spot on Analtech Silica Gel G plates for ethanol/acetone, ethanol/acetic acid, and n-propanol/formic acid solvent mixtures.

The substrates used in the experiments were fused quartz (an insulator), TiO_2, and ZnO (both wide-band gap semiconductors). Each substrate was cut into smaller pieces (approximate dimensions: 1 cm wide, 1 cm long, and 1-2 mm thick) so that several samples could be prepared for each substrate. One of the two ZnO substrates prepared in this manner was broken so all of the ZnO samples were prepared from the same piece of ZnO. TiO_2 and ZnO were both obtained as undoped single crystals with surfaces cut normal to their c-axes and optically polished. TiO_2 was purchased from Commerical Crystal Laboratories (South Amboy, NJ) while ZnO was purchased from Airtron (Morris Plains, NJ). The fused quartz had been polished to a $\lambda/4$ optical quality. Before preparing samples, all of the substrates were cleaned with distilled water and methanol rinses to remove any residual dye that

might have remained from previous experiments. After cleaning each substrate and before coating it with the dye solution, it was examined for any fluorescence from residual dye molecules. If such fluorescence was found, the substrate was recleaned until it was found to be free of this residual dye fluorescence. Both the TiO_2 and ZnO substrates exhibited fluorescence even after thorough cleanings. This fluorescence was possibly due to broadening of the bandgap absorption bands at room temperature so that there was a small overlap with the 575 nm laser line. The TiO_2 fluorescence was short-lived, with a lifetime on the same order as the width of the instrument function, which tended to distort the fluorescence decay profiles and complicate the data analysis. The fluorescence from the ZnO substrate was much longer-lived, with a lifetime greater than 3 ns. This did not noticeably affect the fluorescence decay profiles, meaning that the data analysis could be readily accomplished. In both cases, the substrate fluorescence was less than 5% of the fluorescence from the dye-coated samples.

The procedure for adsorbing Rh 3B onto the substrates consisted of dipping the substrates into aqueous solutions of Rh 3B and allowing them to remain in the solution for about 5 minutes, to establish an equilibrium between the dye molecules in solution and on the surface, before withdrawal. As shown by other members of this research group [148] the solution concentrations required to achieve surface dye coverages that have little energy transfer between Rh 3B molecules are very low. In these experiments, the Rh 3B solution concentration was

approximately 7 x 10^{-9} M. The uniformity of the dye coverage on the sample was monitored by measuring the total fluorescence count rate as the sample was translated by means of a computer-controlled stepper motor. These surface scans also made it possible to avoid collecting fluorescence from an area with a high fluorescence count rate relative to the rest of the sample (i.e., a concentrated hot spot).

While the fluorescence decay profiles were being collected, the laser scatter was blocked from reaching the MCP by a set of 3 mm Schott glass filters that consisted of a pair of OG590 filters and a single RG610 filter. The decay profiles were transferred to the MINC-23 computer system where, as in the previous experiments, they were deconvoluted with various fitting models by means of a Marquardt nonlinear regression program. The results from these fits were then examined in terms of how well the model fit the data and the values obtained from the model to make some conclusions about the energy transfer from Rh 3B to the substrates.

Fits to exponential models

Some of the models used in the data analysis were based upon linear combinations of exponential lifetimes. The simplest model of this type is the single exponential model,

$$N(t) = A \exp(-t/\tau)$$

The quality of fits to this model was poor for all of the samples with reduced chi-square values greater than 10 for the TiO_2 and ZnO samples and greater than 2 for all of the fused quartz samples. The fits to a bi-exponential model, were much improved compared to the

$$N(t) = A_1 \exp(-t/\tau_1) + A_2 \exp(-t/\tau_2),$$

single exponential model. Table 5.1 gives examples of the parameters obtained from typical bi-exponential fits to data obtained from samples of the various substrates. Figures 5.1, 5.2, and 5.3 are plots of the experimental data (the dots) and the bi-exponential fit (the solid line) to that data. In the upper right hand corner of each plot is the autocorrelation of the residuals. As can be seen from the information in the table and the plots, the bi-exponential model gives a good fit to the data for Rh 3B on fused quartz with a reduced chi-square close to 1 and a nearly statistical autocorrelation of residuals. On the other hand, the bi-exponential model fits to the decay profiles from TiO_2 and ZnO samples are not quite as good. The reduced chi-squares while being much smaller than in the single exponential case are still larger than is acceptable for a good fit. Also, the autocorrelations of residuals (which are more sensitive indicators of the quality of the fit) are not statistical.

When the number of exponentials in the model was increased to three,

$$N(t) = A_1 \exp(-t/\tau_1) + A_2 \exp(-t/\tau_2) + A_3 \exp(-t/\tau_3),$$

Table 5.1. Bi-exponetial fitting parameters

Substrate	A_1	$\tau_{1,ps}$	A_2	$\tau_{2,ps}$	x^2
Fused quartz	0.045	3841	0.014	1196	1.076
TiO_2	0.025	689	0.121	173	1.835
ZnO	0.008	1200	0.021	252	1.607

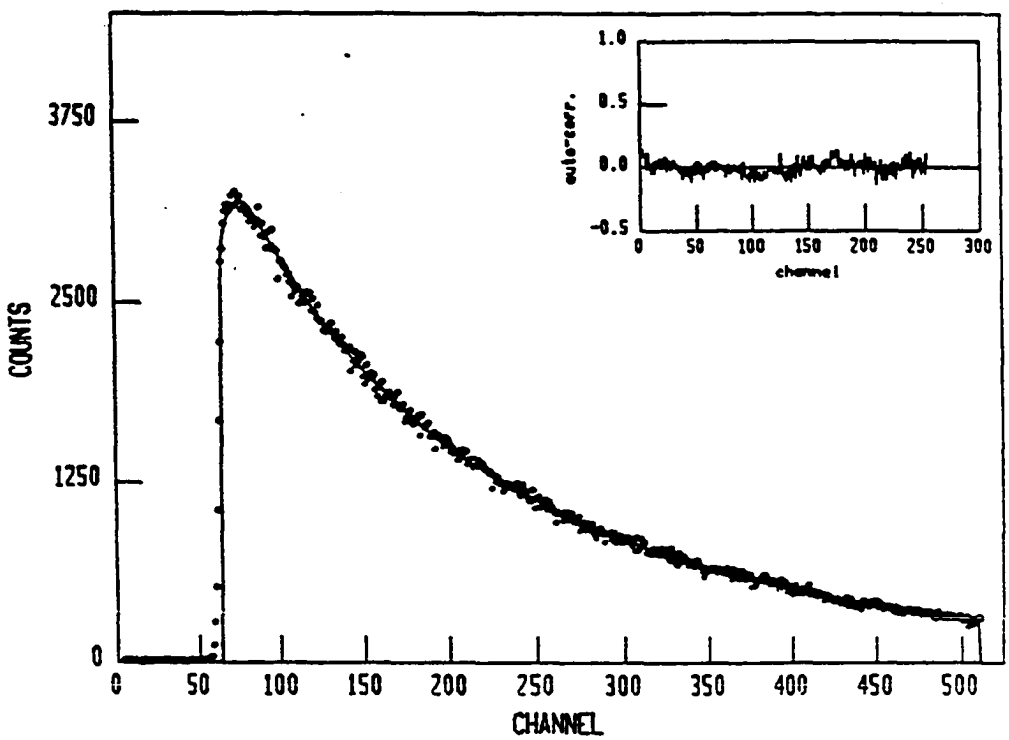

Figure 5.1. Bi-exponential fit to the data obtained from a sample having Rh 3B adsorbed on fused quartz. The lifetimes, pre-exponents, and reduced chi-square are given in Table 5.1

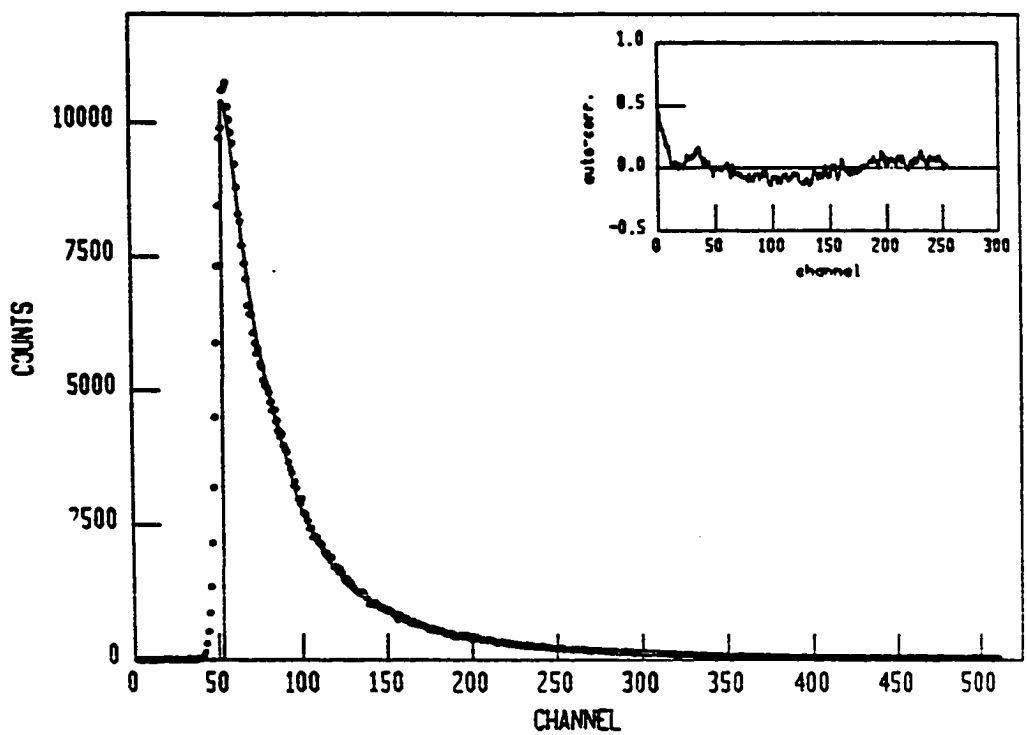

Figure 5.2. Bi-exponential fit for Rh 3B adsorbed on TiO_2.
The lifetimes, pre-exponents, and reduced chi-square are given in Table 5.1

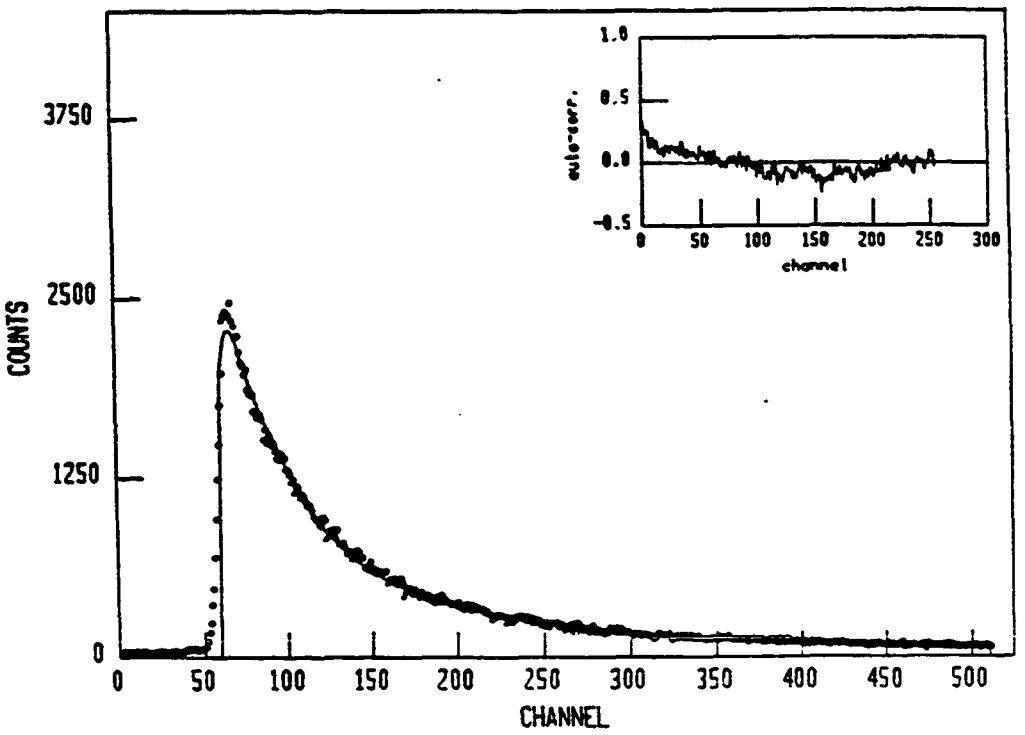

Figure 5.3. Bi-exponential fit for Rh 3B adsorbed on ZnO.
The lifetimes, pre-exponents, and reduced chi-square are given in Table 5.1

the decay profiles from the ZnO and TiO_2 samples were fit very well. Table 5.2 gives the parameters from typical fits of the data collected from samples with TiO_2 and ZnO substrates. The plots corresponding to those fits are shown in Figures 5.4 and 5.5. For both cases the reduced chi-squares are close to 1 and the autocorrelations of the residuals are nearly statistical. The fact that the tri-exponential model fits the data better than the bi-exponential mode is expected since in the tri-exponential model there are two more adjustable parameters. These additional parameters are probably the reason for the improvements in the quality of the fits.

With a tri-exponential model, it is difficult to imagine a possible mechanism that would describe the energy transfer process. In fact, as pointed out by James et al. [139,140], tri-exponential and even bi-exponential fits can mask the effects of a distribution of fluorescence lifetimes. This means that one possibility is the dye molecules are actually located at a variety of distances from the substrate which could account for the necessity of a multi-exponential model. To ascertain whether this is a plausible explanation it is necessary to examine the predictions of the CPS theory for these substrates. As pointed out previously, both the CPS theory and the Persson model predict a single exponential behavior of the fluorescence lifetime of the molecule. If because of surface roughness, oxide layers, or co-adsorbents the emitting molecules were

Table 5.2. Tri-exponential fitting parameters

Substrate	A_1	$\tau_{1,ps}$	A_2	$\tau_{2,ps}$	A_3	$\tau_{3,ps}$	χ^2
TiO_2	0.018	763	0.079	221	0.114	37	1.037
ZnO	0.005	1439	0.013	444	0.018	84	1.116

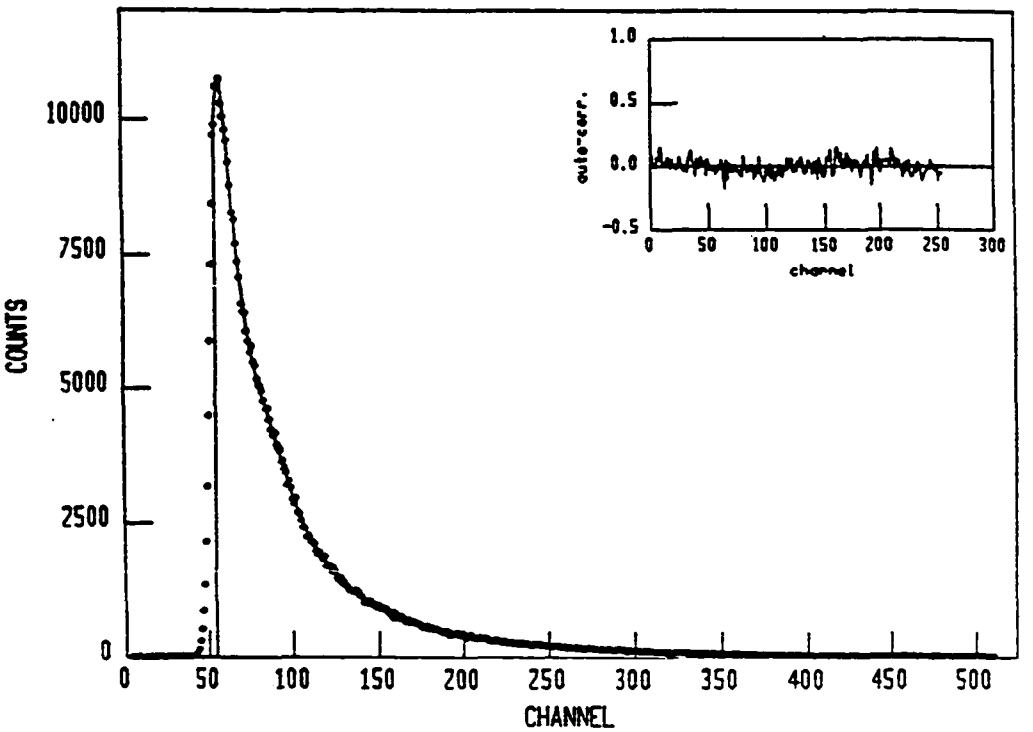

Figure 5.4. Tri-exponential fit for Rh 3B adsorbed on TiO_2. The lifetimes, pre-exponents, and reduced chi-squares are given in Table 5.2

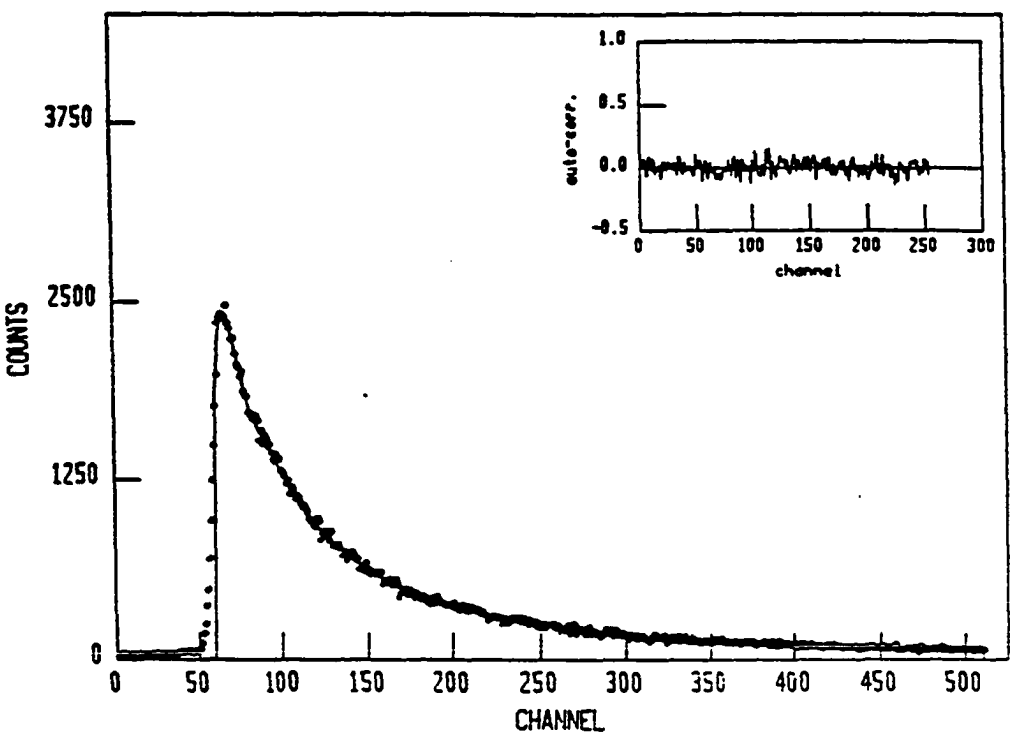

Figure 5.5. Tri-exponential fit for Rh 3B adsorbed on ZnO. The lifetimes, pre-exponents, and reduced chi-square are given in Table 5.2

located at different distances from the surface, the expected lifetimes would be different. Figure 5.6 is a plot of the calculated lifetime vs. distance curves for TiO_2. An examination of this plot indicates that to obtain the same lifetimes as those from the bi-exponential and tri-exponential fitting models a large distribution of distances is required. The longest lifetimes from the models (689 ps from the bi-exponential model and 763 ps from the tri-exponential model) imply that some molecules would be located at a distance of approximately 100 Å away from the surface. The next longest lifetime (173 ps for the bi-exponential fit and 221 ps for the tri-exponential) fit would correspond to molecules less than 25 Å from the surface. The same type of variation in distances would be necessary for the ZnO samples. Since the crystal surfaces were polished to an optical finish and care was taken to avoid collecting data from areas of the samples that appeared to have scratches, this kind of distance distribution is improbable.

Fits to Förster models

The multiexponential fits indicate that the energy transfer process for molecules directly adsorbed on a surface was not adequately described by the CPS or Persson theories. In Chapter I it was shown that many energy transfer processes can be described by Förster-type decay mechanisms. In order to determine whether this was true for Rh 3B molecules adsorbed on fused quartz, TiO_2, and ZnO it was necessary to deconvolute the fluorescence decay profiles with

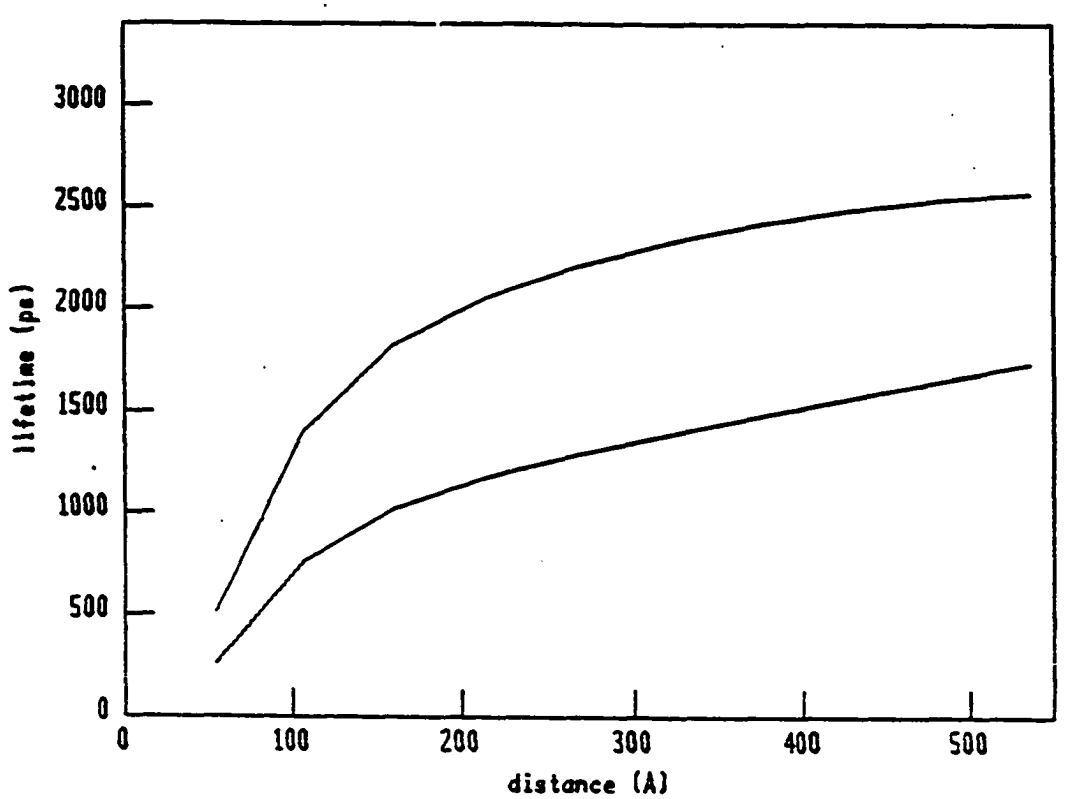

Figure 5.6. Distance vs. lifetime curves for TiO_2. The upper curve is for $\tau_{\parallel}$ and the lower curve for $\tau_{\perp}$. The optical constants used were $n_2 = 2.66$ and $\kappa_2 = 4 \times 10^{-2}$

time-dependent Förster equations. The Förster models used in this data analysis were the three-dimensional (3-D) Föster model which is given by the equation

$$N(t) = a \exp(-[t/\tau + \pi^{1/2} C_T (t/\tau)^{1/2}]),$$

and the two-dimensional (2-D) Förster model that obeys the relationship

$$N(t) = a \exp(-[t/\tau + 1.354 C_T (t/\tau)^{1/3}]).$$

Typical fitting parameters for the fluorescence decay profiles of fused quartz, TiO_2, and ZnO samples deconvoluted with the 3-D Förster equation are given in Table 5.3. The plots corresponding to these fits are shown in Figures 5.7, 5.8, and 5.9. Table 5.4 lists parameters obtained from deconvolution of the same data with the 2-D Förster model and Figures 5.10, 5.11, and 5.12 are the plots of the results from the 2-D Förster fits.

The results from these tables and figures show some interesting trends. First, both the 2-D and 3-D Förster models fit the decay profiles for the fused quartz and ZnO samples very well with reduced chi-squares near 1 and statistical autocorrelations. The fits for Rh 3B adsorbed on TiO_2 are not as good with either model although the 2-D model does appear to provide a better match than the 3-D model. A possible reason for this is, as mentioned earlier, the TiO_2 itself

Table 5.3. Fitting parameters for 3-D Förster model

Substrate	C_T	τ(ps)	χ^2
Fused Quartz	0.2872	45870	1.074
TiO_2	10.49	29270	2.926
ZnO	5.72	19360	1.314

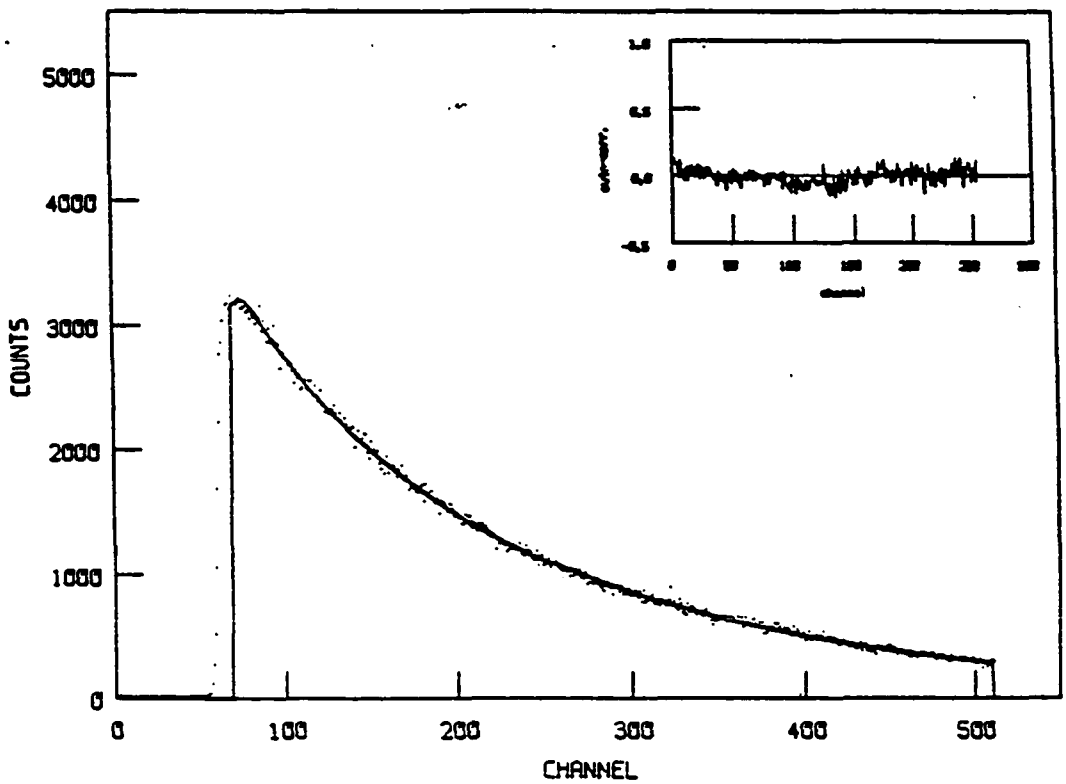

Figure 5.7. 3-Dimensional Förster fit for Rh 3B adsorbed on fused quartz. The values of C_T, τ, and reduced chi-square are given in Table 5.3

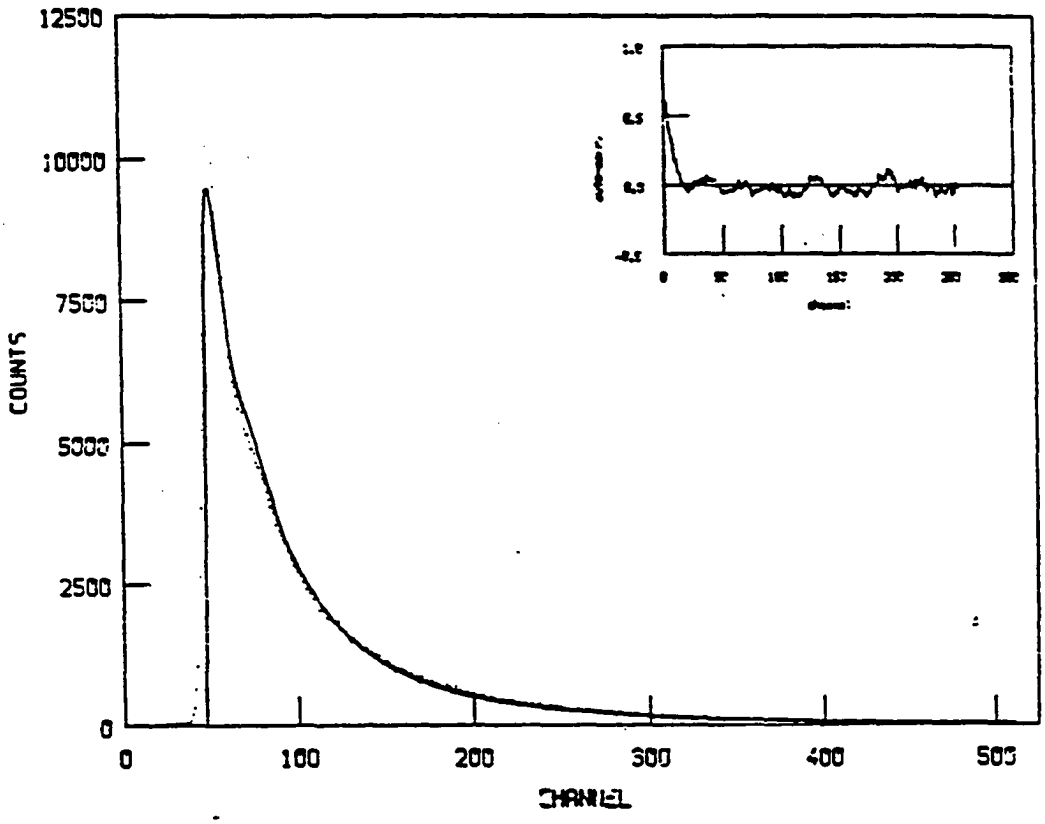

Figure 5.8. 3-Dimensional Förster fit for Rh 3B adsorbed on TiO_2. The values of C_T, τ, and reduced chi-square are given in Table 5.3

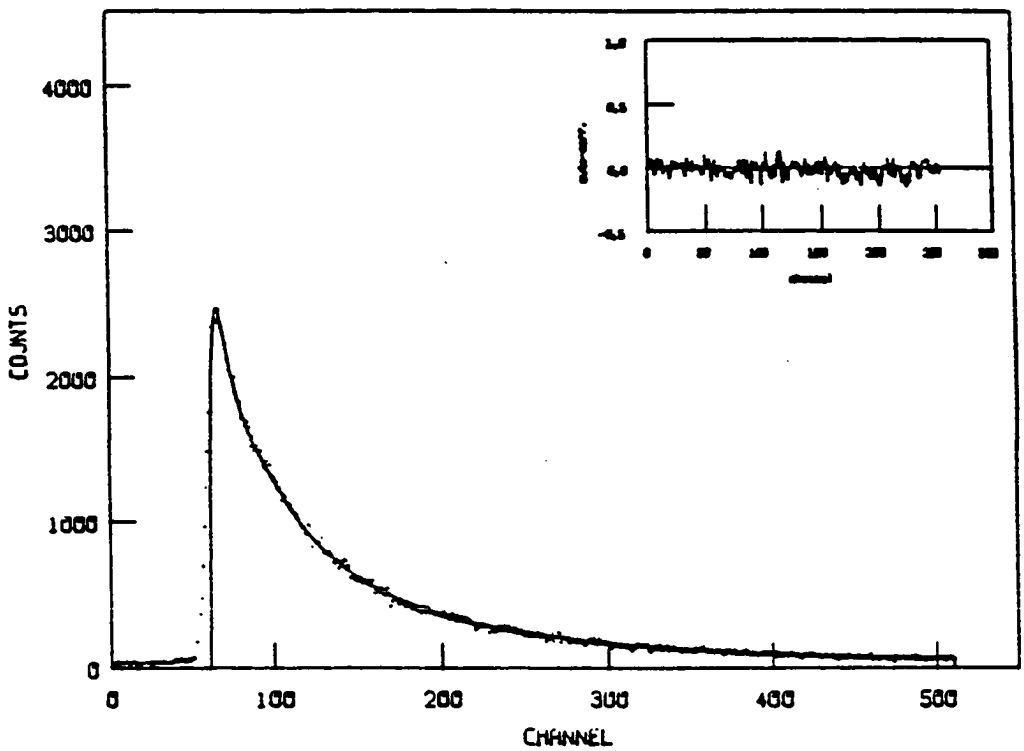

Figure 5.9. 3-Dimensional Förster fit for Rh 3B adsorbed on ZnO. The values of C_T, τ, and reduced chi-square are given in Table 5.3

Table 5.4. Fitting parameters for 2-D Förster model

Substrate	C_T	τ(ps)	χ^2
Fused Quartz	0.3807	4242	1.084
TiO_2	3.359	2171	1.181
ZnO	2.314	2529	1.118

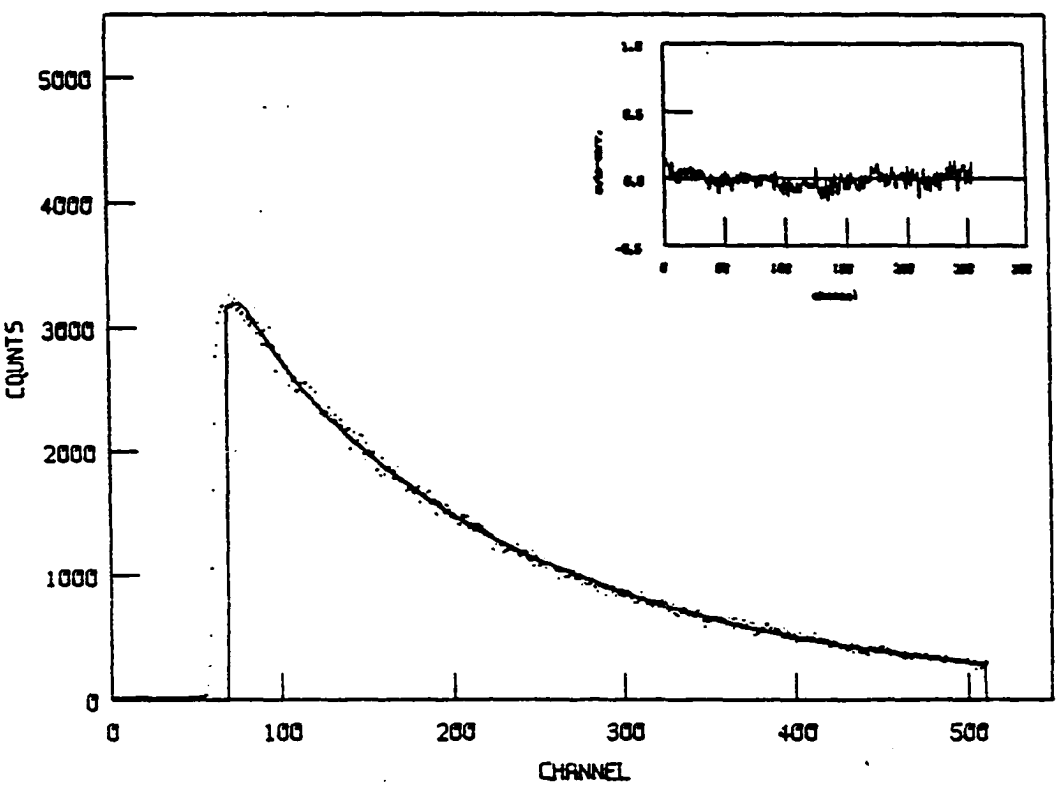

Figure 5.10. 2-Dimensional Förster fit for Rh 3B adsorbed on fused quartz. The values of C_T, τ, and reduced chi-squares are given in Table 5.4

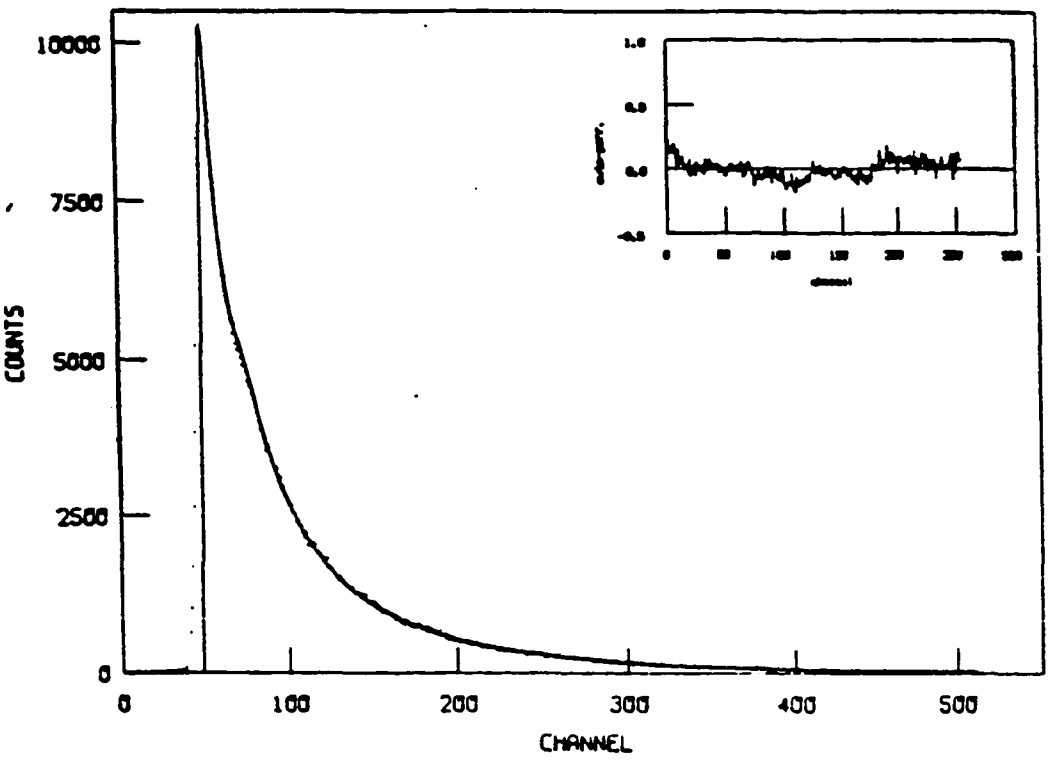

Figure 5.11. 2-Dimensional Förster fit for Rh 3B adsorbed on TiO_2. The values of C_T, τ, and reduced chi-squares are given in Table 5.4

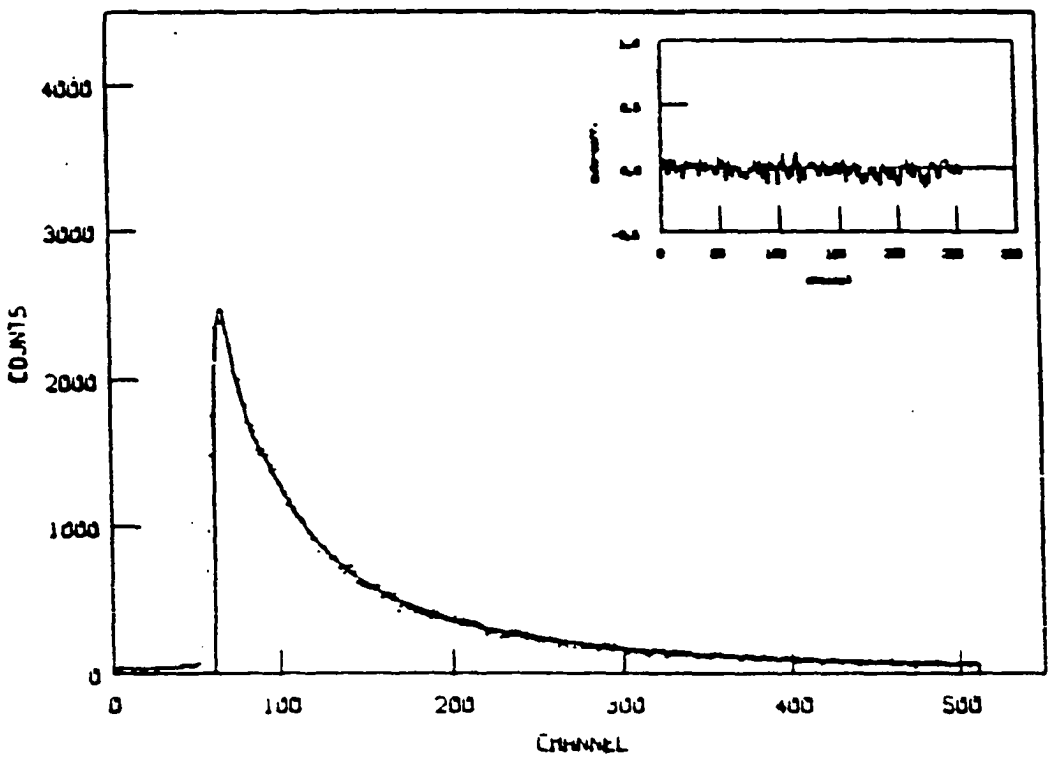

Figure 5.12 2-Dimensional Förster fit for Rh 3B adsorbed on ZnO. The values of C_T, τ, and reduced chi-squares are given in Table 5.4

Another important point is that the results show almost identical fits to the data from the fused quartz substrates with both the 2-D and 3-D Förster models. Not only are the quality of the fits very good in both cases, but in addition the calculated lifetime are within 40 ps and the C_T values are also very close. The calculated lifetimes, about 4250 ps, are close to the solution fluorescence lifetime, approximately 3500 ps [148], and to the long-component lifetime obtained from the fit to the bi-exponential model, about 3800 ps. Since the lifetime calculated from the Förster equations is supposedly the natural lifetime of the molecule it is not unexpected that it have a value slightly larger than the observed lifetime in solution. Rh 3B does have a high fluorescence quantum yield so it is expected that calculated lifetime be close to the solution lifetime, which it is. The relatively small value of C_T indicates that while there is a small amount of energy transfer to the fused quartz substrate, it is probably not enough to result in significant lifetime shortening of emitting molecules adsorbed on this substrate. This can be seen from the fact that the exponential fits give fluorescence lifetime values very close to the values obtained from solution studies.

While the 2-D and 3-D Förster models both fit the decay profiles collected from samples of Rh 3B adsorbed on ZnO very well, the numerical parameters from these fits are quite different. The 3-D Förster model predicts a natural lifetime of Rh 3B of over 19,000 ps. This lifetime is almost 5 times greater than both the

solution lifetime and the lifetime predicted for Rh 3B molecules adsorbed on quartz. While the results from the TiO_2 samples are not as well described by the 3-D Förster equation, the calculated lifetime for these samples is even longer (greater than 29,000 ps) than for the ZnO samples. These results indicate that the 3-D time-dependent Förster equation is clearly not a good description of the energy transfer to these substrates. The 2-D time-dependent Förster equation, on the other hand, gives lifetime values that although are slightly shorter than the solution lifetime are still much closer to the expected lifetime. While not as large as those calculated for the 3-D Förster model, the C_T values are still large enough so that significant lifetime shortening would result from the energy transfer process. This is again consistent with the results from the exponential fits that gave fluorescence lifetimes considerably shorter for Rh 3B molecules adsorbed on single crystal TiO_2 and ZnO semiconductors than for Rh 3B in solution.

These results indicate that energy transfer from Rh 3B molecules to ZnO and TiO_2 single crystal substrates is probably best described by a 2-D Förster type mechanism. The dimensionality of this model suggests that the acceptors in this energy transfer model are some type of surface states. The shorter-than-expected natural lifetimes that are calculated using this model could have several possible explanations. One of these possibilities is that the Rh 3B molecules might not be adsorbed flat on the crystal surface. Studies of rhodamine dyes adsorbed at submonolayer coverages on a fused silica

susbstrate [149,150] indicate that these molecules adsorb with the $S_1 \leftarrow S_0$ transition dipole moments oriented at about 50° to 55° angles from the surface. The angle between these transition dipole moments and the surface could cause a deviation from the 2-D Förster model. Another possibility is that due to surface roughness there might be some variations in the distances from the emitting molecules to the acceptors. While not enough to account for a large variation in the lifetimes of the emitting molecules, it might possibly be responsible for the differences in the calculated and expected lifetimes. The correct model to describe this type of behavior might actually be some combination of the 2-D and the 3-D time dependent Förster equations.

Conclusions

The impetus of the reseach discussed in this dissertation was to examine energy transport and trapping processes that involved organic dye molecules, and in particular the way these processes are related to the efficiency of dye-sensitized semiconductors. Three different types of experiments were performed in an attempt to acquire more insight into these processes. These experiments included: the study of energy transfer from organic dye monomers to dimers, where both species were adsorbed on the same fused silica substrate; the study of the distance dependence of the energy transfer from organic dye molecules to a wide-bandgap semi-conductor; and an examination of the energy transfer behavior for emitting molecules directly adsorbed on

the surfaces of an insulator substrate and two wide-bandgap semiconductor substrates.

The results of the first experiment show that the fluorescence emission of Cresyl Violet (CV) monomers is trapped by CV dimer molecules when the dimer concentration is much greater than the monomers. The reduced fluorescence lifetime from these monomers is best described by an equation containing both single exponential and Förster decay terms. It is unknown as to why both types of decays were required to fit the data but one possibility is that the CV monomers were transferring energy to both the CV dimers and the fused quartz substrates. Another possibility is that the instrument response functions were not as accurately determined as might have been necessary. The effect of either of these conditions could have accounted for the deviation from the expected two-dimensional Förster type behavior.

In the next set of experiments an attempt was made to examine the nonradiative energy transfer from CV monomers to a TiO_2 substrate as a function of the dye-surface separation distance. Since the lifetime behavior of emitting molecules spaced at various distances from metal surfaces was already known, the data analysis for this experiment centered on determining if analogous behavior for energy transfer to a wide-band gap semiconductor would be found. To this end, lifetime vs. separation distance curves were generated for TiO_2 based upon its optical constants. While it is difficult to reach a definitive conclusion based upon the results, there is general agreement between

the observed lifetimes and those calculated for dipoles oriented perpendicular to the TiO_2 surface, according to the CPS theory.

In the final set of experiments that were discussed it was found that the energy transfer from Rh 3B molecules to three different substrates (fused quartz, TiO_2, and ZnO) most likely occurs via a 2-D Förster-type mechanism, at least for molecules that are directly adsorbed on the substrate. This model indicates that acceptors are surface states of some type, but their exact nature is not known. While other research groups in similar types of experiments [19,29,31] found it necessary to include an exponential term in this model or multi-exponential models to fit the data, they were coating their samples with dye solutions that had higher concentrations. Therefore, it is possible that with their samples there was energy transfer between the organic dye molecules themselves as well as to the substrate. The closeness of the calculated lifetimes and C_T value for Rh 3B adsorbed on fused quartz could be due to the fact that there is little energy transfer to the fused quartz which would make it difficult to distinguish between the two models. For the wide-band gap semiconductors there is a much greater reduction in the fluorescence lifetime which implies a greater extent of nonradiative energy transfer. This results in the vastly different lifetimes predicted by the 3-D and 2-D models enabling a choice to be made as to which one appears to be the appropriate model.

CHAPTER VI. CONCLUSIONS

These experiments have increased the understanding of the processes involved in the energy transfer processes from dye molecules to substrates, in particular wide-band gap semiconductors. However, there are still many areas that need to be explored in other experiments. In terms of the energy transfer between dye molecules adsorbed on fused quartz surfaces, other members of this research group have already investigated these processes more thoroughly [148] and plan further work in this and related areas.

One set of experiments that could be performed is to repeat some of these measurements under the conditions of high vacuum and reduced temperatures. These experiments could provide several types of information. First, by performing the experiments under vacuum the emitting molecules could be adsorbed on the surfaces in a controlled and measureable fashion. This would require choosing an emitting molecule that could be readily sublimed which is not true for most laser dyes. Also a vacuum would minimize the possibility of co-adsorbents or formation of oxide layers which might have been present in these experiments and could have accounted for the deviation from strictly two-dimensional Förster-type energy transfer observed in the last set of experiments.

Using reduced temperatures would also have several benefits. The absorption bands of the ZnO and TiO_2 substrates would be narrowed at lower temperatures, e.g., liquid He temperature. This could result in

the elimination of the observed TiO_2 and ZnO fluorescence, thereby allowing a more definite conclusion to be reached regarding the applicability of the 2-D Förster model. Another benefit could be increased knowledge about the energy-accepting states in the substrates. If these states disperse the energy via bulk or surface phonons then reducing the temperature should restrict the amount of energy that could be accepted. This means that the lifetime shortening observed at the lower temperatures would be less than that at room temperature where these experiments were carried out.

Before attempting to make generalizations from these results to the entire field of dye-sensitized semiconductors, it would be necessary to examine a wider variety of systems. In the experiments reported here, the emitting molecules were from the oxazine and xanthene families of laser dyes, while the wide-bandgap semiconductors were undoped and single-crystalline. Since some of the dye sensitization experiments in solar photochemistry have involved the use of amorphous semiconductors, micellar semiconductors, and doped semiconductors, these types of substrates should definitely be considered for use in energy transfer experiments. Also, by increasing the different types of emitting molecules used in the investigations, it may be possible to find the correct molecule-substrate combination(s) that would increase the dye-sensitized semiconductor efficiencies to the point where the technology could be a significant contribution to the solar energy field.

REFERENCES

1. Gilman, P. B., Jr. Photochemistry and Photobiology 1972, 16, 211.

2. Meier, H. Photochemistry and Photobiology 1972, 16, 219.

3. "Dye Sensitization", Berg, W. F., Mazzucato, U.; Meier, H.; Semerano, G., eds.; Focal Press: London and New York, 1970.

4. Muenter, A. A.; J. Phys. Chem. 1976, 80, 2178.

5. Tanaka, M.; Nakazawa, N.; Tanaka, I.; Yamashita, H. Chem. Phys. 1985, 97, 457.

6. Nozik, A. J. Ann. Rev. Phys. Chem. 1978, 29, 189.

7. Gerischer, H. In "Advances in Electrochemistry and Electrochemical Engineering" Delahay, P., eds; Interscience: New York, 1961; Vol. 1, pp. 139-232.

8. Gerishcer, H.; Willig, F. Topics in Current Chemistry 1976, 61, 31.

9. Spitler, M.; Lübke, M.; Gerishcer, H. Chem. Phys. Lett. 1978, 56, 577.

10. Spitler, M.; Calvin, M. J. Chem. Phys. 1977, 66, 4294.

11. Spitler, M.; Calvin, M. J. Chem. Phys. 1977, 67, 5193.

12. Fujihara, M.; Tetsuo, O.; Hursh, D.; Kuwana, T. Electroanal. Chem. 1978, 88, 285.

13. Fox, M. A. Chemical Reviews 1979, 79, 253.

14. Haller, I. J. Am. Chem. Soc. 1978 100, 8050.

15. Gerishcer, H.; Spitler, M.; Willig, F. In "Electrode Processes 1979"; Bruckenstein, S., ed.; Electrochemical Society: Princeton, New Jersey, 1980; p. 115.

16. Arden, W.; Fromherz, P. Ber. Busenges. Phys. Chem. 1978, 82, 868.

17. Arden, W.; Fromherz, P. J. Electrochem. Soc.: Solid-State Science and Technology 1980, 127, 370.

18. Matsumura, M.; Yoichi, N.; Tsubomura, H. Bull. Chem. Soc. Japan 1977, 50, 2533.

19. Nakao, M.; Itoh, K.; Honda, K. J. Phys. Chem. 1984, 88, 4906.

20. Frippiat, A.; Kirsch-DeMesmaeker, A.; J. Phys. Chem. 1985, 89, 1285.

21. Matsumura, M.; Mitsuda, K.; Tsubomura, H. J. Phys. Chem. 1983, 87, 5248.

22. Terenin, A.; Akimov, I. J. Phys. Chem. 1965, 69, 730.

23. Yamase, T.; Gerishcher, H.; Lübke, M.; Pettinger, B. Ber. Bunsenges. Phys. Chem. 1979, 83, 658.

24. Spitler, M. In "Photoelectrochemistry: Fundamental Processes and Measurement Techniques"; Wallace, W., Nozik, A.; Deb, S.; eds; Electrochemical Society: Princeton, New Jersey, 1982; p. 282.

25. Kavassalis, C.; Spitler, M. T. J. Phys. Chem. 1983, 87, 3166.

26. Natoli, L. M.; Ryan, M. A.; Spitler, M. T. J. Phys. Chem. 1985, 89, 1448.

27. Sonntag, L. P.; Spitler, M. T. J. Phys. Chem. 1985, 89, 1453.

28. Spitler, M. T. J. Phys. Chem. 1986, 90, 2156.

29. Itoh, K.; Chiyokawa, Y.; Nakao, M.; Honda, K. J. Am. Chem. Soc. 1984, 106, 1620.

30. Nakashima, N.; Yoshihara, K.; Willig, F. J. Chem. Phys. 1980, 73, 3553.

31. Kenmitz, K.; Murao, T.; Yamazaki, I.; Nakashima, N.; Yoshihara, K. Chem. Phys. Lett. 1983, 101, 337.

32. Liang, Y.; Ponte Goncalves, A. M.; Negus, D. K. J. Phys. Chem. 1983, 87, 1.

33. Liang, Y.; May, P. F.; Poole, J. A.; Ponte Goncalves, A. M. J. Phys. Chem. 1984, 88, 2451.

34. Liang, Y.; Ponte Goncalves, A. M. J. Phys. Chem. 1985, 89, 3290.

35. Drexhage, K. H. In "Topics in Applied Physics"; Schäefer, F. P., ed; Springer-Verlag: West Berlin, 1973; p. 144.

36. Förster, Th. Annalen der Physik **1948**, 2, 55.

37. Förster, Th. Z. Naturforsch. **1949**, 4a, 321.

38. Förster, Th.; König, E. Z. Elektrochemie **1957**, 61, 344.

39. Förster, Th. Disc. Faraday Society **1959**, 27, 7.

40. Förster, Th. In "Comparative Effects of Radiation"; Burton, M.; Kirby-Smith, J. J., Magee, J. L.; eds; Wiley: New York, 1960; p. 300.

41. Förster, Th. In "Modern Quantum Chemistry Part III: Action of Light and Organic Molecules" Sinanoglu, O., ed.; Academic: New York, 1965; p. 93.

42. Avouris, P.; Gelbart, M.; El-Sayed, M. A. Chem. Reviews **1977**, 77, 793.

43. Knox, R. S. In "Bioenergetics of Photosynthesis"; Govindjee, R., ed.; Academic: New York, 1975; p. 183.

44. "CRC Handbook of Chemistry and Physics", 57th edition; Weast, R. C., ed; CRC Press: Cleveland, 1976; p. A-165.

45. Dexter, D. L. J. Chem. Phys. **1953**, 21, 836.

46. Ore, A. J. Chem. Phys. **1959**, 31, 442.

47. Knox, R. S. Physica **1968**, 39, 361.

48. Craver, F. W.; Knox, R. S. Molecular Physics **1971**, 22, 385.

49. Blumen, A. J. Chem. Phys. **1981**, 74, 6926.

50. Haan, W.; Zwanzig, R. J. Chem. Phys. **1978**, 68, 1879.

51. Gochanour, C. R.; Andersen, H. C.; Fayer, M. D. J. Chem. Phys. **1979**, 70, 4254.

52. Loring, R. F.; Andersen, H. C.; Fayer, M. D. J. Chem. Phys. **1982**, 76, 2015.

53. Stehfest, H. Commun. ACM **1970**, 13, 47.

54. O'Connor, D. V.; Phillips, D. "Time-Correlated Single Photon Counting"; Academic Press: London, 1984.

55. Robbins, R. J. Ph.D. Dissertation, University of Melbourne, Melbourne, Australia, 1980.

56. Bevington, P. R. In "Data Reduction and Error Analysis for the Physical Sciences"; McGraw-Hill: New York, 1969.

57. Grinvald, A.; Steinberg, I. Z. Analytical Biochemistry 1974, 59, 583.

58. Fox, M. A.; Nobs, F. J.; Voynick, T. J. Am. Chem. Soc. 1980, 102, 4029.

59. Hohman, J. R.; Fox, M. A. J. Am. Chem. Soc. 1982, 104, 401.

60. Loring, R. F.; Fayer, M. D. Chem. Phys. 1982, 70, 139.

61. Huber, D. L. Phys. Rev. B 1979, 20, 2307, 5333.

62. Ediger, M. D.; Fayer, M. D. J. Chem. Phys. 1983, 78, 2518.

63. Mulder, B. J. Philips Res. Rep. 1967, 22, 553.

64. Garoff, S.; Stevens, R. B.; Hanson, C. D.; Sorenson, G. K. J. Lumin. 1981, 24, 773.

65. Wokaun, A.; Lutz, H. P.; King, A. P.; Wild, U. P.; Ernst, R. R. J. Chem. Phys. 1983, 79, 509.

66. Miller, R. J. D.; Pierre, M.; Fayer, M. D. J. Chem. Phys. 1983, 78, 5138.

67. Fayer, M. D., private communication, Stanford University, Department of Chemistry, Stanford, California.

68. Ippen, E. P.; Shank, C. V. Appl. Phys. Lett. 1975, 27, 488.

69. Beddard, G. S.; Fleming, G. R.; Porter, G.; Searle, G. F. W.; Synowiec, J. A. Biochim. Biophys. Acta 1979, 545, 165.

70. Marquardt, D. W. J. Soc. Ind. Appl. Math. 1963, 11, 431.

71. Chambers, R. W.; Kajiwara, T.; Kearns, D. R. J. Phys. Chem. 1974, 78, 380.

72. Selwyn, J. E.; Steinfeld, J. I. J. Phys. Chem. 1972, 76, 762.

73. Rohatgi, K. K.; Mukhopadhyay, A. K. Photochem. Photobiol. 1971, 14, 551.

74. McRae, E. G.; Kasha, M. J. Chem. Phys. 1958, 28, 721.

75. McRae, E. G.; Kasha, M. "Physical Processes in Radiation Biology"; Academic Press: New York, 1964.

76. Kasha, M.; Rawls, H. R.; Ashraf-Bayoumi, M. Pure Appl. Chem. 1965, 11, 371.

77. Lopez-Arbeloa, I.; Ruiz Ojeda, P. Chem. Phys. Lett. 1982, 87, 5560.

78. Faraggi, M.; Peretz, P.; Rosenthal, I.; Weinraub, D. Chem. Phys. Lett. 1984, 103, 310.

79. Sadkawski, P. J.; Fleming, G. R. Chem. Phys. Lett. 1978, 57, 526.

80. Beddard, G. S.; Doust, T.; Meech, S. R.; Phillips, D. J. Photochem. 1981, 17, 427.

81. Tao, T. Biopolymers 1969, 8, 609.

82. Chuang, T. J.; Eisenthal, K. B. J. Chem. Phys. 1972, 57, 5094.

83. Loring, R. F.; Andersen, H. C.; Fayer, M. D. Chem. Phys. 1984, 85, 149.

84. Drexhage, K. H.; Flek, M.; Kuhn, H.; Schäefer, F. P.; Sperling W. Ber. Bunsenges. Phys. Chem. 1966, 70, 1179.

85. Drexhage, K. H.; Kuhn, H.; Schäefer, F. P. Ber. Bunsenges. Phys. Chem. 1968, 72, 329.

86. Drexhage, K. H. J. Luminescence 1970, 1,2, 693.

87. Drexhage, K. H. In "Progress in Optics", Wolf, E., ed.; North-Holland: Amsterdam, 1974; Vol. 12.

88. Kuhn, H. J. Chem. Phys. 1970, 53 101.

89. Philpott, M. R. Chem. Phys. Lett. 1973, 19, 435.

90. Morawitz, H. Phys. Rev. 1969, 187, 1792.

91. Chance, R. R.; Prock, A.; Silbey, R.; J. Chem. Phys. 1974, 60, 2744.

92. Chance, R. R.; Prock, A.; Silbey, R.; J. Chem. Phys. 1975, 62, 2245.

93. Chance, R. R.; Miller, A. H.; Prock, A.; Silbey, R.; Chem. Phys. Lett. 1975, 33, 590.

94. Chance, R. R.; Miller, A. H.; Prock, A.; Silbey, R. J. Chem. Phys. 1975, 63, 1589.

95. Chance, R. R.; Prock, A.; Silbey, R. Phys. Rev. A. 1975, 12, 1448.

96. Chance, R. R.; Prock, A.; Silbey, R. J. Chem. Phys. 1976, 65, 2527.

97. Chance, R. R.; Prock, A.; Silbey, R. Adv. Chem. Phys. 1978, 37, 1.

98. Sommerfeld, A. "Partial Differential Equations of Physics"; Academic Press: New York, 1949.

99. Waldeck, D. H.; Alivisatos, A. P. Harris, C. B. Surface Science 1985, 158, 103.

100. Morawitz, H. IBM J. Res. Develop. 1979, 23, 517.

101. Philpott, M. R. J. Chem. Phys. 1975, 62, 1812.

102. Morawitz, H.; Philpott, M. R. Phys. Rev. B 1974, 10, 4863.

103. Babiker, M. J. Phys. C. 1979, 12, 4985.

104. Pockrand, I.; Brillante, A.; Möbius, D. Il Nuovo Cimento 1981, 63B, 350.

105. Burstein, E.; Chen, W. P.; Chen, Y. J., Hartstein, A. J. Vac. Sci. Technol. 1973, 11, 1004.

106. Ritchie, R. H. Surf. Sci. 1973, 34, 1.

107. Weber, W. H.; Eagen, C. F. Opt. Letters 1979, 4, 236.

108. Alivisatos, A. P.; Waldeck, D. H.; Harris, C. B. J. Chem. Phys. 1985, 82, 541.

109. Campion, A.; Gallo, A. R.; Harris, C. B.; Robota, H. J.; Whitmore, P. M. Chem. Phys. Lett. 1980, 73 447.

110. Whitmore, P. M.; Robota, H. J.; Harris, C. B. J. Chem. Phys. 1982, 77, 1560.

111. Ford, G. W.; Weber, W. H. Surf. Sci. 1981, 109, 451.

112. Arias, J.; Avarind, P. K.; Metiu, H. Chem. Phys. Lett. 1982, 85, 404.

113. Persson, B. N. J. J. Phys. C. 1978, 11, 4251.

114. Persson, B. N. J. Persson, M. Solid State Communications 1980, 36 175.

115. Persson, B. N. J.; Lang, N. D. Phys. Rev. B 1982, 26, 5409.

116. Persson, B. N. J.; Avouris, Ph. J. Chem. Phys. 1983, 79, 5156.

117. Avouris, Ph.; Persson, B. N. J. J. Phys. Chem. 1984, 88, 837.

118. Persson, B. N. J.; Andersson, S. Phys. Rev. B 1984, 29, 4382.

119. Eagen, C. F.; Weber, W. H.; McCarthy, S. L.; Terhune, R. W. Chem. Phys. Lett. 1980, 75, 274.

120. Wähling, G.; Möbius, D.; Raether, H. Z. Naturforsch. 1978, 33a, 907.

121. Pockrand, I.; Brillante, A.; Möbius, D. Chem. Phys. Lett. 1980, 69, 499.

122. Pockrand, I.; Swalen, J. D.; Santo, R.; Brillante, A.; Philpott, M. R. J. Chem. Phys. 1978, 69, 4001.

123. Knoll, W.; Philpott, M. R.; Swalen, J. D.; Girlando, A. J. Chem. Phys. 1981, 75, 4795.

124. Lukosz, W.; Meier, M. Optics Letters 1981, 6, 251.

125. Brenner, R. E.; Dornhaus, R.; Chang, R. K. Optics Communications 1979, 30, 145.

126. Kurczewska, H.; Bässler, H. J. Lumin. 1977, 15, 261.

127. Rossetti, R.; Brus, L. E. J. Chem. Phys. 1980, 73, 572.

128. Rossetti, R.; Brus, L. E. J. Chem. Phys. 1982, 76, 1146.

129. Inacker, O.; Kuhn, H. Chem. Phys. Lett. 1974, 27, 317.

130. Killesreiter, H. J. Lumin. 1976, 12-13, 857.

131. Dexter, D. L. J. Lumin. 1979, 18-19, 779.

132. Hayashi, T.; Castner, T. G.; Boyd, R. W. Chem. Phys. Lett. 1983, 94, 461.

133. Whitmore, P. M.; Alivisatos, A. P.; Harris, C. B. Phys. Rev. Lett. 1983, 50, 1092.

134. Avouris, Ph.; Demuth, J. E. J. Chem. Phys. 1981, 75, 4783.

135. Avouris, Ph.; Schmeisser, D.; Demuth, J. E. J. Chem. Phys. 1983, 79, 488.

136. Bücher, H.; Drexhage, K. H.; Fleck, M.; Kuhn, H.; Möbius, D.; Schäfer, F. P.; Sondermann, J.; Sperling, W.; Tillmann, P.; Wiegand, J. Molecular Crystals 1967, 2, 199.

137. Kuhn, H.; Möbius, D.; Bücher, H. in "Physical Methods of Chemistry Part IIIB Optical, Spectroscopic and Radioactivity Methods" Weissberger, A.; Rossiter, B. W., eds; Wiley-Interscience: New York, 1972; p. 577.

138. Blodgett, K. B.; Langmuir, I. Phys. Rev. 1937, 51, 964.

139. James, D. R.; Ware, W. R. Chem. Phys. Lett. 1985, 120, 455.

140. James, D. R.; Liu, Y. S.; DeMayo, R.; Ware, W. R. Chem. Phys. Lett. 1985, 120, 460.

141. Spitler, M. T. Proceedings of the Eighth Department of Energy Solar Photochemistry Research Conference, Lake Geneva, Wisconsin (June 11-14, 1984).

142. Drexhage, K. H.; Fleck, M.; Schäefer, F. P.; Sperling W. Ber. Bunsenges. Phys. Chem. 1966, 20, 1179.

143. Drexhage, K. H.; Kuhn, H.; Schäfer, F. P. Ber. Bunsenges. Phys. Chem. 1968, 72, 329.

144. Anfinrud, P.; Crackel, R. L.; Struve, W. S. J. Phys. Chem. 1984, 88, 5873.

145. Cardona, M.; Harbeke, G. Phys. Rev. 1965, 137, A1467.

146. Brus, L. E. J. Chem. Phys. 1981, 74, 737.

147. Yasa, Z. A.; Amer, N. M. Opt. Commun. 1981, 36, 406.

148. Anfinrud, P. A.; Hart, D. E.; Hedstrom, J. F.; Struve, W. S. J. Phys. Chem. 1986, 90, 3116.

149. Heinz, T. F.; Chen, C. K.; Ricard, D.; Shen, Y. R. Phys. Rev. Lett. 1982, 48, 478.

150. DiLazzaro, P.; Mataloni, P.; DeMartin, F. Chem. Phys. Lett. 1985, 114, 103.

ACKNOWLEDGEMENTS

None of this reseach would have been possible without the excellent advice, supervision, and support of Dr. Walter S. Struve during my years as a graduate student. Deserving of special recognition is Philip Anfinrud with whom a large portion of this research was done and who was always willing to assist in overcoming problems that arose in these studies. Other members of the research group who were particularly helpful with their expertise, suggestions, and friendship include: Tim Causgrove, Dave Hart, and Jack Hedstrom. Finally, I want to thank the members of the "Hazardous Chemical Waste" (a.k.a. "The Cheap Sunglasses") for helping to make my springs and summers more enjoyable and to wish them the best of luck in the quest for those ever-elusive intramural T-shirts.

```
**********SIMPS**********

PROGRAM FOR CALCULATING THE NORMALIZED DECAY RATE CONSTANTS
VERSUS NORMALIZED DISTANCE FOR PARALLEL AND PERPENDICULAR
DIPOLES SPACED AT VARIOUS DISTANCES FROM A SURFACE OF KNOWN
COMPLEX REFRACTIVE INDEX USING SIMPSON'S RULE FOR NUMERICAL
INTEGRATION.

DIMENSION RESULD(200),RESR(200),RESNR(200),RES(200),RINV(200)
DIMENSION DHAT(200),RESULT(200),QA(200),BINV(200),RESULU(200)
BYTE OUTFIL(16)
DOUBLE PRECISION PI,D,Y,E1,B,A,H,XMIN,XMAX,HDOWN
DOUBLE PRECISION BRADL,BRADG,U,TU,BUPA1
DOUBLE PRECISION SUMEVB,SUMODB,RABS1,RABS2
DOUBLE PRECISION BNRADL,BNRADG,UDOWN,TD1
DOUBLE PRECISION SUM4B,SUM2B,Q,THETA,BET
COMPLEX*8 E2,E,TU1,TU2,TD2,RPERU,RPARU,RPERD,RPARD,BD2
COMPLEX*8 G,SUMEVA,SUMODA,BRAD,BRADI,BRADF,BUP1,BUP2,BDOW1
COMPLEX*8 SUM4A,SUM2A,BDOWN2,BR,BNR,BNRAD,BNRADI,BNRADF
COMPLEX*8 TA,TB,TE,TF,RC,TF1,AZQ,AZW,AZX,ASD,AZE,TAY
COMPLEX*8 BDI,BDF,SUM4,SUM2,SUMEV,SUMOD,SUMDE,SUMDO,BUP
COMPLEX*8 BUPI,BUPF,BD2A,BDOWN1,BDOWNI,BDOWNF,RESULE
COMPLEX*8 RESULV,RESP,RESNP

----------initialize values----------

PI=3.14159
G=(0.0,-1.0)
Q=1.0
THETA=1.0

---------- input data ----------

TYPE 10
FORMAT ('$NUMBER OF INTERVALS:')
ACCEPT *,N
TYPE 20
FORMAT ('$VALUE OF D FOR ONE FATTY ACID LAYER IN ANGSTROMS:')
ACCEPT *,D
TYPE 30
FORMAT ('$EMISSION WAVELENGTH IN ANGSTROMS:')
ACCEPT *,Y
TYPE 40
FORMAT ('$VALUE OF N1:')
```

```
ACCEPT *,E1
TYPE 50
FORMAT ('$VALUE OF N2+iK2(N2,K2):')
ACCEPT 630,E2
TYPE 60
FORMAT ('$NUMBER OF FATTY ACID LAYERS:')
ACCEPT *,L
TYPE 61
FORMAT ('$OUTPUT FILENAME:')
ACCEPT 450,OUTFIL

------------calculation of bup------------------------------

OPEN (UNIT=1,NAME=OUTFIL,TYPE='NEW',ERR=210)
WRITE (1,610)N,D,Y
WRITE (1,620)E1,E2,L
M=N
ND=10*N
MD=ND
B=0.99
A=0.0
H=(B-A)/FLOAT(N)
XMIN=1.01
XMAX=40.0
HDOWN=(XMAX-XMIN)/FLOAT(ND)
E2=E2**2
E1=E1**2
E=(E2/E1)
DO 200 I=1,L
DHAT(I)=(FLOAT(I)*2.0*PI*D*SQRT(E1))/Y
BET=((Q*THETA)/(4.*DHAT(I)**3))*AIMAG((E2-E1)/(E2+E1))
SUMEV=(0.0,0.0)
SUMOD=(0.0,0.0)
SUMDE=(0.0,0.0)
SUMDO=(0.0,0.0)
BUPI=(0.0,0.0)
BUPF=(0.0,0.0)
SUMEVA=(0.0,0.0)
SUMODA=(0.0,0.0)
BRADI=(0.0,0.0)
BRADF=(0.0,0.0)
BRADL=0.0
BRADG=0.0
BDOW1=(0.0,0.0)
BDOWN1=(0.0,0.0)
```

```
BDOWNI=(0.0,0.0)
BDOWNF=(0.0,0.0)
 DO 100 J=1,M
 K=0
 KK=0
 U=0.0
 TU1=(0.0,0.0)
 TU2=(0.0,0.0)
 U=A+FLOAT(J)*H
 TU=SQRT(1.-U**2)
 TU1=-CMPLX(0.0,TU)
 TU2=G*CSQRT(E-U**2)
 RPARU=(0.0,0.0)
 RPERU=(0.0,0.0)
 RPARU=((E1*TU2)-(E2*TU1))/((E1*TU2)+(E2*TU1))
 RPERU=(TU1-TU2)/(TU1+TU2)
 RABS1=CABS(RPERU)
 RABS2=CABS(RPARU)
 BUP1=(U/TU1)*((1.-(CABS(RPERU)**2))
     +(1.-U**2)*(1.-CABS(RPARU)**2))
 AZW=(-2.*TU1*DHAT(I))
 AZQ=CEXP(AZW)
 ASD=(U/TU1)*((RPERU)+(1.-U**2)*RPARU)
 BUP2=(U/TU1)*AZQ*((RPERU)
      +(1.-U**2)*RPARU)
 BUP=-BUP2
 BDOW1=(U/TU1)*((1.-CABS(RPERU)**2)
      +(1.-U**2)*(1.-CABS(RPARU)**2))
 BDOWN1=(3./8.)*Q*(BDOW1)
 BR=RPARU*CEXP(-2.*TU1*DHAT(I))*(U**3)/TU1
 BRAD=BR
 K=J/2
 KK=J-2*K
 IF (J.NE.1) GO TO 65
 BUPI=BUP
 BDOWNI=BDOWN1
 BRADI=BRAD
 GO TO 100
 IF (J.NE.M) GO TO 70
 BUPF=BUP
 BDOWNF=BDOWN1
 BRADF=BRAD
 GO TO 100
 IF (KK.NE.0) GO TO 80
 SUMEV=SUMEV+BUP
 SUMDE=SUMDE+BDOWN1
 SUMEVA=SUMEVA+BRAD
```

```
 GO TO 100
 SUMOD=SUMOD+BUP
 SUMODA=SUMODA+BRAD
 SUMDO=SUMDO+BDOWN1
 CONTINUE
RESULV=(H/3.)*(BUPI+4.*SUMEV+2.*SUMOD+BUPF)
RESULU(I)=Q-(3./4.)*Q*AIMAG(RESULV)
RESP=(H/3.)*(BRADI+4.*SUMEVA+2.*SUMODA+BRADF)
RESR(I)=Q-(3./2.)*Q*AIMAG(RESP)

--------------- calculation of bdown ------------------------

BDI=(0.0,0.0)
BDF=(0.0,0.0)
SUM4=(0.0,0.0)
SUM2=(0.0,0.0)
SUM4A=(0.0,0.0)
SUM2A=(0.0,0.0)
BNRADI=(0.0,0.0)
BNRADF=(0.0,0.0)
BNRADL=0.0
BNRADG=0.0
 DO 150 J=1,MD
 K=J/2
 KK=J-2*K
 UDOWN=0.0
 UDOWN=XMIN+FLOAT(J)*HDOWN
 TD1=(0.0)
 TD2=(0.0,0.0)
 TD1=SQRT(UDOWN**2-1.)
 TD2=G*CSQRT(E-UDOWN**2)
 RPERD=(0.0,0.0)
 RPARD=(0.0,0.0)
 RPARD=((E1*TD2)-(E2*TD1))/((E1*TD2)+(E2*TD1))
 RPERD=(TD1-TD2)/(TD1+TD2)
 W=EXP(-2.*TD1*DHAT(I))
 BD2=(UDOWN/TD1)*(RPERD+(1.-UDOWN**2)*RPARD)
    *EXP(-2.*TD1*DHAT(I))
 BD2A=(3./4.)*Q*(BD2)
 BNR=RPARD*EXP(-2.*TD1*DHAT(I))*UDOWN**3/TD1
 BNRAD=BNR
 IF (J.NE.1) GO TO 110
 BDI=BD2A
 BNRADI=BNRAD
 GO TO 150
 IF (J.NE.MD) GO TO 120
 BDF=BD2A
```

```
 BNRADF=BNRAD
 GO TO 150
 IF (KK.NE.0) GO TO 130
 ----------------------summation of intervals----------
 SUM4=SUM4+BD2A
 SUM4A=SUM4A+BNRAD
 GO TO 150
 SUM2=SUM2+BD2A
 SUM2A=SUM2A+BNRAD
 CONTINUE
SUM4=SUM4
SUM2=SUM2
BDI=BDI
BDF=BDF
RESULE=(HDOWN/3.)*(BDI+4.*SUM4+2.*SUM2+BDF)
RESULD(I)=AIMAG(RESULE)
RESNP=(HDOWN/3.)*(BNRADI+4.*SUM4A+2.*SUM2A+BNRADF)
RESNR(I)=(1.-Q)-(3./2.)*Q*AIMAG(RESNP)
RES(I)=RESR(I)+RESNR(I)
RINV(I)=1./RES(I)
RESULT(I)=RESULU(I)+RESULD(I)
QA(I)=RESULU(I)/RESULT(I)
BINV(I)=1./RESULT(I)
TYPE 595,I,DHAT(I),BINV(I),RINV(I)
WRITE(1,600)I,DHAT(I),BINV(I),RINV(I)
CONTINUE
CLOSE(UNIT=1,DISPOSE='SAVE')
STOP
FORMAT(16A1)
FORMAT( 3X'I='I4,3X'DHAT='F8.5,3X'1/B='F8.5,3X'RINV='F8.5)
FORMAT( 3XI4,3XF8.5,3XF8.5,3XF8.5)
FORMAT( 3X'N='I6,3X'D='F10.6,3X'Y='F10.3)
FORMAT( 3X'N1='F9.6,3X'N2+iN2='2F9.6,3X'L='I5)
FORMAT( 2F9.6)
FORMAT( 10X'J='I5)
END
```

```
----------------PLOTIT-------------------------
PROGRAM TO PLOT CURVES CALCULATED USING SIMPSONS RULE

BYTE OUTFIL(16),NAME(6)
DIMENSION N(6),X(200),Y1(200),Y2(200)
COMMON X,Y1,Y2,XMIN,XMAX,XTIC,YMIN,YMAX,YTIC,N,NCHNLS,CMIN,CNEW

-------------INITIALIZING PLOTTER---------------------

CALL INIPLT(9,10.25,7.25)
CALL WINDOW(1.,9.75,.5,6.75)
CALL VUPORT(0.,10.,0.,10.)
CALL MOVETO(2.,2.,0)
CALL MOVETO(0.,0.,0)
CALL ENDPLT

-------------INPUTTING PARAMETERS---------------------

TYPE 10
FORMAT(/'$ENTER MINIMUM,MAXIMUM,AND INCREMENT VALUES FOR X:')
ACCEPT *,XMIN,XMAX,XTIC
TYPE 20
FORMAT(/'$ENTER MINIMUN,MAXIMUM,AND INCREMENT VALUES FOR Y:')
ACCEPT *,YMIN,YMAX,YTIC
XDIF=XMAX-XMIN
YDIF=YMAX-YMIN
TYPE 30
FORMAT(/'$ENTER NUMBER OF DATA POINTS:')
ACCEPT *,NCHNLS
TYPE 35
FORMAT(/'$ENTER VALUE OF TAU:')
ACCEPT *,TAU
TYPE 40
FORMAT(/'$ENTER OUTPUT FILENAME:')
ACCEPT 45,OUTFIL
FORMAT (16A1)
CALL ASSIGN(1,OUTFIL,0,'OLD','CC')
DO 51 I=1,NCHNLS
READ(1,50,END=46) L,X(I),Y1(I),Y2(I)
FORMAT( 2XI4,3XF8.5,3XF8.5,3XF8.5)
X(I)=668.4508*X(I)
Y1(I)=TAU*Y1(I)
Y2(I)=TAU*Y2(I)
CONTINUE
CALL CLOSE(1)
TYPE 55
```

```
FORMAT (/'$ENTER LOGICAL UNIT NUMBER (7=SCREEN,9=PLOTTER,'
 ',nn=file FTNnn.DAT):')
ACCEPT *,LUN
IF (LUN.EQ.7) GO TO 60
XPAGE=10.25
YPAGE=7.25
GO TO 65
XPAGE=10.2
YPAGE=6.3
CALL INIPLT(LUN,XPAGE,YPAGE)
CALL WINDOW(1.4,XPAGE-.4,.9,YPAGE-.1)
CALL SCALE(XMIN,XMAX,YMIN,YMAX)
DO 100 M=1,2
GO TO (80,70)M
CALL DASHLN(X,Y2,NCHNLS,0,-1,0,0,0)
GO TO 100
CALL DASHLN(X,Y1,NCHNLS,0,-1,0,0,0)
CONTINUE
CALL AXIS(XTIC,YTIC,'distance (A)',12,2,0,'lifetime (ps)',13,2,0)
XWRLD=.183*(XMAX-XMIN)+XMIN
YWRLD=.925*(YMAX-YMIN)+YMIN
IX=ISCRX(XWRLD)
IY=ISCRY(YWRLD)
CALL ENDPLT
TYPE 130
FORMAT(/'$DO YOU WANT TO CHANGE OUTPUT DEVICE?')
ACCEPT 140,NDEV
FORMAT(A1)
IF (NDEV.EQ.'Y') GO TO 150
TYPE 160
FORMAT(/'$SY:CLEAR.DAT')
STOP
END
```